Coherent long-range transport of entangled electron spins

Baptiste Jadot

Université Grenoble Alpes

THÈSE

Pour obtenir le grade de

DOCTEUR DE L'UNIVERSITÉ GRENOBLE ALPES

Spécialité : **Physique de la Matière Condensée et du Rayonnement**

Arrêté ministériel : 25 mai 2016

Présentée par

Baptiste Jadot

Thèse dirigée par **Tristan Meunier**

préparée au sein de l'**Institut Néel - CNRS**
et de l'**École Doctorale de Physique de Grenoble**

Coherent long-range transport of entangled electron spins

Thèse soutenue publiquement le **18 février 2020**,
devant le jury composé de :

Thomas Ihn
Professeur, ETH Zurich, Rapporteur

Patrice Bertet
Directeur de recherche, CEA Saclay, Rapporteur

Jean-Michel Raimond
Professeur, Laboratoire Kastler Brossel, Examinateur

Alexia Auffèves
Directrice de recherche, Institut Néel – CNRS, Présidente

Tristan Meunier
Directeur de recherche, Institut Néel – CNRS, Directeur de thèse

Abstract

Quantum computing is a field of growing interest, especially in Grenoble with an exceptional concentration of both research and industrial groups active in this field. The global aim is to develop a new kind of nano-processor, based on quantum properties. Its building brick is a two-level quantum system, in our case the spin of an electron trapped in a quantum dot.

In this quest for a large-scale architecture, networked quantum computers offer a natural path towards scalability. Indeed, separating the computational task among quantum core units interconnected via a coherent quantum mediator would greatly simplify the addressability challenges. These quantum links should be able to coherently couple arbitrary nodes on fast timescales, in order to share entanglement across the whole quantum circuit. In semiconductor quantum circuits, nearest neighbor entanglement has already been demonstrated, and several schemes exist to realize long-range coupling. Among them, a possible implementation of this quantum mediator would be to prepare an entangled spin state and shuttle individual electron spins across the structure, provided that this transport preserves the entanglement.

In this work, we demonstrate the fast and coherent transport of electron spin qubits across a 6 µm long channel, in a GaAs/AlGaAs laterally defined nanostructure. Using the moving potential induced by a propagating surface acoustic wave, we send sequentially two electron spins initially prepared in a spin singlet state. During its displacement, each spin experiences a coherent rotation due to spin-orbit interaction, over timescales shorter than any decoherence process. By varying the electron separation time and the external magnetic field, we observe quantum interferences which prove the coherent nature of both the initial spin state and the transfer procedure. We show that this experiment is analogous to a Bell measurement, allowing us to quantify the entanglement between the two electron spins when they are separated, and proving that this fast and long-range qubit displacement is an efficient procedure to share entanglement across future large-scale structures.

Contents

Introduction

Quantum computing became in the last decade a field of exponentially growing interest for many researchers of various background. Its premise, as proposed by Feynman in 1982,[Fey82] relies on harnessing the quantum properties of matter on an atomic scale to solve complex computational problems, such as the simulation of chemical bonds inside a molecule. Since then, numerous algorithms have been developed, such as the famous Shor[Sho94] (factorization of prime numbers) or Grover[Gro96] (search in a database) algorithms, and promise an exponentially faster computation time compared to classical supercomputers.

The working principle of a quantum computer relies on two fundamentally quantum properties of matter, superposition and entanglement. Indeed a quantum bit (or *qubit*) can, contrarly to its classical counterpart, be in a an arbitrary superposition of its two basis states $|0\rangle$ and $|1\rangle$. We usually parametrized such a quantum superposition of states by two angles ϕ and θ, so that the qubit state is $|\phi\rangle = \cos\left(\frac{\theta}{2}\right)|0\rangle + \sin\left(\frac{\theta}{2}\right)e^{i\phi}|1\rangle$. This superposition principle is the origin of the computational speed-up, allowing some parallelization with the appropriate quantum algorithms. In addition to this phenomenon, quantum algorithms also exploit the entanglement shared between qubits. This quantum property, famously called *spooky action at a distance* by Einstein, characterizes systems of several qubits that share a common quantum state. Even when separated over large distances, any operation (such as a measurement) on one qubit can have an instantaneous impact on the other entangled qubits. During the last century, this phenomenon was the origin of heated debates over the nature of reality, entanglement being seemingly irreconcilable with our macroscopic understanding of the world. Since then, experimental proofs of entanglement between distant qubits have been provided,[Asp81; Hen15] ruling-out locality and establishing this long-range interaction as a true quantum phenomenon.

Harnessing these quantum properties and developing a multi-qubit architecture has been in the last decades the subject of intense and various research. In 2000, DiVincenzo proposed five criteria for a successful implementation of a quantum computer: [DiV00]

- A scalable system with well characterized qubits.
- The ability to initialize the system in a known state.
- A universal set of single-qubit and two-qubit gates.
- Limited decoherence over the typical gate duration.
- The ability to measure only a specific qubit.

These requirements are extremely challenging to fulfill, as they often appear contradictory. For example, some qubit implementations are notoriously weakly coupled to their environment. This is great from the point of view of decoherence, but limits the gate operation time. For this reason, different qubit architectures are often benchmarked considering the number of consecutive operations achievable within the decoherence timescale. In this perspective, a wide variety of qubit implementations are investigated, each having their assets and drawbacks.

Historically, the focus was mainly on atomic physics, with the development of ion traps and the first qubit demonstrations, borrowing techniques from the Nuclear Magnetic Resonance (NMR) community.[Rai01; Van01] Nowadays, a large variety of physical qubit realizations have been reported, such as photonic circuits[Cre11; Pol09], superconducting Josephson junctions,[Bar14; Nak99] defects in diamonds or other materials[Aws18; Jel04; Ken02], and many others. In 1998, Loss and DiVincenzo[Los98] proposed to use quantum dots in semiconductor materials to control individual electron spins as qubits. The main advantage of this proposal are the pre-existing fabrication techniques and equipments developed for decades by the silicon transistor industry, facilitating the scale-up towards a many-qubits processor. Notably, recent qubit demonstrations have been made using a Metal-Oxide-Semiconductor (MOS) architecture in silicon, widely used in the microelectronics industry.[Pla12; Vel14] In addition, using isotopically purified substrate lead to great improvement of the qubit coherence time, approaching 10^3 operations before the spin information is lost.[Tyr12; Yon18] Finally, error correction protocols (similar to the ones used in RAM technology) have been proposed to accommodate for imperfect qubits,[Fow12; Ste96] at the cost of an increase in the number of required qubits, again favoring a scalable architecture.

Following early demonstration of one-[Kop06] and two-qubit operations[Pet05] in semiconductors, the focus is now mainly on scaling up to a network of interconnected qubits. In this framework, most architectures propose to build arrays of quantum dots, each containing a few electrons and coupled to their nearest neighbor.[Mor18; Tha12; Zaj16] The control of the charge configuration and dot-to-dot coupling is a challenging milestone, and requires a large amount of electrical connections. For this reason, other options have been studied, such the creation of smaller arrays acting as computational nodes interconnected by quantum links.[Van17] The requirements on such a quantum link are rather strong, as they must couple arbitrary nodes on fast ($\sim$ ns) timescales, while preserving the quantum coherence the system. Several long-range coupling mechanisms have been proposed, such as placing the system in a photonic cavity[Lan18; Mi18], using a large quantum dot[Mal19] or a floating gate[Tri12] as a mediator, or shuttling the electrons themselves. This last technique relies on a moving trapping potential, either generated by sequential electrical pulses[Baa16; Mil19] or an acoustic wave propagating in a piezoelectric material[Lim05], to transport electrons over several micrometers. This shuttling protocol has experimentally been demonstrated[Her11; McN11] for single electrons, and results obtained on a large spin ensemble[Sto05] seem to indicate that the spin information can be preserved during this transfer.

In this work, we exploit a Surface Acoustic Wave (SAW), propagating in a GaAs/AlGaAs heterostructure, to realize a spin-preserving electron transfer and study its fidelity. In

particular, we study the impact of the spin-orbit interaction on individual electron spins in motion, and demonstrate a remote entanglement between two electron spins separated by 6 µm. The first chapter of this thesis introduces the relevant concepts used in this work, from electron spin isolation and readout to their controlled transfer via the SAW. In the second chapter we present the experimental setup, covering all the electronic, cryogenic and fabrication techniques required to perform the experiments. The third chapter presents how we control and read-out the charge state of the system, as well as an extensive study of the SAW-assisted transfer protocol. In particular, we develop a delay-controlled sending procedure of two electrons with a nanosecond resolution. In chapter four, we cover the spin initialization, readout and manipulation techniques, using a double quantum dot. We study the spin mixing process due to hyperfine interaction with the nuclear spin bath, and realize a two-qubit SWAP gate. Finally, in the last chapter we sequentially transfer two electrons initially in an entangled (singlet) spin state, and observe an interference pattern, signature of the coherent nature of the SAW transfer protocol and driven by the spin-orbit interaction. We exploit this transfer protocol as a Bell measurement, demonstrating that the entanglement is preserved while the electrons are separated.

CHAPTER 1

Isolation and manipulation of electron spins : state of the art

In this chapter, we introduce the underlying physical phenomena exploited to control individual electrons and their spin. We first present the substrate and how quantum dots containing few electrons are realized and probed. We then introduce how we can access the spin degree of freedom of these electrons, using various spin to charge conversion mechanisms. We study the effect of the environment, and in particular electrical noise and hyperfine coupling with the surrounding nuclei, and establish the single-spin and exchange operations that will be used in the following work. We finally develop how a surface acoustic wave can be used as a electron conveyor belt to transport spin information across a nanostructure.

1.1 Formation of GaAs quantum dots

A quantum dot is three-dimensional confinement potential which can trap electrons or holes on a scale of the order of their Fermi wavelength. They thereby exhibit wave-like properties and cannot be considered as purely classical particles, but need to be treated as quantum objects with the quantum mechanics formalism, such as the Shrödinger equation. In the last decades, several implementations of these quantum dots have been presented, such as self-assembled[Kle96], laterally[Kou97] or vertically[Kou01] defined quantum dots in a semiconductor, single molecules[Par02] or carbon nanotubes.[Dek99; McE00] In this work, we isolate a few electrons in a laterally defined GaAs double quantum dot and tune their confining electrostatic potential to perform charge and spin manipulation.

1.1.1 Substrate and lateral confinement

Due to the advanced control on semiconductor fabrication techniques, such structures are now being produced with highly reproducible characteristics. This work is based on a GaAs/AlGaAs heterostructure. At the interface between these two semiconductors of different gaps, a two-dimensional electron gas (2DEG) is formed by doping the substrate with Si donors. Electrons are accumulated in this 2DEG and their confinement along the growth axis is typically 16 meV $\approx$ 186 K,[Nak94] and about one order of magnitude greater than the one achieved in the (x,y) plane. At cryogenic temperatures, the electron motion along this axis is quantized and only the ground state is occupied, which allows us to consider the structure as a true two-dimensional system. Such heterostructures are

typically used for high electron mobility transistors (HEMTs), and have lead to numerous breakthrough in understanding the physics of 2D, 1D and 0D systems during the past decades.[Mei90; Par02]

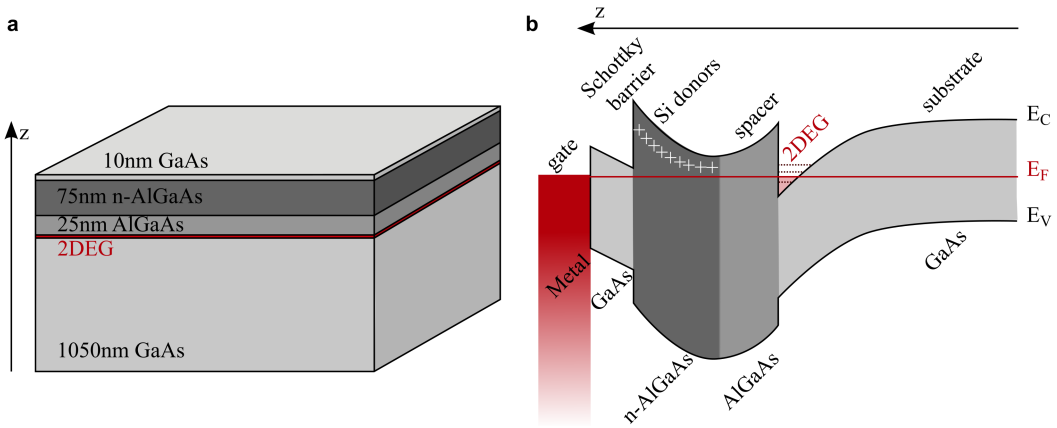

Figure 1.1: Two-dimensional electron gas. a. Scheme of the heterostructure composition. The 2DEG is located at the AlGaAs/GaAs interface, 110 nm below the surface. b. Band structure along the growth axis. The implanted silicon atoms provide electrons to the 2DEG, and are responsible for the bending of the bands, which create a strong confinement along the z-axis.

In this thesis, we use GaAs/$Al_{0.33}Ga_{0.67}As$ heterostructures realized by A.D. Wieck from the Ruhr-University in Bochum, Germany. They are grown by molecular beam epitaxy (MBE), one atomic layer at a time, which allows a great control on the heterostructure composition and extremely sharp interfaces in the growth direction. By carefully adjusting the doping concentration and its location in the heterostructure, the scattering events between electrons and ionized donors are greatly reduced, enhancing the electron mobility. The obtained mobility for these MBE defined 2DEG are typically three orders of magnitude greater than in the case of a grown oxide (e.g. Si/SiO2) interface.[Ang07; Law19; Li13; Uma09]

Our 2DEG is located approximately 110 nm below the sample surface, and has a electron mobility and density of:

$$\begin{aligned} \mu_e &= 1.5 \times 10^6 \,\mathrm{cm^2 V^{-1} s^{-1}} \\ n_e &= 2.6 \times 10^{11} \,\mathrm{cm^{-2}} \end{aligned} \tag{1.1}$$

From this characteristic values we can infer the Fermi wavelength, and verify that it is indeed greater than the spatial extension in the z-axis ($L_z \approx 6\,\mathrm{nm}$[Nak94]):

$$\lambda_F = \sqrt{\frac{2\pi}{n_e}} = 49\,\mathrm{nm} > L_Z \tag{1.2}$$

We can also determine the mean free path of the electrons in the (x,y) plane, product of

the Fermi velocity v_F and the momentum relaxation time τ_e:

$$l_e = v_F \tau_e = \frac{\hbar \mu_e \sqrt{2\pi n_e}}{e} = 13\,\mu\text{m} \tag{1.3}$$

This large mean-free path allows us to define micro-scale structures that are, in principle, free of any impurity, assuring a ballistic transport. However, in our experiment we will be influenced by the electrostatic potential disorder, perturbing the electron trajectory from a straight line.

Lateral confinement

To form quantum dots, we need to add lateral confinement to the one already provided by the material along the growth axis (z axis). We deposit metallic gates on top of the substrate, that we bias with a negative voltage. Electrons located in the 2DEG underneath the gate are repelled by the electrostatic potential induced at the 2DEG level. By carefully engineering the gate geometry and tuning their applied voltage, quantum dots can be formed and controlled. The gates we use are typically quite thin ($t = 15\,\text{nm}$), and their width is adjusted depending on the magnitude of the desired effect on the 2DEG ($w = 20 - 60\,\text{nm}$). Because the contact between between the metallic gate and the GaAs substrate forms a Schottky barrier, we can apply large negative voltages without any current flowing to the 2DEG. In some cases, an insulating layer can be deposited before the metallic gates to allow positive voltages and provide more versatility in the electrostatic potential control. However, trapped charges in this oxide layer can induce charge noise felt by the quantum dots, and therefore this technique was not used in this work.

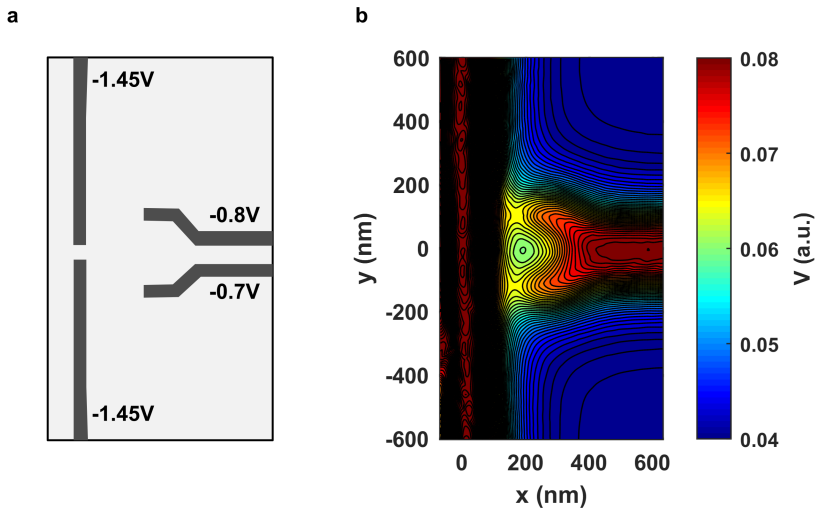

Figure 1.2: Sensing dot. a. Gate geometry and applied voltages. All four gates are 40 nm wide, and used to define a 200 nm wide quantum dot. **b.** Simulated electrostatic potential at the 2DEG depth.

To visualize the potential landscape felt by the electrons, we use a Poisson solver to

simulate the gate effect at the 2DEG depth. This allows us to refine the sample design and study the expected effect of each gate on our nanostructure. We can see Fig. 1.2. how a quantum dot is formed by patterning four thin (40 nm) metallic gates on top of the sample and applying negative voltages.

1.1.2 Energy scales

In this section, we study the energy cost of the addition of one electron into the quantum dot, considering firstly the classical Coulomb repulsion with the other charges already in the dot, and secondly discussing the orbital energy coming from quantum mechanical properties. We consider a quantum dot of size $L = 100\,\text{nm}$ containing a small number ($N \sim 2$) of electrons, and evaluate the chemical potential of the system, defined as the energy needed for the addition of one electron.

Capacitive model

The usual semi-classical approach to model quantum dots starts by considering a charged island capacitively coupled to different reservoirs of fixed potentials V_i. Noting $C_{\text{tot}} = \sum C_i$ the total capacitance of the island, its stored energy is then:

$$U_{\text{C}}(N) = \frac{Q^2}{2C_{\text{tot}}} = \frac{(Ne)^2}{2C_{\text{tot}}} \tag{1.4}$$

and the chemical potential is:

$$\mu_{\text{C}}(N) = U_{\text{C}}(N) - U_{\text{C}}(N-1) = (N - \frac{1}{2})E_{\text{C}} \tag{1.5}$$

with $E_{\text{C}} = \frac{e^2}{C_{\text{tot}}}$ the so-called charging energy. To evaluate this charging energy, we consider the quantum dot as charged disk of diameter L and calculate the self-capacitance of this disk:

$$C_{\text{self}} = 4\varepsilon_r\varepsilon_0 L = 46\,\text{aF} \tag{1.6}$$

giving a charging energy of $E_{\text{C}} = 3.5\,\text{meV}$. This value is an overestimation, because our simple disk model does not take into account the additional coupling to the metallic gates on top of the substrate or the electron reservoirs in the 2DEG, which would increase the total capacitance C_{tot}. It is however a good approximation, as a charging energy of the order of a few meV is usually found in GaAs quantum dots of this size.[Han07]

Orbital energy

As mentioned before, the fact that our quantum dots are smaller than the Fermi wavelength of the electrons in the 2DEG means their motion becomes quantized into distinct orbitals. To evaluate the energy separation between these orbitals, we consider a particle in a 2D harmonic potential of characteristic dimension $R = L/2$:

$$V(r) = \frac{1}{2}m^*\omega_0^2 r^2 \tag{1.7}$$

with ω_0 the angular frequency of the oscillator and $m^* = 0.067m_0$ the effective mass of electrons in GaAs. Solving the Schrödinger equation leads to the following energy levels:

$$E_{\text{orb}}(n_x, n_y) = \hbar\omega_0 \left(n_x^2 + n_y^2 + \frac{1}{2} \right) \tag{1.8}$$

The energy separation can be evaluated by considering an harmonic oscillator of total energy $\frac{\hbar\omega_0}{2}$. The kinetic energy of the system is zero at a distance R, leading to:

$$\begin{aligned} V(R) &= \frac{\hbar\omega_0}{2} \\ \Leftrightarrow \frac{1}{2} m^* \omega_0^2 R^2 &= \frac{\hbar\omega_0}{2} \\ \Leftrightarrow \omega_0 &= \frac{\hbar}{m^* R^2} \end{aligned} \tag{1.9}$$

Taking into account the size of the quantum dot, we obtain an orbital energy separation:

$$\Delta E_{\text{orb}} = \hbar\omega_0 = \frac{4\hbar^2}{m^* L^2} = 0.45\,\text{meV} \tag{1.10}$$

This orbital energy being several times smaller than the charging energy, we can conclude that the chemical potential of the quantum dots is mainly determined by the classical Coulomb repulsion. Since this charging energy corresponds to a temperature of approximately 12 K, cooling the system down to cryogenic temperatures will allow us to control the charge configuration in our quantum dots with a single electron precision.

1.1.3 Charge sensing

To probe the occupancy of quantum dots, we define local electrometers sensitive to nearby charges, such as a quantum point contact (QPC) or a single electron transistor (SET).

A QPC is a small 1D constriction in the 2DEG, through which a current is forced to pass close to the probed quantum dot.[Wee88] At cryogenic temperatures and with a sufficient confinement conductance plateaus start to appear, between which the conductance is extremely sensitive to the electrostatic environnement.[Sch04] By recording the current through the QPC and varying the quantum dot potential, we can see on top of a general trend quite sharp signal shifts, corresponding to single electrons tunneling to or from the quantum dot. From the sign of this shift we can infer the tunneling direction (e.g. an electron coming towards the QPC has the same effect as a more negative QPC voltage and results in a lower conductance).[Gus09; Spr02] We can also probe multiple quantum dots using the same QPC, as the signal shift amplitude depends on the distance from the QPC.[Elz03]

A single electron transistor (SET) is a quantum dot coupled to two electron reservoirs biased with a small voltage (typically $V_{\text{bias}} = 150\,\mu\text{V}$). Because of its discrete chemical potential levels, the conduction through this dot is only allowed if a level sits within the bias window, and otherwise blocked (the so-called Coulomb blockade), leading to the appearance of Coulomb peaks when the SET potential is swept.[Han07] These peaks are

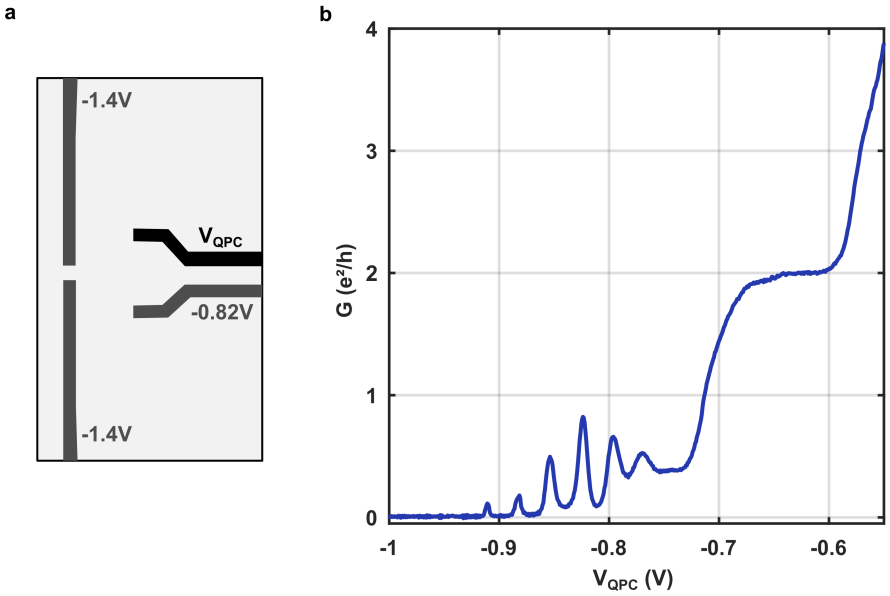

Figure 1.3: QPC and SET. Electrometer conductance as a function of the gate voltage V_{QPC}. A 200 µV bias is applied and the 2DEG contact resistance of 500 Ω is taken into account. As V_{QPC} gets more negative we observe conductance plateaus, multiples of $2e^2/h$, signature of a QPC behavior. For $V_{\mathrm{QPC}} < 0.75$ V, a quantum dot is formed and Coulomb peaks appear. For $V_{\mathrm{QPC}} < 0.92$ V, the electrometer is completely pinched-off, and no current flows through it.

extremely sharp and their position is sensitive to the surrounding charges, which allows us to monitor changes in the quantum dot configuration. The SET sensitivity can be several times larger than the one achieved with a QPC, with current shifts of up to several nA per electron (for $V_{\mathrm{bias}} = 150$ mV).[Bar10; Rei07]

1.2 Electron spins in GaAs quantum dots

Now that we have established how to isolate a few electrons and measure their charge configuration using local electrometers, we study the spin degree of freedom of these electrons. We first focus on the one- and two-electron spin states of a single quantum dot, focusing on their wavefunction parity and the relevant energy scales. Then, we present the two-electron spin states of a double quantum dot, and study the low and high interdot coupling regime. Finally, we describe several spin readout techniques, involving an electron exchange with the reservoir or between adjacent quantum dots.

1.2.1 Spin states in a single quantum dot

Here we focus on the case of a single quantum dot populated with either one or two electrons, submitted to an external magnetic field $B_z > 0$. We note $|\uparrow\rangle$ a spin aligned with this magnetic field (resp $|\downarrow\rangle$ for an anti-aligned spin), and name $|g\rangle$ the first and $|e\rangle$ the second orbital states.

Single electron

For the single electron case, the ground state naturally corresponds to the electron occupying the lowest orbital $|g\rangle$. The finite magnetic field lifts the degeneracy between the two spin configurations $|\uparrow\rangle$ and $|\downarrow\rangle$ by the Zeeman splitting:

$$\begin{aligned} E_{\mathrm{Z}} &= +\frac{1}{2} g \mu_B B_z \quad \text{for} \quad |\uparrow\rangle \\ E_{\mathrm{Z}} &= -\frac{1}{2} g \mu_B B_z \quad \text{for} \quad |\downarrow\rangle \end{aligned} \tag{1.11}$$

where μ_B is the Bohr magneton and $g = -0.425$ is the GaAs g-factor.[Now07; Wei77] Because of the g-factor sign, the ground spin state of the system corresponds to the electron spin aligned with the external magnetic field ($|\uparrow\rangle$ for $B_z > 0$).

Two electrons

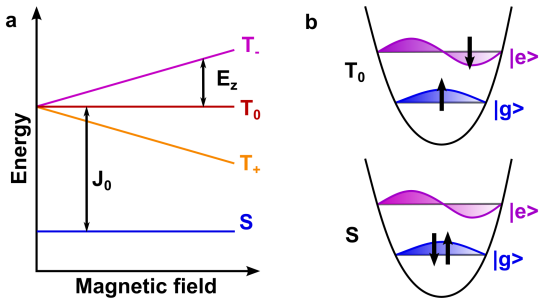

Figure 1.4: Energy diagram of a single quantum dot. a. Four ground spin states a single quantum dot populated by two electrons. The S and T_0 states are separated by the exchange energy J_0, and the triplet degeneracy is lifted by the Zeeman splitting $E_{\mathrm{Z}} = g\mu_{\mathrm{B}}B$ under an external magnetic field B. **b.** Orbital part of the ground S and T_0 states. The singlet spin state is the only case where both electrons can occupy the lowest orbital.

Since electrons are fermions, their wavefunction must be anti-symmetric with respect to the exchange of two particles. As it is the product of an orbital part and a spin part, this means that one of them is anti-symmetric and the other is symmetric. Therefore, there is only one configuration in which both electrons occupy the ground orbital, called the singlet spin state:

$$|S\rangle = |gg\rangle \otimes \frac{|\uparrow\downarrow\rangle - |\downarrow\uparrow\rangle}{\sqrt{2}} \tag{1.12}$$

Higher in energy we then have the triplet spin states, where the electrons occupy different orbitals:

$$\begin{aligned} |T_0\rangle &= \frac{|ge\rangle - |eg\rangle}{\sqrt{2}} \otimes \frac{|\uparrow\downarrow\rangle + |\downarrow\uparrow\rangle}{\sqrt{2}} \\ |T_+\rangle &= \frac{|ge\rangle - |eg\rangle}{\sqrt{2}} \otimes |\uparrow\uparrow\rangle \\ |T_-\rangle &= \frac{|ge\rangle - |eg\rangle}{\sqrt{2}} \otimes |\downarrow\downarrow\rangle \end{aligned} \tag{1.13}$$

The $|S\rangle$ and $|T_0\rangle$ states are $m_S = 0$ states, whereas $|T_+\rangle$ and $|T_-\rangle$ have a non-zero magnetic moment $m_S = \pm 1$. The presence of the external magnetic field thus lifts the degeneracy between the triplet spin states, leading to the energy diagram presented on Fig. 1.4. In a single quantum dot, the ground $|S\rangle$ and $|T_0\rangle$ states are separated by the *exchange energy* $J_0 \approx 300\,\mu\text{eV}$. This energy splitting is the result of two competing factors: the difference in orbital energy is partly compensated by the lower Coulomb interaction for $|T_0\rangle$ due to its anti-symmetric orbital component.

Our two electron system possesses a multitude of excited states, all involving higher orbital states, to the exception of two excited singlets with orbital part $\frac{|ge\rangle+|eg\rangle}{\sqrt{2}}$ and $|ee\rangle$. However because these orbitals are symmetric, the two electron wavefunctions tend to overlap more than in a antisymmetric case, and the Coulomb interaction lifts these excited singlets higher in energy than the ground $|T_0\rangle$ state.

For a high external magnetic field ($|B_z| > 4.3\,\text{T}$), the $|T_+\rangle$ (or $|T_-\rangle$) state becomes the ground state of the system. As in this work we always work below this limit, the singlet spin state will always remain the ground state of the system.

1.2.2 Spin states in a double quantum dot

When two quantum dots are coupled, several charge configurations are possible for a given number of electrons isolated inside the structure. We focus on the case of a double quantum dot loaded with two electrons, noting E_C the charging energy associated with both electrons occupying the same dot, t_c the interdot tunnel coupling, $\varepsilon = V_R - V_L$ the energy detuning between the two dots and (N_L, N_R) the number of charges on the left and right dot respectively. In the (2,0), (1,1), (0,2) basis, the Hamiltonian for the singlet states are:

$$H_{|S\rangle} = \begin{pmatrix} E_c - \varepsilon & t_c & 0 \\ t_c^* & 0 & t_c \\ 0 & t_c^* & E_c + \varepsilon \end{pmatrix} \tag{1.14}$$

The $|T_0\rangle$ spin state has a similar Hamiltonian, with the addition of the exchange energy J_0 when both electrons are on the same site.

$$H_{|T_0\rangle} = \begin{pmatrix} E_c + J_0 - \varepsilon & t_c & 0 \\ t_c^* & 0 & t_c \\ 0 & t_c^* & E_c + J_0 + \varepsilon \end{pmatrix} \tag{1.15}$$

Finally, the $|T_+\rangle$ and $|T_-\rangle$ states are simply offset from the $|T_0\rangle$ state by the Zeeman energy

$$H_{|T_\pm\rangle} = H_{|T_0\rangle} \pm E_\text{Z} \begin{pmatrix} 1 & 0 & 0 \\ 0 & 1 & 0 \\ 0 & 0 & 1 \end{pmatrix} \tag{1.16}$$

As expected, we can see that for large detunings $\varepsilon \to \pm\infty$ both electrons are in the same quantum dot with spin states identical to the single-dot case. We will now study the energy diagram for moderate detunings in the weak ($t_c/h \sim 1\,\text{GHz}$) or strong ($t_c/h \gg 10\,\text{GHz}$) coupling regimes.

Weak coupling

For totally uncoupled quantum dots, the ground state follows three asymptotes:

$$\begin{aligned} E_{|S_{(2,0)}\rangle} &= E_\text{C} - \varepsilon \quad \text{for} \quad \varepsilon > E_\text{C} \\ E_{|S_{(1,1)}\rangle} &= 0 \qquad\quad \text{for} \quad |\varepsilon| \leq E_\text{C} \\ E_{|S_{(0,2)}\rangle} &= E_\text{C} + \varepsilon \quad \text{for} \quad \varepsilon < -E_\text{C} \end{aligned} \tag{1.17}$$

Increasing the interdot tunnel coupling hybridizes the $|S_{(2,0)}\rangle$ and $|S_{(1,1)}\rangle$ (respectively $|S_{(1,1)}\rangle$ and $|S_{(0,2)}\rangle$) states when their energy is close, creating avoided crossings for $\varepsilon \approx +E_\text{C}$ (resp. $\varepsilon \approx -E_\text{C}$), visible on Fig. 1.5. The same effect affects the triplet states, with avoided crossings for $\varepsilon \approx \pm(E_\text{C} + J_0)$.

At large detuning, the S-T_0 energy splitting is equal to the exchange energy in a single quantum dot $J(\varepsilon \to \pm\infty) = J_0$. It is interesting to note that at zero detuning $\varepsilon = 0$ this splitting has a quadratic dependance with the interdot tunnel coupling:

$$\begin{aligned} J(\varepsilon = 0) = E_{|T_{0(1,1)}\rangle} - E_{|S_{(1,1)}\rangle} &= \frac{2t_c^2}{E_\text{C}} - \frac{2t_c^2}{E_\text{C} + J_0} \\ &= \frac{2J_0}{E_\text{C}(E_\text{C} + J_0)} t_c^2 \end{aligned} \tag{1.18}$$

For $t_c/h \sim 1\,\text{GHz}$, this splitting would correspond to a magnetic field of 0.1 mT. In practice, small magnetic field difference between the two quantum dots (such as a g-factor difference or the hyperfine coupling with the surrounding nuclei) will overcome and favor either $|\uparrow\downarrow\rangle$ or $|\downarrow\uparrow\rangle$, making one of these two states the ground state of the system in (1,1).

Strong coupling

Increasing the interdot tunnel coupling t_c leads to an energy splitting between $E_{|S_{(1,1)}\rangle}$ and $E_{|T_{0(1,1)}\rangle}$ larger than any of these magnetic field inhomogeneities, allowing the singlet state to remain the ground state of the system even in (1,1) at zero detuning, and preventing any mixing.[Ber15b]

This can be seen as a limit where the two quantum dots are so coupled that two electrons always "feel" each-other, even when they are separated each in one quantum dot. As we will see in the following sections, we exploit our control over the interdot tunnel coupling to shuttle a singlet spin state from the (2,0) to the (0,2) configuration without any mixing process. We can see Fig. 1.6. a map of the $S - T_0$ splitting, as well as the position of the $S - T_+$ avoided crossing, and the different interdot coupling regimes.

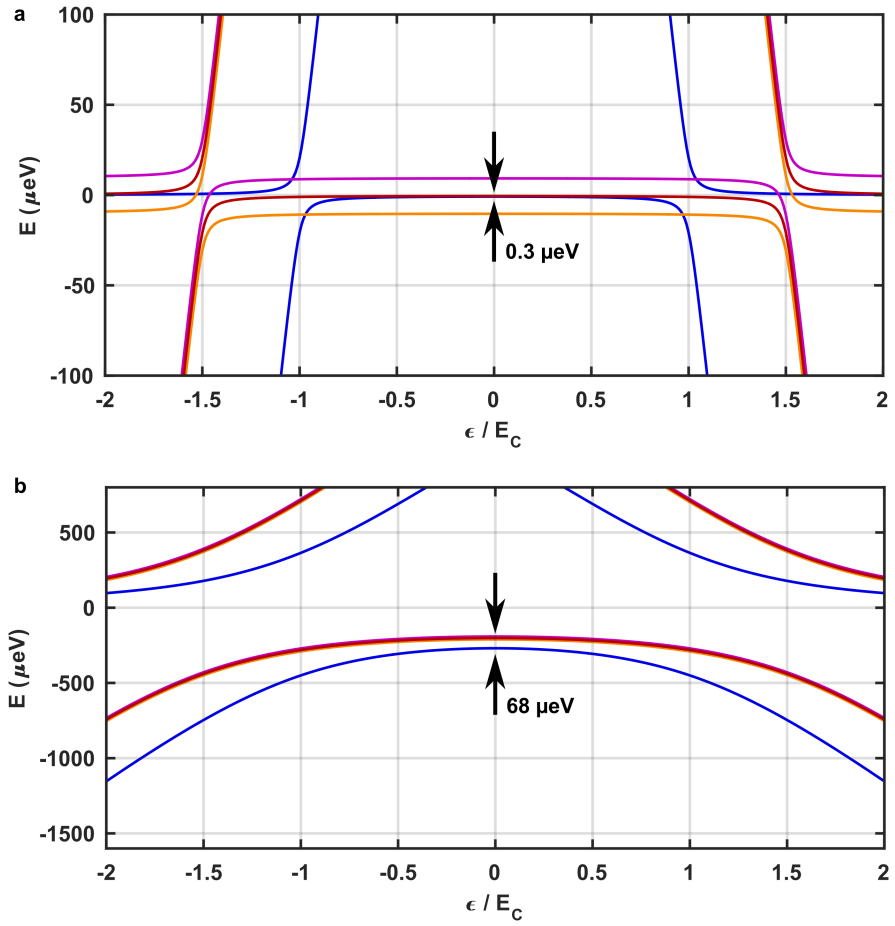

Figure 1.5: Energy diagram of a double quantum dot. Energy diagram as a function of detuning for a intermediate (**a.** $t_c = 5\,\mathrm{GHz}$) and high (**b.** $t_c = 100\,\mathrm{GHz}$) interdot tunnel coupling. The charging energy and exchange interaction are respectively $E_c = 1\,\mathrm{meV}$ and $J_0 = 500\,\mu\mathrm{eV}$, and the magnetic field is $B_z = 500\,\mathrm{mT}$. We observe avoided crossings between the (1,1) and (2,0) (resp. (0,2)) configurations for a same spin state, of amplitude $2t_c$. At zero detuning, the S-T_0 splitting is proportional to t_c^2, assuring a singlet state preservation for the high coupling regime.

1.2.3 Spin readout techniques

Now that the energy diagrams for two electrons in single and double quantum dots are understood, we can present several techniques used to probe the energy splitting of the system, and read out its spin state. This measurement usually relies on a spin to charge conversion mechanism, followed by the previously described charge readout. It either involves an electron exchange with a neighbor electron reservoir or exploits interdot coupling to discriminate the spin states based on the charge occupancy of the system. Here, we introduce several techniques, discussing their fidelities, advantages and drawbacks, again focusing on a double quantum dot containing two electrons.

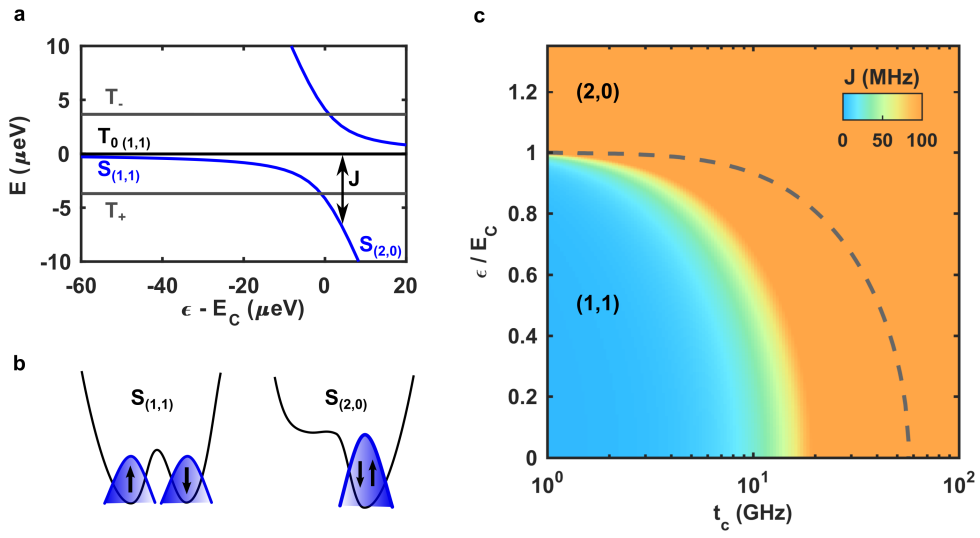

Figure 1.6: S-T_0 splitting. Exchange energy J as a function of the detuning and interdot tunnel coupling. For $\varepsilon/E_c > 1$, the two electrons are in the same quantum dot (configuration (2,0)). At $\varepsilon = 0$, the electrons are separated in the (1,1) configuration, and their exchange energy is set by the interdot tunnel coupling. Mixing processes occur if J is lower than the magnetic field inhomogeneities ($\sim 60\,\mathrm{MHz}$). The $S - T_+$ avoided crossing for an external magnetic field of 150 mT is indicated by the gray dashed line.

Energy-selective readout

As we have previously discussed, the two-electron spin basis for a single quantum dot is the singlet-triplet basis, split at zero magnetic field by the exchange energy:

$$J_0 \approx 300\,\mu\mathrm{eV} \approx 3.5\,\mathrm{K} \tag{1.19}$$

Besides, the density of states in the reservoir follows a Fermi distribution:

$$f(E) = \frac{1}{1 + \exp\left(\frac{E-\mu}{k_B T}\right)} \tag{1.20}$$

At cryogenic temperatures ($T \sim 100\,\mathrm{mK}$), we can therefore approximate the density of states as a step function, with every states below a Fermi energy E_F occupied and all states above empty. By tuning the quantum dot potential so that this Fermi energy sits between the singlet and triplet states, the tunneling-out of the singlet spin state is suppressed as no state with the same energy is available in the reservoir, and in this case two electrons remain in the quantum dot. On the other hand, a triplet spin state will lead to one electron leaving the quantum dot to the reservoir, followed by a tunnel-in of one electron to form a singlet state.[Meu06] If the tunnel-rate is slower than the measurement speed, we can observe this temporary charge deficit in the quantum dot (see Fig 1.7.a) and infer a triplet state.

This mechanism, called Elzerman spin readout,[Elz04] can also be used to read single-spin

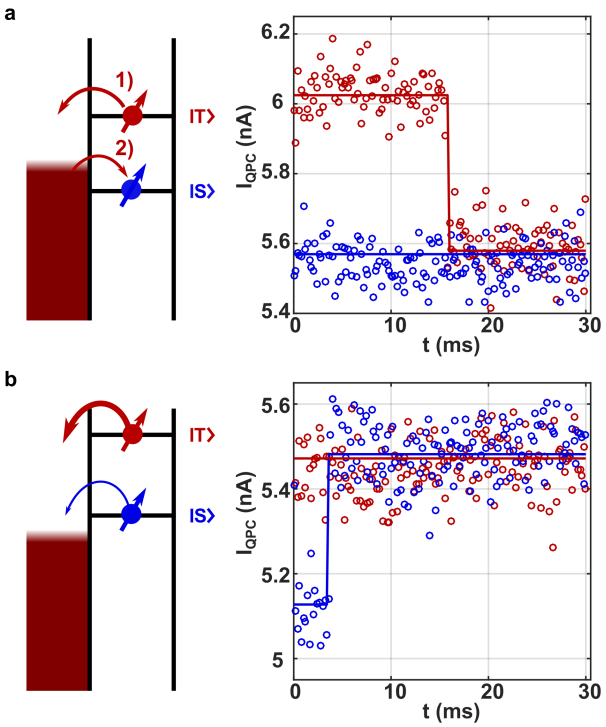

Figure 1.7: Spin to charge conversion. top. Energy-selective spin readout. A singlet spin state lies below the Fermi energy of the reservoir and the quantum dot charge is unchanged. A triplet spin state leads to one electron tunneling-out to the reservoir, followed by a re-loading in a singlet spin state. The experimental data shows an evidence of this re-loading process in the case of a triplet spin state (the charge occupancy jumps from 1 to 2 electrons). **bottom.** Tunnel-rate-selective spin readout. While both state tunnel to the reservoir, this process occurs at a faster rate for a triplet spin state. In the experimental data, we can see the tunnel-out of a singlet state (jump from 2 to 1 electrons). The triplet state tunnel-out rate is above our measurement speed, and thus happens before the first point is acquired.

states, providing a large enough external magnetic field to split the $|\uparrow\rangle$ and $|\downarrow\rangle$ states. However, for both single- and two-electron spin states this readout technique is extremely sensitive on electrical noise, as the dot potential needs to be precisely tuned with respect to the reservoir, which affects the spin measurement fidelity.

Tunnel-selective readout

The tunnel selective readout (TSR) also relies on charge tunnel to the reservoir, but exploits the orbital difference between the singlet and the triplet states. As the triplet states are composed of a higher orbital $|e\rangle$, their spatial extension is slightly greater, analogous to a s and p orbitals in atoms. Therefore, their coupling to the surrounding reservoirs, and subsequently their tunnel-rate, are larger than in the case of a singlet spin state.[Han05]

Experimentally, the quantum dot potential is raised so that both the singlet and triplet states are above the Fermi energy, and one electron tunnels to the reservoir. The tunnel-out

time is stochastic, but on average faster for triplet states. If this difference is large, we can set a threshold and determine the initial spin state (see Fig 1.7.b.).

The main asset of this technique is that the tuning of the dot potential is less critical, as it simply needs to be above the Fermi energy. However, the measurement fidelity depends on the tunnel-rate contrast which varies with the quantum dot geometry and is typically around one order of magnitude.

Isolated tunnel-selective readout

In the following work, we used our ability to control the reservoir coupling on µs timescales to realize a particular form of tunnel-selective readout. The coupling to the reservoir is open only for a time τ that satisfies $\Gamma_S \ll \frac{1}{\tau} \ll \Gamma_T$, and closed before the singlet state tunnels-out. A singlet state will then correspond to two electrons remaining in the quantum dot, whereas a triplet state is associated with only one remaining electron.

This technique has the great advantage of decoupling the measurement time from the tunnelling time, as once the tunnel coupling is turned off the charge can be read-out for several hundreds of ms if needed. However, its fidelity still relies on a high contrast between the singlet and triplet tunnel-rates to the reservoir.

Pauli spin blockade

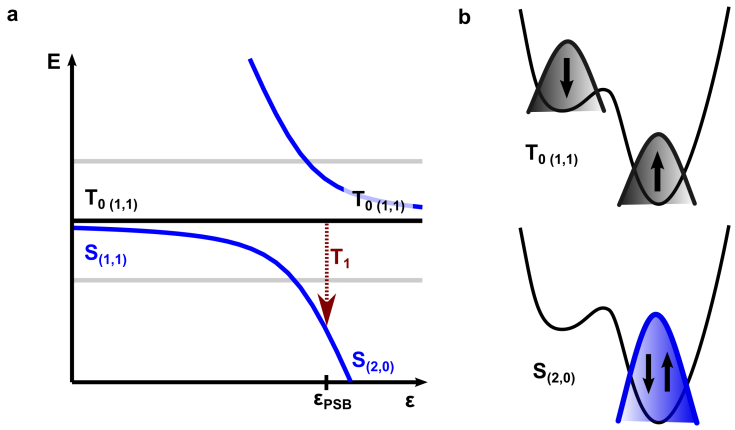

Figure 1.8: Pauli spin blockade. a. Energy diagram close to the Pauli spin blockade position. **b.** For a specific detuning, a triplet spin state is in a (1,1) charge configuration, while a singlet spin state is in the (2,0) configuration. The relaxation rate of the triplet state, T_1, is indicated in **a.** by the red arrow.

All spin readout techniques presented so far rely on a tunnel coupling to a electron reservoir, which can be an obstacle to scale-up a quantum dot array. This is why several alternative readout methods using interdot coupling were developed, based on a mechanism called Pauli spin blockade (PSB).

As we have seen in section 1.2.2, the tunnel coupling between two adjacent quantum dots creates a avoided crossing between the (2,0) and (1,1) charge states, appearing when both configurations are close in energy. However, because the triplet states have an additional exchange energy J_0 in the (2,0) configuration, their avoided crossing appear for a larger detuning ε.

Therefore, we can find a particular detuning range where the charge ground state for a singlet spin state is (2,0), whereas the triplet states are all in the (1,1) configuration. This different charge distribution depending on the spin state is measurable by our charge detector, providing a fast and non-destructive spin measurement (the electrons stay in the same spin configuration after the measurement if they are in a pure state).[Joh05]

The main drawback of this technique is the smaller signal as we only measure a difference in electron repartition inside the structure instead of a different total number of charges. Depending on the position of the charge detector, the contrast between (1,1) and (2,0) may be small, and will definitely be smaller than the contrast obtained via TSR. It also requires a precise control of the detuning and a fast charge measurement, as the relaxation processes are typically quite fast in a PSB position ($\sim 10\,\mu s$). However, if the signal to noise ratio is sufficient this technique provides a fast, scalable and non-destructive spin readout mechanism, nowadays widely used in semiconductor spin qubits.

Spin latching

A recent work by Harvey-Collard *et al*[HC18] presents an enhanced version of Pauli spin blockade, exploiting a double quantum dot with different tunnel couplings to a common reservoir. This creates a tendency for one quantum dot to exchange electrons with the reservoir through the other quantum dot, and only when its chemical potential is in resonance. In a PSB position, a singlet spin state corresponds to a (2,0) configuration, allowing an electron to enter the right quantum dot, and the system ends up in a (2,1) configuration. On the other hand, a triplet state remains blocked in a (1,1) configuration, preventing a third electron from entering the double quantum dot until a relaxation process occurs.

This method increases the PSB signal, as we come back to detecting a different total number of electrons in the structure. However, it again requires one reservoir per double quantum dot, as well as well-controlled tunnel couplings. The single-shot fidelities of this readout scheme are extremely high, with a reported 99.3 % fidelity for a silicon spin qubit.[Urd19]

Quantum capacitance

A very promising technique for scalability purposes, that does not require a electron reservoir nor a local electrometer, is the measure of the quantum capacitance. It relies on the realization of a resonant circuit connected to one of the metallic gate controlling the detuning, whose resonant frequency is sensitive to the charge susceptibility of the quantum dot.

At a PSB position, the singlet spin state has its (1,1) and (2,0) charge configurations in resonance, whereas the triplet states is blocked in (1,1). This leads to a larger electrical susceptibility for the singlet state, which is seen by the resonant circuit as a small additional capacitance, slightly shifting its resonant frequency.

In other words, we can define a quantum capacitance, proportional to the curvature of the energy states:

$$C_Q \propto -\frac{\partial^2 E}{\partial \varepsilon^2} \tag{1.21}$$

Near the $|S_{(1,1)}\rangle$ - $|S_{(2,0)}\rangle$ avoided crossing the singlet quantum capacitance increases, typically reaching a few fF for a GHz interdot coupling. The associated shift in resonant frequency depends on the LC tank circuit, with typical values below 1 MHz.[Col13]

1.3 Relaxation and decoherence mechanisms

Now that the we introduced the energy diagram for two electron spins in a double quantum dot, and how to perform spin readout, we focus on the influence of the environment on this spin information. This coupling to the environment can be exploited as a knob to perform single and two-qubit operations.[Fol09; Now07] However, when uncontrolled, these mechanisms lead to decoherence (loss of spin information) on extremely short timescales in GaAs. In this section, we try to categorize the different kinds of environmental perturbation, and discuss the timescale on which they occur.

1.3.1 Bloch sphere, relaxation, decoherence and dephasing

An important tool to introduce once we start talking about quantum information is the Bloch sphere. Whereas a classical bit in either 0 or 1, a quantum bit (qubit) can be in a coherent superposition of its two eigenstates $|0\rangle$ and $|1\rangle$:

$$|\psi\rangle = a\,|0\rangle + b\,|1\rangle \tag{1.22}$$

where a and b are complex numbers and $|a|^2 + |b|^2 = 1$. This normalization condition naturally describes a sphere of radius 1 (the Bloch sphere), and thus we can equivalently define our state by two angles θ and ϕ such as:

$$|\psi\rangle = \cos\left(\frac{\theta}{2}\right)|0\rangle + \sin\left(\frac{\theta}{2}\right)e^{i\phi}\,|1\rangle \tag{1.23}$$

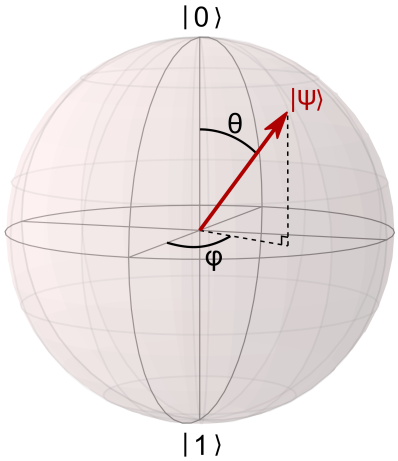

Figure 1.9: Bloch sphere. Representation of a single-qubit quantum state by two angles θ and ϕ. The probability to measure the qubit in the $|0\rangle$ state is $\cos^2(\theta/2)$, and ϕ is the phase of the qubit.

Our quantum state is now represented by two real numbers, θ being the colatitude and

ϕ the azimuthal angle on the Bloch sphere (Fig. 1.9). Each single-qubit quantum state can therefore be mapped to a point in the Bloch sphere, a notation quite often used when discussing qubit operations.

Environmental effects on a qubit

The effect on the environment on the qubit can be split in two categories, relaxation and dephasing, affecting respectively the latitude and phase of the spin state.

Relaxation corresponds to a jump towards the ground state $|0\rangle$, with a loss of energy towards the environment. Representing the average trajectory on the Bloch sphere for several single-shot realizations, this phenomenon is associated with a tendency for θ to decrease, collapsing the state towards the north pole. This process occurs on a timescale called T_1, and is for a GaAs singlet-triplet qubit on the order of a few ms. In our structures, the phonon bath has been identified as the main energy loss mechanism[Meu07], this interaction being mediated by the spin-orbit coupling, leading to an Hamiltonian of the form:[Gol04]

$$\begin{aligned} H_{\text{eff}} &= \frac{1}{2} g \mu_{\text{B}} \boldsymbol{\delta B}(t) \cdot \boldsymbol{\sigma} \\ \text{with } \boldsymbol{\delta B}(t) &= 2\boldsymbol{B} \times \boldsymbol{\Omega}(t) \end{aligned} \tag{1.24}$$

More generally, a dephasing process affects the qubit phase ϕ, with or without energy loss or gain. Dephasing occurs for example when a quantum operation is repeated on the same qubit (or applied simultaneously on many qubits). Because of slow fluctuations in the environment, each realization is performed with slightly different experimental conditions, leading to an uncertainty on the final state reached. Hyperfine interaction, as we will see in the next paragraph, is a good example of a dephasing process, responsible in GaAs quantum dots of the rather poor coherence time $T_2^* \approx 15\,\text{ns}$.

Some of these decoherence processes can be mitigated using clever dynamical decoupling techniques (e.g. Hann echo[Hah50], CPMG sequence[Blu11], nuclear polarization[Blu10]) exploiting the fact that the environment, however uncertain, remains constant throughout a single operation. Other decoherence mechanisms, on the other hand, are characteristic of a phase noise evolving faster than the operation time (typically $\gg 1\,\text{MHz}$), which cannot be suppressed via dynamical decoupling. Such high frequency processes arise from entanglement with uncontrolled particles or GHz charge noise. The different dynamical decoupling techniques thus are able to suppress some of the phase noise and probe its remaining part, giving rise a variety of characteristic timescales (T_2^{Hann}, T_2^{CPMG}) necessarily satisfying the inequalities:

$$T_2^* \leq T_2^{\text{Hann}}, T_2^{\text{CPMG}} \leq 2T_1 \tag{1.25}$$

These different timescales are characteristic of the material properties, as their origin vary greatly from one heterostructure to the other. Silicon quantum dots have for example coherence times T_2^* one order of magnitude larger than those obtained in GaAs, even more when the substrate is isotopically purified in the nuclear-spin-free ^{28}Si.[Ito14]

1.3.2 Hyperfine interaction

Each atom composing our heterostructure possess a non-zero nuclear spin ($I_{\mathrm{Ga}} = I_{\mathrm{As}} = \frac{3}{2}$ for Gallium and Arsenic, $I_{\mathrm{Al}} = \frac{5}{2}$ for Aluminum). They all interact with an electron spin contained in a quantum dot via the hyperfine interaction:

$$H_{\mathrm{HF}} = \sum_{k}^{N} A_k \boldsymbol{I_k} \cdot \boldsymbol{S} \tag{1.26}$$

where $\boldsymbol{I_k}$ and $\boldsymbol{S}$ are the spin operators of the nuclei k and the electron respectively. A_k is the interaction strength for the nuclei k,[Han07] proportional to the nuclear gyromagnetic ratio and the magnitude of the electronic wavefunction at the position $\boldsymbol{r_k}$:

$$A_k \propto \gamma_{n,k} \, |\psi_e(\boldsymbol{r_k})|^2 \tag{1.27}$$

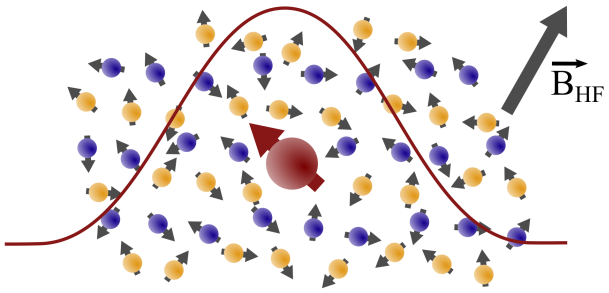

Figure 1.10: Hyperfine interaction. Illustration of the interaction between an electron spin and a large number of neighbor nuclear spins. The nuclear spin distribution can be seen as an additional magnetic field $\boldsymbol{B}_{\mathrm{HF}}$.

Because of the large spatial extension of the electron s-type orbital, this sum extends over a extremely large number of nuclear spins (typically $N = 10^6$). For this reason, it is easier to consider all these nuclear spin as an additional magnetic field (called the Overhauser field) applied to the electron:

$$\begin{aligned} H_{\mathrm{HF}} &= g\mu_B \boldsymbol{B}_{\mathrm{HF}} \cdot \boldsymbol{S} \\ \text{with} \quad \boldsymbol{B}_{\mathrm{HF}} &= \frac{1}{g\mu_B} \sum_k A_k \boldsymbol{I_k} \end{aligned} \tag{1.28}$$

In the paramagnetic case, with every nuclear spin aligned, the apparent magnetic field would reach 5 T.[Pag77; Tay07] As the external magnetic field is never large enough to polarize these nuclear spins (for $B_z = 1\,\mathrm{T}$ the nuclear Zeeman splitting is three orders of magnitude smaller than the thermal energy), we instead can consider that the nuclear bath is in a high temperature regime and each nuclear spin has a random orientation. This leads to an isotropic 3D Gaussian distribution of $\boldsymbol{B}_{\mathrm{HF}}$, centered around zero and of standard deviation:

$$\sigma_{\mathrm{HF}} \sim \frac{5\,\mathrm{T}}{\sqrt{N}} = 5\,\mathrm{mT} \tag{1.29}$$

The fluctuations of $\boldsymbol{B}_{\mathrm{HF}}$ have a timescale of $\sim 1\,\mathrm{s}$ on the axis parallel to the external magnetic field, and are due to dipole-dipole interaction between the electron and the nuclei.[Rei08] In the transverse plane they are significantly faster ($\sim 10\,\mu\mathrm{s}$), as they are not protected by the Zeeman energy mismatch between electron and nuclei, and are mainly driven by the Knight shift (the effect of the electron spin on each nuclei).[Bar09; Tay07]

Both of these timescales being several orders of magnitude larger than any qubit operation time ($\sim 100\,\mathrm{ns}$), we can consider the Overhauser field $\boldsymbol{B}_{\mathrm{HF}}$ constant during a single experimental realization. However, as explained previously, its slow fluctuations induce dephasing when the operation is repeated. To illustrate this effect, we consider the case of a qubit initially in its ground state $|0\rangle$ and submitted to rotations induced by an external field $\boldsymbol{B}_0 = B_0 \boldsymbol{u}_x$ so that the ground state probability evolves as:

$$P_{|0\rangle}(t) = \cos^2\left(\frac{\omega_0 t}{2}\right) \tag{1.30}$$

where the angular frequency $\omega_0 = \frac{g\mu_B}{\hbar} B_0$ is proportional to the magnetic field felt by the qubit. The x component of the Overhauser field B_{HF} slightly increases or decreases this precession frequency. Therefore, the effective magnetic field driving the rotation follows a normal distribution of mean value B_0 and standard deviation σ_{HF}:

$$\mathcal{N}(B) = \frac{1}{\sqrt{2\pi\sigma_{\mathrm{HF}}^2}} \exp\left(-\frac{(B-B_0)^2}{2\sigma_{\mathrm{HF}}^2}\right) \tag{1.31}$$

Thus, the ground state probability is the average over the different angular frequencies:

$$\begin{aligned} P_{|0\rangle} &= \int_{-\infty}^{+\infty} \mathcal{N}(B) \cos^2\left(\frac{g\mu_{\mathrm{B}} B}{2\hbar} t\right) dB \\ \Leftrightarrow P_{|0\rangle}(t) &= \frac{1}{2} + \frac{1}{2}\cos\left(\omega_0 t\right) e^{-\left(\frac{t}{T_2^*}\right)^2} \\ \text{with} \quad T_2^* &= \frac{\hbar\sqrt{2}}{g\mu_B \sigma_{\mathrm{HF}}} \propto \sqrt{N} \end{aligned} \tag{1.32}$$

Therefore, as presented in Fig. 1.11., the Gaussian nature of the Overhauser magnetic field leads to a Gaussian damping, on a timescale T_2^* proportional to the square root of the nuclei number $\sqrt{N}$.

The components of the Overhauser field orthogonal the external magnetic field slightly tilt the precession axis, which for a large external field has usually a rather weak effect. However, this transverse Overhauser field can induce a spin-flip, and for example couple the $|T_+\rangle$ state to the $|S\rangle$ state.

In GaAs, the hyperfine interaction is the main responsible for the rather poor coherence times ($T_2^* \approx 15\,\mathrm{ns}$), and its effects have been extensively studied.[Bra05; Dut05] Several techniques exists to compensate for it, the most well-known being Hann echo and Carr-Purcell-Meiboom-Gill (CPMG) pulses, which consists in applying π pulses to reverse the random part of the evolution.[Blu11] In addition, a pumping sequence can be used on

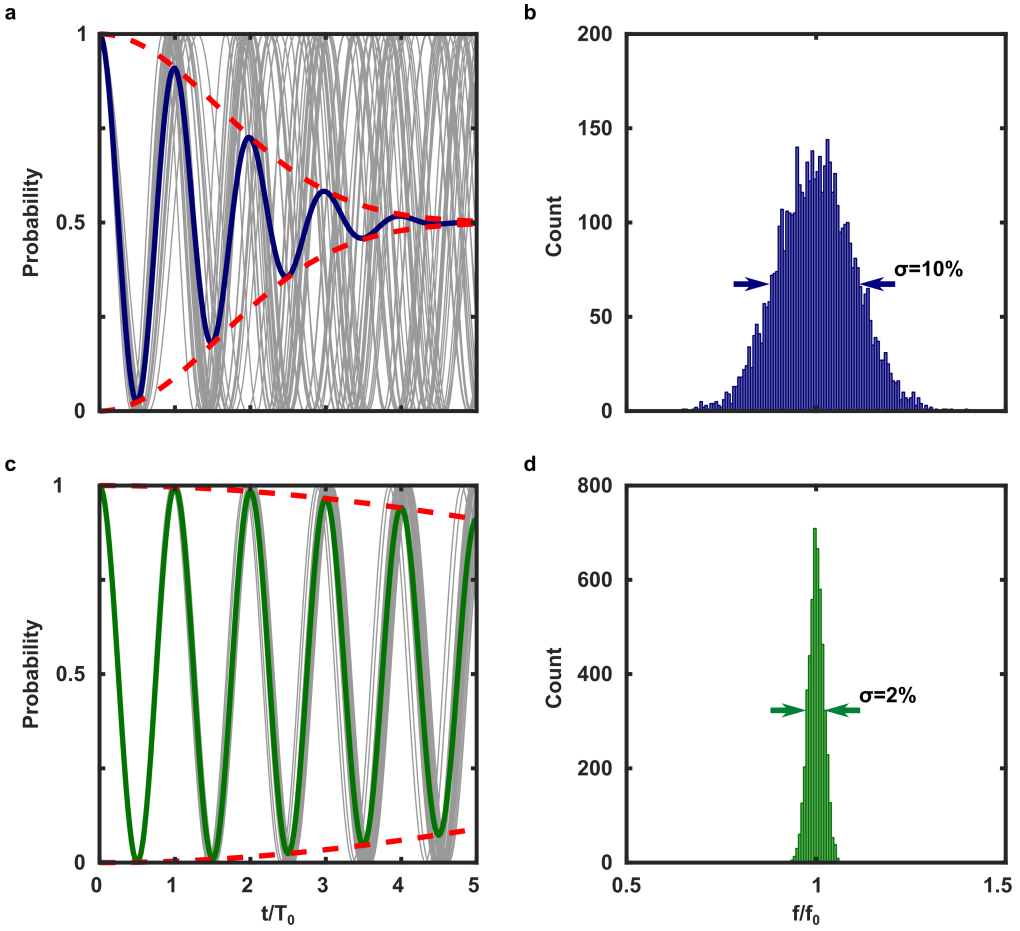

Figure 1.11: Dephasing. a.c. Single-shot spin evolution (gray) and average spin probability (blue/green line) for a Gaussian noise of width $\sigma/f_0 = 10\,\%$ (**a.**) and $\sigma/f_0 = 2\,\%$ (**c.**). **b.d.** Histogram of the frequency distribution. The width of the frequency noise is inversely proportional to the characteristic time of the Gaussian envelope in **a.** and **c.**, indicated by the red dashed curve.

the electron spin to polarize the nuclear spin bath, a method called dynamical nuclear polarization (DNP).[Blu10]

1.4 Spin manipulation

Now that the basic physical phenomena involved in spin evolution have been introduced, we focus on the methods used for single- and two-spin operations. We first study the spin-orbit interaction, and its ability to drive single-spin rotations for an electron in motion. In addition, we present other techniques used in semiconductor quantum dots to drive single-spin rotations. Then, we introduce a two-spin exchange gate, realized in a double quantum dot by tuning the interdot tunnel coupling and energy detuning.

1.4.1 Single-spin manipulation

Spin orbit interaction

The spin-orbit interaction is a generic term employed for phenomena coupling the electron momentum to its spin degree of freedom. These mechanisms are of paramount importance for the development of spin qubit devices, as they offer a knob to manipulate electrically the spin state. However, they also provide decoherence sources, as they increase the spin coupling to its environment. In GaAs, two intrinsic mechanisms are responsible for the spin-orbit coupling, both relativistic effects of the electron motion in an electrical potential. If we consider an electron of momentum $\boldsymbol{p}$ in an electrical field $\boldsymbol{E}$, from the perspective of this electron an effective magnetic field $\boldsymbol{B}_{\mathrm{SO}} = -\frac{1}{mc^2}\boldsymbol{p} \times \boldsymbol{E}$ is perceived, affecting its spin.

The Dresselhaus spin-orbit interaction[Dre55; Par55] finds its origin in the bulk inversion asymmetry of the zinc-blende structure of GaAs. This non-centrosymmetric structure leads to an asymmetric electrical potential depending on the electron momentum. In a 2D nanostructure, with a finite thickness t in the z direction, the Dresselhaus Hamiltonian is a sum of a linear and a cubic term:

$$\begin{aligned} \mathrm{H}_{\mathrm{D}}^{(1)} &= \frac{\beta}{\hbar}\left(p_x\sigma_x - p_y\sigma_y\right) \\ \mathrm{H}_{\mathrm{D}}^{(3)} &= -\frac{\beta}{\hbar^3}\left(\frac{t}{\pi}\right)^2 p_x p_y \left(p_y\sigma_x - p_x\sigma_y\right) \end{aligned} \tag{1.33}$$

with β is the Dresselhaus coupling constant. Generally only the first term, linear in momentum, is taken into account.

The Rashba interaction[Byc84; Ras60] arises from the triangular electrostatic potential confinement along the growth axis at the 2DEG depth. This potential leads to an electrical field along z, felt by an electron propagating in the 2DEG as an in-plane magnetic field and the equivalent Hamiltonian:

$$\mathrm{H}_{\mathrm{R}} = \frac{\alpha}{\hbar}\left(\boldsymbol{p} \times \boldsymbol{u_z}\right) \cdot \boldsymbol{\sigma} = \frac{\alpha}{\hbar}\left(-p_y\sigma_x + p_x\sigma_y\right) \tag{1.34}$$

with α the Rashba coupling constant, dependant on the confinement along the growth axis. In our GaAs heterostructures, the relative magnitudes of these two contributions depend on the z confinement, with some recent work indicating that both the Dresselhaus and Rashba effect have to be taken into account.[Sca14]

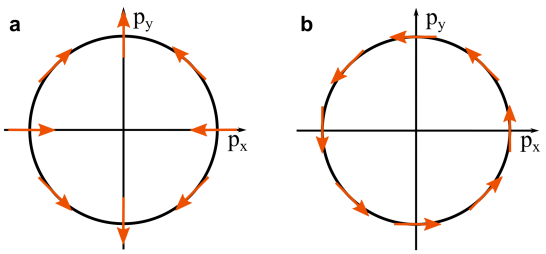

Figure 1.12: Spin-orbit interaction. Orientation and magnitude of the equivalent magnetic field created by a **a.** Dresselhaus and **b.** Rashba type of spin-orbit interaction.

Figure 1.12. presents the equivalent magnetic field orientation associated with both Dresselhaus and Rashba types of spin-orbit coupling. For some direction of propagation, these two phenomena can add up or partly compensate each other. In the case of a propagation along the [110] or $[\bar{1}10]$ axis ($|p_x| = |p_y| = p$), the spin-orbit interaction is felt by the electron as a magnetic field perpendicular to its momentum:

$$\begin{aligned} \boldsymbol{B}_{\mathrm{SO}}^{[110]} &= -\frac{p(\beta-\alpha)}{g\mu_{\mathrm{B}}\hbar}\boldsymbol{u}_{[\bar{1}10]} \\ \boldsymbol{B}_{\mathrm{SO}}^{[\bar{1}10]} &= -\frac{p(\beta+\alpha)}{g\mu_{\mathrm{B}}\hbar}\boldsymbol{u}_{[110]} \end{aligned} \tag{1.35}$$

Under this in-plane magnetic field, the electron spin rotates at an angular rate $\omega_{\mathrm{SO}} = g\mu_{\mathrm{B}}B_{\mathrm{SO}}/\hbar$. Since this rate is proportional to the electron speed $v = p/m_0$, it is often convenient to define the spin-orbit length, for which a propagating electron experiences a π pulse:

$$l_{\mathrm{SO}}^{[110]} = \frac{v\pi}{\omega_{\mathrm{SO}}} = \frac{\pi\hbar^2}{m_0|\beta-\alpha|} \tag{1.36}$$

As expected, this characteristic length is inversely proportional to the magnitude of the spin-orbit interaction, which in turn depends on the direction of motion. In two-dimensional GaAs heterostructures, it is typically of the order of a few micrometers.[San11]

In consequence, by engineering specific electron trajectories one could potentially drive any single-spin rotation.[San13] This opens the ways towards a qubit manipulation via the spin motion, of which this thesis is an example. However, the need for a micrometer shuttling limits the scalability and inter-connectivity of a device whose single-qubit gates are exclusively based on this mechanism. For this reason, complementary techniques designed to perform single-spin rotation in a static quantum dot have been developed, of which we will now present a brief review.

Electron spin resonance

By analogy with the atomic physics and the nuclear magnetic resonance (NMR) techniques, one could imagine to drive single-spin rotations by applying an oscillating magnetic field B_x orthogonal to the external magnetic field B_z defining the quantization axis of our spin qubits.[Poo96] Indeed, by tuning the frequency of B_x in resonance with the Larmor frequency $\omega_z = g\mu_{\mathrm{B}}B_z/\hbar$ of the electron spin, we can drive single-spin rotations around the x or y axis, providing a full control over the qubit. The usual technique consists in defining a micrometer metallic strip close to the sample through which a large oscillating current is passed, generating the in-plane magnetic field. This technique has been demonstrated both for GaAs[Kop06] and Si[Pla13] quantum dots, but the coupling strength remain rather weak, dramatically limiting the operation rate. In addition, these large metallic feedlines are not easily scalable and require a large power to be brought to the sample.

Electric dipole spin resonance

Another technique commonly used to create an oscillating in-plane magnetic field consists in applying a high-frequency modulation to the electrostatic potential confining the electrons,

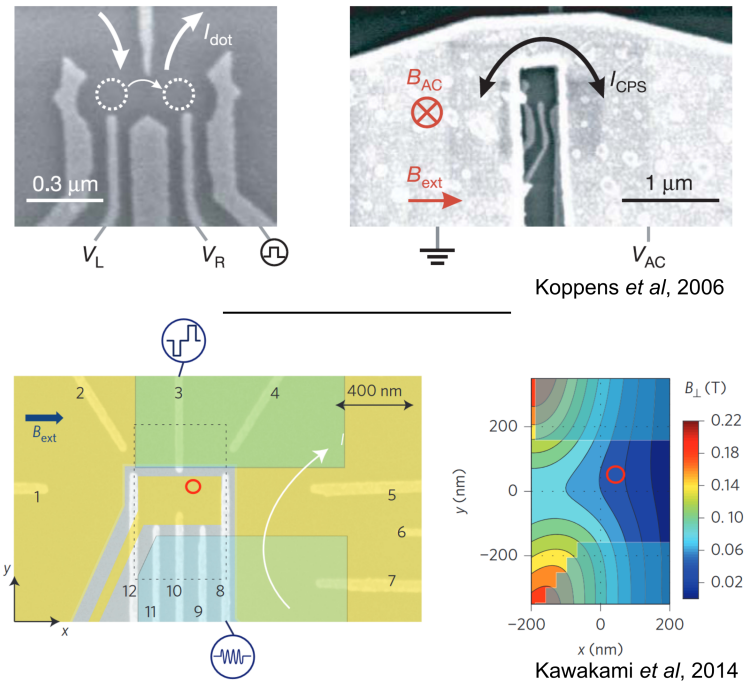

Figure 1.13: Electron spin resonance. top. Stripline used for ESR resonance, deposited on top of a GaAs/AlGaAs double quantum dot. From [Kop06]. **bottom.** Scheme of a Si/SiGe double quantum dot and magnetic field gradient created by a Co micro-magnet located at the surface of the sample. From [Kaw14].

effectively moving the spins back and forth over several tenth of nanometers. Because of the spin-orbit coupling, this displacement is indeed able to drive a spin rotation at a rate depending on the input power.[Now07] However, as the intrinsic spin-orbit coupling is rather weak for electrons in GaAs (and null for electrons in Si) the achieved Rabi frequencies are quite weak, typically reaching at most a few MHz.

To overcome this limitation, the state of the art technique consists in artificially increasing the spin-orbit coupling by creating a magnetic field gradient along the direction of motion of the electron. In practice, a micro-magnet is deposed at the surface of the sample, resulting in a gradient up to $\sim 1\,\mathrm{mT/nm}$.[Kaw14; Tak16] By applying a high-frequency electrical modulation on a gate defining the quantum dot, the spin can be submitted to an oscillating magnetic field able to drive single-spin rotations at frequencies up to 30 MHZ.[Yon18]

1.4.2 Two-spin exchange

In addition to the single-spin operations previously discussed, the realization of quantum logic circuits requires the development of two-qubit gates. Indeed, these gates are required to share entanglement across the nanostructure, and create the many-qubit superposition of states required by quantum algorithms. In laterally defined quantum dots, the first two-qubit gate was realized by Petta *et al*[Pet05] in a double quantum dot, taking advantage of the exchange coupling between electrons in adjacent quantum dots. This experiment

relies on a nanosecond control of the energy detuning between the two dots, allowing non-adiabatic changes of spin basis between the (1,1) and (2,0) configurations in the GHz interdot coupling regime.

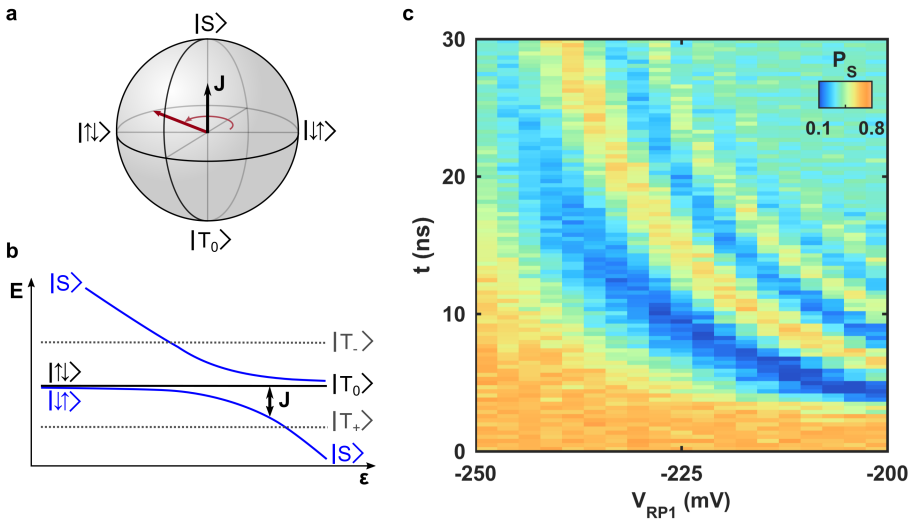

Figure 1.14: Exchange oscillations. c. Two-spin coherent oscillations driven by the exchange interaction between adjacent electrons. The oscillation frequency ($f_{\mathrm{Rabi}} \propto J$) increases with the detuning ε, as sketched in **b**. The spin trajectory in the Bloch sphere is indicated in **a**.

In the (1,1) charge configuration, the dominant energy scale for the two antiparallel states $|\uparrow\downarrow\rangle$ and $|\downarrow\uparrow\rangle$ is the Overhauser magnetic field induced by the surrounding nuclear spins. As mentioned before, it has a Gaussian distribution of standard deviation $\sigma_{\mathrm{HF}} \sim 5\,\mathrm{mT}$ and mean value 0 mT, and fluctuates with a timescale of the order of a few seconds (on the z axis). In a double quantum dot, a difference in magnetic field of the order of a few mT is thus to expect between the two dots for each direction x, y and z. The later lifts the degeneracy between the $|\uparrow\downarrow\rangle$ and $|\downarrow\uparrow\rangle$ state by $|g\mu_{\mathrm{B}}\Delta B_z| \approx 10\,\mathrm{MHz}$. For the following explanation, we consider that $\Delta B_z < 0$ and $|\downarrow\uparrow\rangle$ is the ground spin state in the (1,1) configuration.

As sketched in Fig. 1.14., if a detuning pulse is applied to bring the system towards the (2,0) configuration, where the $|\downarrow\uparrow\rangle$ and $|\uparrow\downarrow\rangle$ states are not eigenstates anymore, the exchange energy J drives a precession of the spin state. For a specific exchange pulse duration ($\frac{J\tau}{\hbar} = \pi$) the spins of two adjacent electrons are exchanged, an operation called a SWAP gate. If a pulse half as long is applied, a $\sqrt{\mathrm{SWAP}}$ gate, building bloch of many quantum algorithms, is realized. As the exchange energy depends on the detuning ε, the frequency of the exchange oscillations can be increased by increasing the detuning pulse amplitude. However, as demonstrated by Bertrand *et al*,[Ber15b] the detuning noise impact is proportional to the Rabi frequency, coercing the decoherence time to an upper bound inversely proportional to the frequency of the oscillations ($T_2^{\mathrm{Rabi}} \propto 1/f^{\mathrm{Rabi}}$).

In section 4.3.2, we observe experimentally such exchange oscillations, adding an adiabatic

conversion from the $|S\rangle$-$|T_0\rangle$ to the $|\downarrow\uparrow\rangle$-$|\uparrow\downarrow\rangle$ basis for the spin initialization and readout.

1.5 Surface acoustic wave as an electron conveyor belt

Surface acoustic waves (SAW) are a type of mechanical wave introduced by Lord Rayleigh to explain seismic data observed after earthquakes.[Ray85] As their name suggests, these waves propagate mostly at the surface of their medium, disturbing matter only on a depth of the order of their wavelength. They are widely used as bandpass filters and delay lines in most of nowadays electronic devices, and has thus been extensively studied for both fundamental and industrial applications.

The surface acoustic waves we use in this work propagate at a speed of $v_{\mathrm{SAW}}^{\mathrm{bulk}} = 2.88\,\mu\mathrm{m/ns}$ in bulk GaAs. The presence of thin metallic gates on top of the substrate and the AlGaAs layer slightly lowers this speed, typically to $v_{\mathrm{SAW}} = 2.79\,\mu\mathrm{m/ns}$. This intermediate speed, 5 orders of magnitude slower than light, leads to propagation times of several nanoseconds across our few-micrometers structures, which is within the range of our fast electronics. However, when used to shuttle electrons it still provides a transfer duration shorter than typical decoherence processes in GaAs ($\sim 10\,\mathrm{ns}$). In addition, the relatively large speed creates a significant spin-orbit interaction, that we will exploit in the last chapter of this thesis.

1.5.1 SAW generation

The SAW generation and probing relies on the piezoelectric properties of the GaAs substrate. This coupling between electrical potential and mechanical deformation gives us the ability to convert a microwave voltage burst into a propagating acoustic wave, or contrarily to probe the SAW amplitude by measuring a voltage. For this purpose, we lithographically define interdigital transducers (IDTs) on top top of the sample, that we connect to a high-frequency coaxial cable.

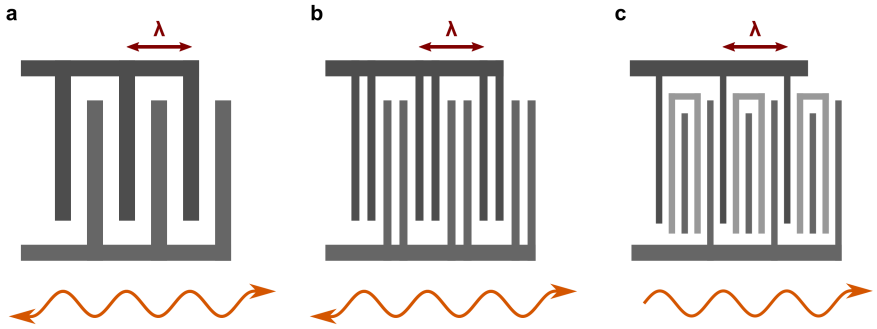

Figure 1.15: Interdigital transducer. a. Single finger IDT, composed of two metallic fingers per period, alternatively connected to two electrodes. The resonant frequency is fixed by the period of these fingers. **b.** Double finger IDT, where each finger is split in two thinner gates. This geometry increases the conversion factor from electrical to mechanical wave. **c.** Unidirectional IDT, with five fingers per period. This connection scheme creates a SAW propagating only towards the right of the IDT.

An IDT is made of many thin metallic strips, alternatively connected to an oscillating voltage source or grounded.[Dat90; Wei57] The IDT resonant frequency is imposed by its

geometry and the SAW velocity, assumed constant in the few-gigahertz regime. Figure 1.15. presents three types of IDTs, all with the same period $\lambda = 1\,\mu m$, and consequently the same resonant frequency $f_0 = v_{SAW}/\lambda = 2.79\,GHz$. The most simple IDT shape, called *single finger* IDT, has two metallic strips of $\lambda/2$ pitch per period. The *double finger* IDT has four fingers per period, and presents the advantage of limiting internal reflections and increasing the power conversion towards the generated SAW. However, half of this power is lost as two SAW bursts, propagating in opposite directions, are generated. The *unidirectional* IDT uses floating gates to maximize the directionality of the SAW generation.[Eks17] The drawback of using these advanced IDT geometries lies in their nanofabrication, are the metallic gates get thinner for the same resonant frequency (same period).

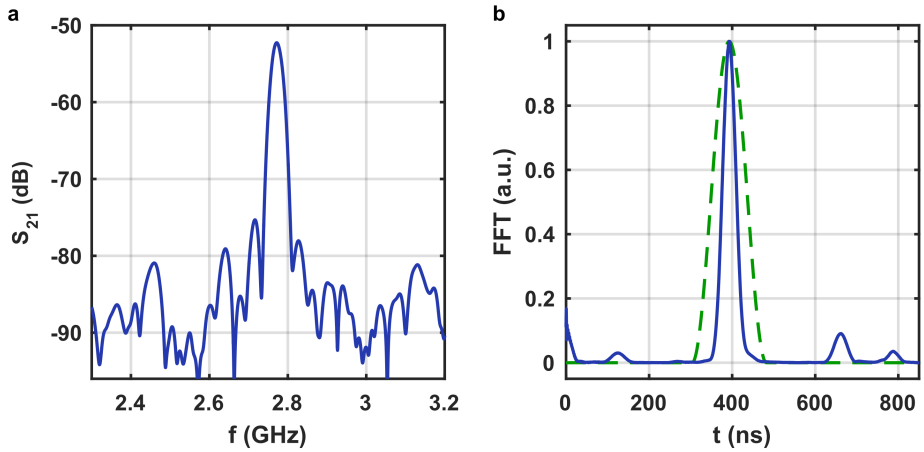

Figure 1.16: IDT characterization. a. Electrical transmission S_{21} as a function of the frequency through two IDT separated by 1050 µm, composed of $N = 70$ double finger pairs of period $\lambda = 1\,\mu m$. At the resonant frequency $f_0 = 2.77\,GHz$, the transmission reaches $-52.3\,dB$. **b.** Fast Fourier transform of the data presented in **a.**. From this time-domain analysis we can clearly identify the propagation time of SAW, $\tau = 393\,ns$. Capacitive coupling, travelling as the speed of light, is responsible of the feature near $t \approx 0\,ns$, and the other peaks are reflections at the surface of the material. The dashed green curve represents the Hann filter applied in **a.** to remove these contributions.

In this work, we used a double finger transducer of period $\lambda = 1\,\mu m$. The metallic fingers are each 125 nm wide, 15 nm thick and 70 µm long. They are defined by electron-beam lithography, during the same fabrication step as the central nanostructure, and are made of a Ti/Au stack (4/11 nm). Figure 1.16. presents a room-temperature measurement of the transmission through two identical IDT separated by 1050 µm. The resonant frequency of the IDTs is 2.79 GHz, and their bandwidth is inversely proportional to the number of fingers. In our case ($N = 70$ periods, 280 fingers), the resonance is 50 MHz wide.

Due to the poor piezoelectric constant of GaAs, the electro-mechanical conversion efficiency is extremely low. This can be seen as a large impedance mismatch between the high impedance IDT and the 50 Ω coaxial cable. As a consequence, most of the incoming electrical power is reflected back to the cable instead of being converted into mechanical power. From the maximum value of Fig. 1.16.a., we extract a conversion efficiency of about

−26 dB for one single IDT. Thus, we have to apply a large microwave power (5-15 dBm) on the sample to generate a SAW of sufficient amplitude to shuttle electrons. In addition, we show Fig. 1.16.b. the fast Fourier transform of the S_{21} signal. This time domain analysis presents the signature of capacitive coupling between the IDT at $t \approx 0$ ns. This airborne signal propagating at the spin of light is easily separable from waves propagating at the speed of sound in GaAs. We can also identify additional peaks, corresponding to reflections on the other structures present on the test sample. The data presented Fig. 1.16.a. are filtered with a Hann window in time domain, represented by the dashed green line in b., to isolate the main SAW signal and remove the capacitive coupling baseline.

1.5.2 SAW-assisted shuttling

The propagating electric field associated with a surface acoustic wave has in the past largely been studied and exploited, particularly in GaAs structures. In 1996, Shilton *et al* demonstrated[Shi96a; Shi96b] that SAW-induced current could flow through a pinched-off quantum point contact, and that this current was quantized in units of ef, with f the SAW frequency. This behavior corresponds to a given number of electrons being loaded into each minima of the SAW and transported through the QPC with the help of this potential modulation. Contrarily to current induced by a voltage bias, here the current direction remains constant even when the bias is reversed, as electrons always propagate in the SAW direction.

From this first SAW-induced current demonstration followed many proposals for possible applications, such as a current standard definition based on quantum mechanical properties,[Zim03] or single-photon sources using electron-hole recombination in a P-doped region.[Fod00] The spin qubit community realized the potential of such a quantum link between existing quantum dots, able to shuttle electrons and their spin across micrometers to interconnect quantum processing units. Pioneer work by Hermelin *et al*[Her11] and McNeil *et al*[McN11] demonstrated a controlled transfer of single electrons between two static dots using a SAW. Their technique, that we employ in our work (see 3.2.2), relies on a nanosecond control of the electron injection into the moving quantum dot train created by the SAW potential modulation.

Mathematically, the SAW profile u_{SAW} corresponds to the convolution of the applied microwave burst V_{MW} with the IDT geometry, approximated by a sum of Dirac delta functions for each finger with its polarity $Pi = \pm 1$:

$$\begin{aligned} u_{\mathrm{SAW}}(x,t) &= V_{\mathrm{MW}}(t) * D(t) \\ \text{with } D(t) &= \sum_i P_i \delta\left(v_{\mathrm{SAW}} t - x_i\right) \end{aligned} \tag{1.37}$$

Figure 1.17. presents the SAW amplitude as a function of time measured 2 mm away from a double-finger IDT of period $\lambda = 1\,\mu$m. A microwave burst of duration $t_{\mathrm{MW}} = 10$ ns tuned at the resonant frequency of the IDT $f_0 = v_{\mathrm{SAW}}/\lambda = 2.79$ GHz is applied to one of the transducer electrodes. This electrical pulse is converted to a SAW burst and propagates at the speed of sound, reaching the measurement position in 717 ns. Because of the IDT length ($N\lambda = 7\,\mu$m), a $t_{\mathrm{IDT}} = 2.1$ ns rising time is observed in the SAW burst. This

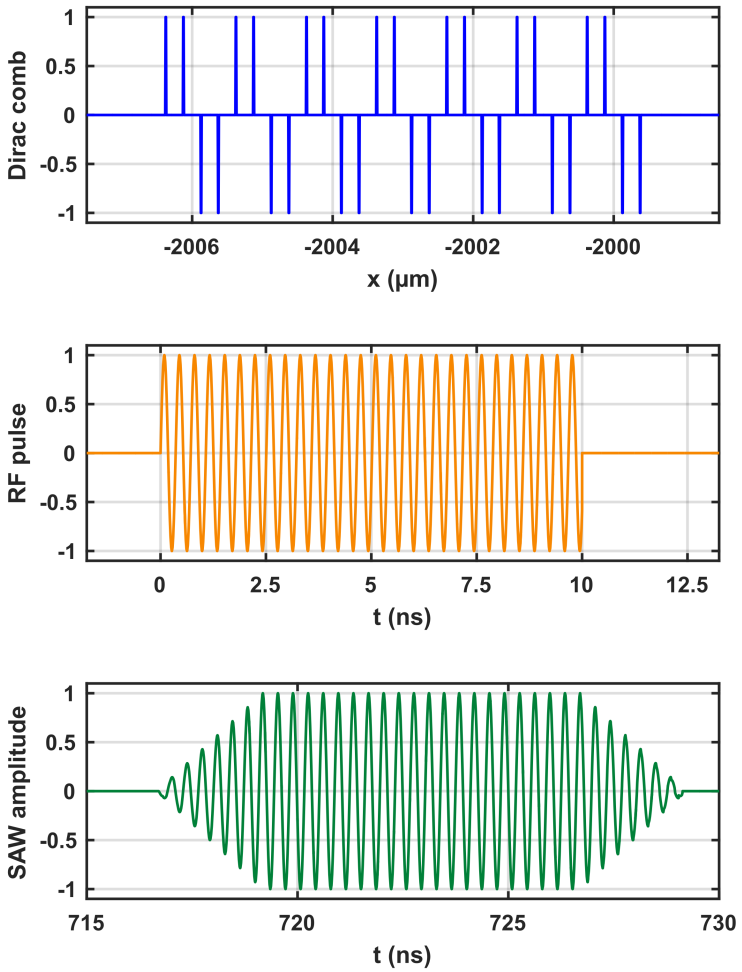

Figure 1.17: SAW burst profile. a. Dirac comb, modeling an double-finger IDT identical to the one used in this work, to the exception of the number of periods (7 instead of 70). **b.** Applied microwave burst, of frequency $f_0 = v_{\mathrm{SAW}}/\lambda = 2.79\,\mathrm{GHz}$ and duration $t_{\mathrm{MW}} = 10\,\mathrm{ns}$. **c.** SAW amplitude 2 mm away from the IDT. The $t_{\mathrm{IDT}} = 2.1\,\mathrm{ns}$ rising (and falling) time of the SAW burst corresponds to the SAW propagation time under the IDT. The maximum amplitude is maintained for $t_{\mathrm{MW}} - t_{\mathrm{IDT}} = 7.5\,\mathrm{ns}$.

time corresponds to the SAW propagation time under the IDT, after which all fingers constructively create the SAW. Thus, the maximum SAW amplitude plateau has a duration of $t_{\mathrm{MW}} - t_{\mathrm{IDT}} = 7.5\,\mathrm{ns}$. For an easier representation of the SAW profile, the number of IDT fingers and the microwave burst duration were here both reduced by a factor 10. Indeed, in the work presented in this thesis we use a $N = 70$ period IDT and a $t_{\mathrm{MW}} = 100\,\mathrm{ns}$ microwave burst. Experimentally, we therefore expect the SAW amplitude similar to the one Fig. 1.17.c., but with a rising/falling time of 25 ns and a plateau of 75 ns. The burst arrival time and its frequency remain unchanged.

In these conditions, the SAW burst is composed of about 350 minima, in which electrons can be shuttled. This uncertainty is extremely decremental when two electrons need to be transported together to avoid decoherence. To circumvent this issue, we trigger the injection of both electrons in specific SAW minima with the help a sub-nanosecond voltage pulse. This *delay-controlled* sending procedure is described in section 3.2.2, and presents a fidelity higher than 80 %, mainly limited by the rising time of the voltage pulse.

1.6 Conclusion

In this chapter, we presented the concepts and techniques used to isolated a few electrons in quantum dots and control their spin information. Using a partially depleted two-dimensional electron gas located at the interface of a GaAs/AlGaAs heterostructure, we can define quantum dots and probe their charge occupancy with local electrometers. In addition, we exploit several spin-to-charge conversion mechanisms to read-out the spin degree of freedom of our system. Single-spin and two-spins operations have been introduced, focusing on the impact of the spin-orbit interaction for electrons in motion, and the observation of two-qubit exchange oscillations. The environmental effects have been discussed, dominated in GaAs by the fluctuating Overhauser magnetic field produced by the nuclear bath surrounding our qubits. Finally, we studied the generation of surface acoustic waves and its use as a tool to shuttle electrons across a nanostructure.

CHAPTER 2

Description of the experimental setup

In this chapter, we describe the experimental setup, starting from the sample fabrication and electrostatic potential simulations. We detail the instruments used to control and measure this sample, as well as the measurement software developed to control them. We present the cryogenic equipment required to achieve sufficiently low temperatures, and discuss the acceptable noise figures and cooling power management. Finally, we introduce the data analysis tools, allowing us to perform the complex data treatment required by the study presented in this thesis.

2.1 Energy scales - requirements

As discussed in the first chapter, the dominant energy scale in our system is the charging energy, corresponding to the electrostatic energy associated with the addition of an extra charged particle in the quantum dot. Its magnitude, dependant on the quantum dot size, is of the order of $E_C \approx 1\,\text{meV}$. The exchange energy between singlet and triplet spin states is expected to be of the order of $J_0 \approx 300\,\mu\text{eV}$ for a singlet quantum dot. Under a 100 mT external magnetic field, the $|T_+\rangle$ and $|T_+\rangle$ spin states are separated from the $|T_0\rangle$ spin state by $E_Z = 2.5\,\mu\text{eV}$.

In units of temperature, frequency and magnetic field, the exchange energy in a single quantum dot J_0 is equivalent to:

$$300\,\mu\text{eV} \approx 3.5\,\text{K} \approx 72\,\text{GHz} \approx 13\,\text{T} \tag{2.1}$$

This correspondences set the requirements in terms of noise, temperature and dynamics of the system, which we will keep in mind as we introduce the different instruments we used. Nevertheless, it is interesting to note that some of the charge and spin manipulation are performed out of equilibrium, which means that the previously introduced requirements need to be adapted to the system dynamics.

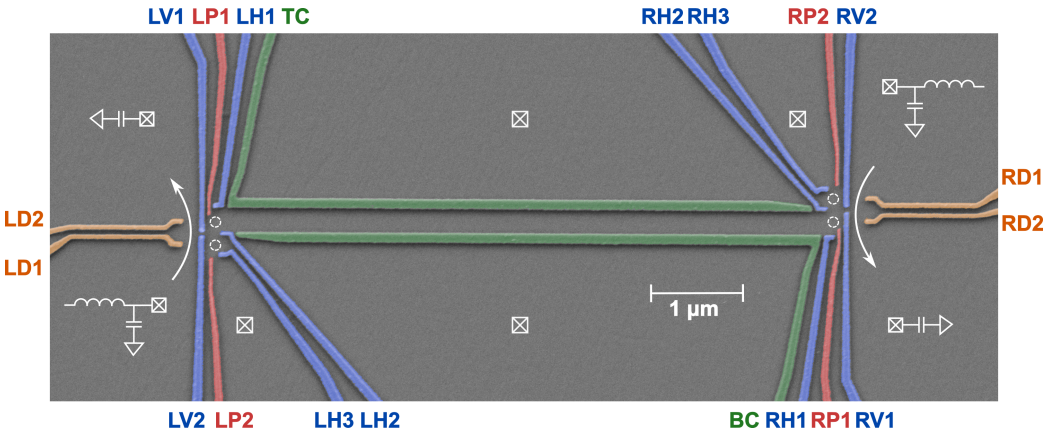

Figure 2.1: Sample picture. False-color SEM micrograph of a sample identical to the one presented in this thesis. On each side of the 6 µm long channel (green) are two double quantum dots whose estimated positions are indicated by dotted circles. Each side is probed by a local electrometer (orange), connected to a reflectometry setup. Four fast gates (red) are connected to an AWG and used for fast spin or charge manipulation.

2.2 Sample fabrication

2.2.1 Process flow

Realizing the type of nanostructure measured in this thesis requires advanced nano-fabrication techniques, able to define nm-wide metallic gates in a cleanroom environment. We start from GaAs/$Al_{0.33}Ga_{0.67}As$ wafers realized by A.D. Wieck from the Ruhr-University in Bochum, Germany. Most of the nano-fabrication is done in the Institut Néel's cleanroom, and a few steps are done at the *Plateforme Technologique Amont* at the CEA Grenoble.

The first fabrication step consists in etching away $100 - 120$ nm of substrate everywhere the 2DEG is not needed (forming electrically isolated 2DEG islands called "mesa"). We create ohmic contacts to the mesa depositing a 200 nm stack of Au/Ge/Ni/Au followed by an annealing step at 400 °C for one minute. The deposited Germanium and Nickel diffuse into the semiconductor and form an alloy, which greatly reduces the contact resistance ($R \approx 400\,\Omega$), allowing us to pass current through the 2DEG.

Next, we define alignment marks by laser lithography and metal deposition. These marks are of paramount importance, to ensure a good alignment between the different fabrication steps down to a sub micrometer precision. We realize two successive lithographies, defining firstly the fine structure and the IDTs and secondly the larger lines connecting them to the bonding pads. The first layer is the most critical step, as the minimum gate width is 20 nm, and is done using electron beam lithography. A focused high-energy electron beam irradiates a photo-sensitive resist (PMMA 2 %), following the wanted gate pattern. The irradiated resist is removed using a developing chemical (MIBK + IPA), and a 15 nm Ti/Au metallic stack is deposited on top of the accessible substrate. Lift-off is then performed, where the rest of the resist is removed by placing the sample in Acetone. Because of the density of irradiated areas (particularly for the IDT), some features may be over-exposed due to proximity effects (e.g. unintentional exposure via electron back-scattering), which

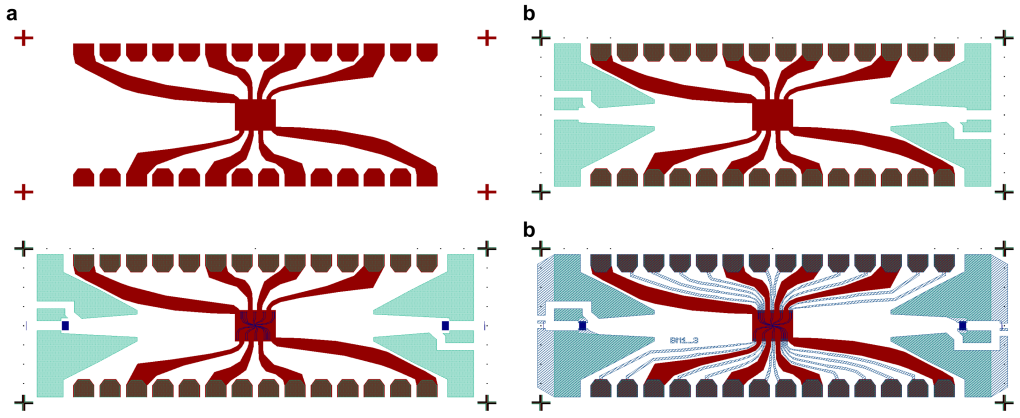

Figure 2.2: Fabrication scheme. a. Mesa etching. **b.** Ohmic contacts and alignment marks. **c.** Electron beam lithography of the fine structure and the IDTs. **d.** Laser lithography of the larger contact gates.

needs to be compensated by adjusting the e-beam dose and modifying the design given to the machine.

The second lithography, exposing the larger contact gates, is based on the same principle, except that the resist and developer are different and the irradiation is done by a infra-red laser with a larger resolution (1 µm). After this fabrication is over, we observe the sample under SEM to check the metallic gates continuity and shape. We then cut the wafer using a diamond scriber, and each sample is placed in an antistatic box. A sample is glued to a PCB, and its pads are connected using gold wire bonding. Once out of the cleanroom, the main threat to the sample is electrical shock, which is why its pads are kept grounded until measurement.

2.2.2 Potential simulation

During the sample design, as well as its measurement, we often use numerical simulations to estimate the potential landscape and the influence of each gate voltage. They rely on a Poisson solver to compute, from the gate geometry, the induced electrical potential at the depth of the 2DEG. Figure 2.3 shows the output of a Comsol© simulation as a color-coded 2D plot. We can identify the channel, electron reservoirs and sensing quantum dot. We observe that the potential profile along the channel shows no parasitic dot behavior, which was the main decoherence mechanism identified in earlier versions of this sample.[Ber15a] Comparing the three panels in Fig. 2.3, we can understand the effect of the RH2 gate on the right double quantum dot. Applying a more positive voltage on this gate brings the two quantum dots closer, increasing their interdot coupling.

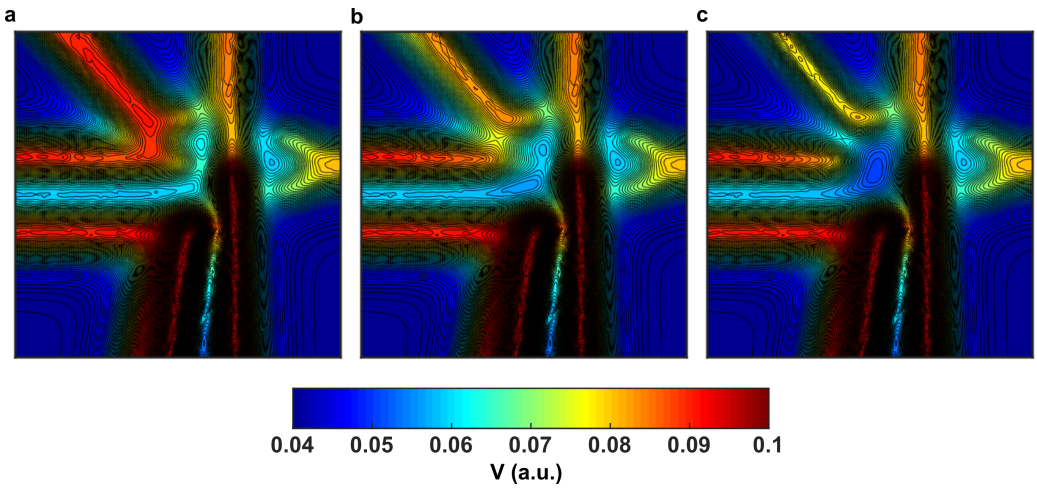

Figure 2.3: Potential simulation. Comsol© simulation of the potential induced by the metallic gates at the 2DEG depth, for different values of the interdot gate RH2 (**a.** dRH2 = -300 mV, **b.** dRH2 = 0 mV, **c.** dRH2 = +300 mV). The transition from uncoupled dots to one single large quantum dot is visible.

2.3 Cryogenics

To achieve the cryogenic temperatures required for this work, we place the sample inside a homemade dilution refrigerator of base temperature 7 mK. With the addition of the RF lines, amplifier and attenuators, the sample temperature is 65 mK. Fitting the Fermi distribution of the electron reservoirs, we estimate the electronic temperature around a few 100 mK.

A dilution refrigerator is based on the phase separation between two Helium isotopes. Below 870 mK, a mixture of ^{3}He and ^{4}He will separate into a "pure" phase, almost composed of 100 % ^{3}He, and a "dilute" phase containing 6.4 % ^{3}He and 93.6 % ^{4}He.[Pob07] An external pump (at room temperature) drives a ^{3}He flow from the pure to the dilute phase, which is an endothermic process, providing a few 100 µW of cooling power at the interface for the refrigerator used in this work.

More precisely, the dilution system is enclosed in a vacuum chamber, surrounded by a liquid Helium bath (see Fig. 2.4). ^{3}He is injected from room temperature at a pressure of a few 100 mbar, cleaned through a liquid nitrogen trap (at 77 K), and cooled down to 4.2 K by the Helium bath. It then enters the vacuum chamber, and is further cooled to 1.3 K by the 1K pot, which is simply a box filled with Helium from the bath and pumped to a pressure of 1 mbar, thereby lowering the boiling point. It then passes though several heat exchangers to finish the cooling down to the base temperature and enters the mixing chamber. This is where the interface between the pure and dilute phases is located, and where the lowest temperature is reached. As mentioned earlier, liquid ^{3}He is forced to pass through the interface to the dilute phase, and later used to cool down incoming helium through the heat exchangers. It finally reaches the still, a box filled with the dilute phase and pumped by a primary and a turbomolecular pump. Because at the still temperature ($\sim$ 750 mK) the partial pressure of ^{3}He is greater than the one of ^{4}He, almost only ^{3}He

evaporates and is re-injected, completing the cycle.

The cooling power of a dilution refrigerator is directly proportional to the ^{3}He flow $\dot{n}_3$ (in mol/s), which in turns depends on the evaporation rate in the still. To increase the latter, we connect a heater to bring the still temperature to the optimal value (before starting to evaporate ^{4}He as well), and use high-flow pumps and large pipes. However, as the achieved cooling power is rather small, a great attention must be paid to heat reaching the sample, in particular by the thermal anchoring of the electrical connections to the room-temperature electronics.

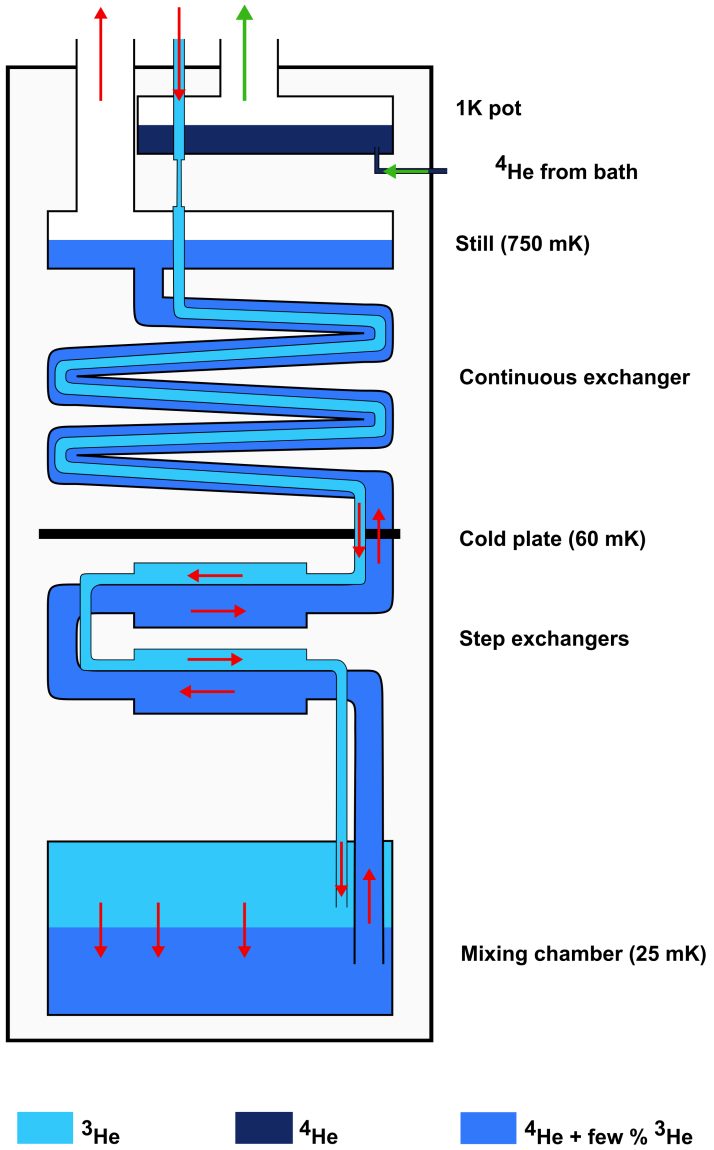

Figure 2.4: Scheme of a dilution refrigerator. A ^{3}He/^{4}He mixture is cooled down by the Helium bath, the 1K pot and the exchangers. In the mixing chamber, ^{3}He is forced to dilute into the less concentrated phase, which is an endothermic process. An external pump constantly removes ^{3}He from the dilute phase and re-injects it, driving the cooling process.

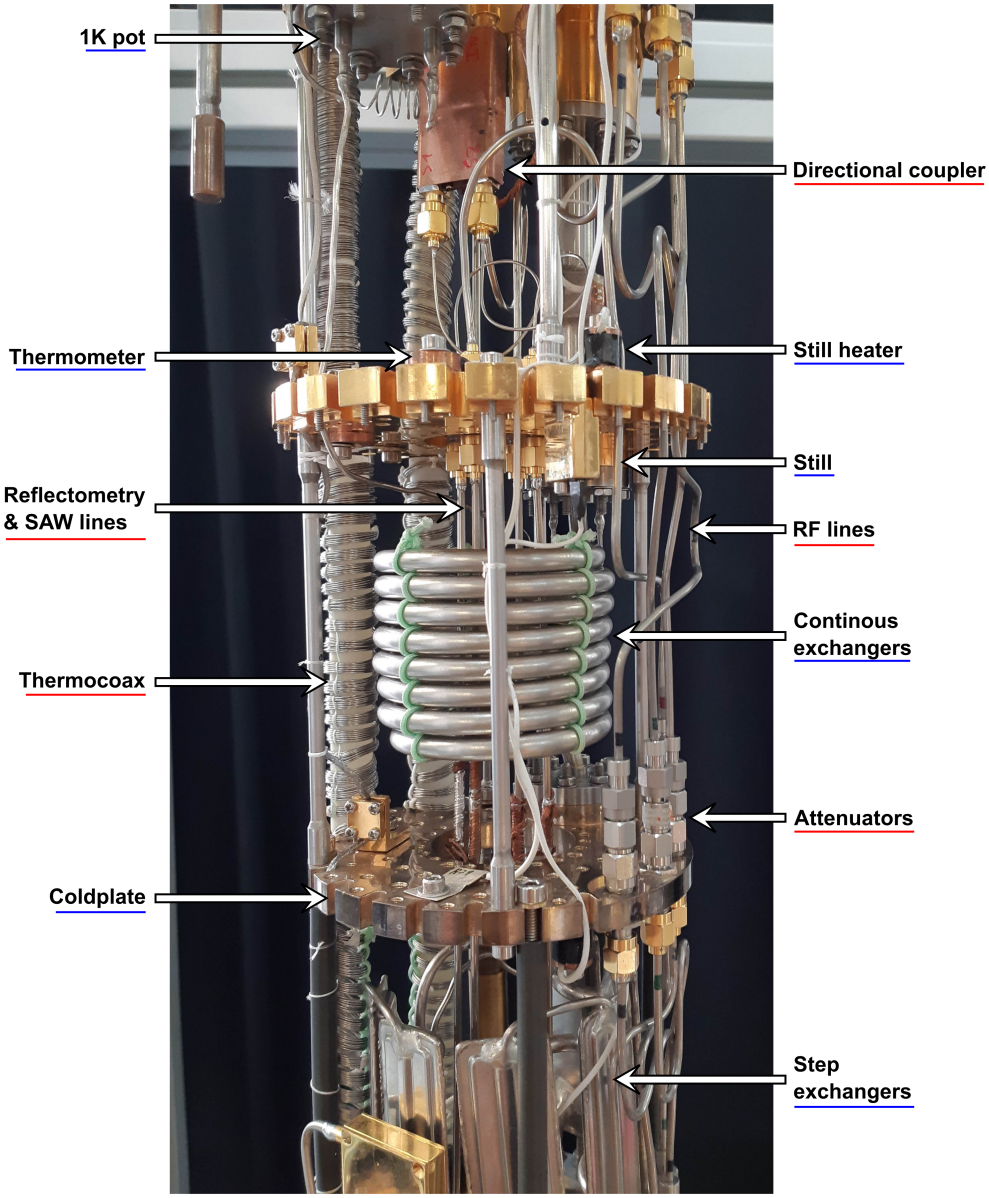

Figure 2.5: Refrigerator picture. The 1 K to 60 mK stages are indicated, with the main cryogenic components underlined in blue. The coaxial cables connected to the sample are underlined in red. The 4 outside RF lines are connected to the gates LP1, RP1, LP1 and LP2, while the RF lines passing through the center of the exchangers are either part of the reflectometry setup or connected to the IDTs.

2.4 Control electronics

To manipulate the charge and spin state held in our double quantum dots we need both a static negative potential to define the quantum dots and the possibility to apply nanosecond voltage pulses to manipulate the spin state and perform the electron transfer protocol. In order to mitigate the electrical noise reaching our sample, we can either use filtering or attenuation. The static potential is given by DC wires, with a low-pass filter behavior removing the high-frequency noise. In the case of the nanosecond voltage pulses, attenuators are placed at several stages of the refrigerator to limit the noise reaching the sample. In addition, both of these lines need thermal anchoring to regulate the heat conduction towards the sample stage. These requirements on the noise, bandwidth and thermal budget greatly constrain the design of the experimental setup. In this section, we detail the different materials and equipment used to bring the control signals to the measured device.

2.4.1 DAC

The main requirements on the DC polarization of the sample are noise and safety. Indeed, our GaAs nanostructures are extremely sensitive both to the electrical noise and over-voltage, as the gates form a Schottky barrier with the semiconductor. Typically, any voltage outside the [-2 V, +0.3 V] range may result in current flowing to the 2DEG and damaging it. To solve both of these problems, we use Digital to Analog Converters (DACs), which we control using an Field-Programmable Gate Array (FPGA) board programmed with the adequate safeties. The DACs are low noise ($\sim 25\,\mathrm{nV}/\sqrt{\mathrm{Hz}}$), and are connected to the sample via Thermocoax$^{\mathrm{TM}}$ coaxial cables, which possess a low-pass filter behavior of cutoff frequency around $\sim 100\,\mathrm{MHz}$, preventing high-frequency noise from reaching the sample. To enhance this filtering, two low-pass filters (of cutoff frequencies 80 MHz and 1.9 MHz) are placed in series at the top of the refrigerator. Each DAC has a minimum setting time of 16 µs and a resolution of 153 µV.

2.4.2 AWG

Since the coherence time in GaAs is rather short ($T_2^* \approx 12\,\mathrm{ns}$), we need to apply voltage pulses of a sub-ns resolution. For this purpose, we use a Tecktronix 5014B Arbitrary Waveform Generator (AWG), capable of generating waveforms of amplitude ±4.5 V and resolution 833 ps on four different channels. They are connected to coaxial cables, thermally anchored and attenuated on the different stages of the refrigerator (4 K stage, 1 K pot, heat exchangers, mixing chamber).

For the data presented in this thesis, two AWG outputs were connected to the LP1 and RP1 gates, with a total of −20 dB of attenuation. The two other outputs were connected to LP2 and RP2 via homemade bias-T, allowing to DC-polarize these gates as well. For these lines, the total attenuation was −33 dB, bringing the pulse amplitude to ±100 mV (±450 mV for LP1 and RP1). However, because of the limited amount of RF-lines available on the setup, the last portion of these four AWG connections are made of smaller coaxial cables and the contact to the sample holder is not impedance-matched to 50 Ω, limiting the achieved bandwidth. At low temperature, we measured a bandwidth of 800 MHz at 4 K and 1.5 GHz at 65 mK. As we will see later in the experimental data, this has been now identified as a main source of decoherence for the spin shuttling experiments.

2.4.3 SAW generation

The piezoelectric properties of GaAs being rather poor, the conversion from electrical to acoustic pulse is extremely inefficient ($\approx -26\,\mathrm{dB}$). Therefore, we have to apply a high-power microwave burst ($10 - 20\,\mathrm{dBm}$) to produce a SAW with the necessary amplitude to shuttle electrons. The setup being in an dilution refrigerator with a limited cooling power, we typically limit the duration of this microwave burst to a few tenths of ns every ms, for an average dissipated power of the order of a few µW over the different stages of the refrigerator. This microwave burst is synthesized by a Rohde&Schwarz SMA100A signal generator, with a minimum burst duration of 30 ns and a $\sim 1\,\mathrm{ns}$ rising time.

As a consequence of this poor electrical to mechanical energy conversion, electrical noise reaching the IDT has little impact on the central structure. To avoid bringing too much heat conduction to the sample, we place a 6 dB attenuator at the 1K pot stage and an additional 1 dB at the mixing chamber stage. To block the direct capacitive coupling between the IDTs and the nanostructure, we design them 2 mm away from the central structure and place a metallic shield 800 µm above the surface of the sample. We can discriminate this parasitic capacitive coupling from the actual SAW thanks to the propagation time ($\approx 730\,\mathrm{ns}$ for the SAW, 6 ps for the capacitive coupling). In addition, the capacitive coupling has still the same magnitude off-resonance, while the SAW generation is prevented.

For the delay-controlled sending experiments, the jitter between the SAW burst and the AWG pulse generation had to be controlled. Since the Rohde&Schwarz generator has a 10 ns jitter on the trigger detection, we chose this instrument as master and used it to trigger the AWG, leading to a sub-ns jitter between the SAW and the AWG pulses.

2.5 Reflectometry

To read the charge (and indirectly spin) state of the system, we opted for a source-reflectometry technique, consisting in building a resonant circuit embedding the electrometer and measuring the signal reflection at the resonant frequency, dependant on the QPC conductance. Compared to a classical DC current measurement, this technique provides many advantages:

- The measurement bandwidth is greatly increased with respect to the use of a room-temperature DC current to voltage converter. Indeed, the low-pass filter behavior of the DC cables limits the measurement bandwidth to a few kHz. Here, this bandwidth is at least two orders of magnitude greater, limited by the rising time of the low-noise amplifiers ($\sim 1\,\mu\mathrm{s}$) and the resonant circuit bandwidth ($\approx 10\,\mathrm{MHz}$).
- As the signal is modulated at the resonant frequency of the circuit (a few 100 MHz), we are only sensitive to noise within the bandwidth of this resonant circuit. This not only removes low-frequency noise coming from the pumps and power supply (50 Hz noise in particular), but also a great amount of the flicker noise (with a 1/f dependance). Typically, the measurement is only sensitive to white noise, limited by the use of a cryogenic amplifier. Such an amplifier thermally anchored at the 4 K stage has a typical noise temperature slightly above 4 K, corresponding to 100 nV for a 1 MHz bandwidth.

- Finally, this technique allows multiplexing, meaning that several signals can be carried through the same wire without interfering, as long as the different resonances are separated. This last point provides a key argument for scalability, as many qubits can be read-out simultaneously at a rate of a few hundreds of MHz without any crosstalk, using only two RF lines.

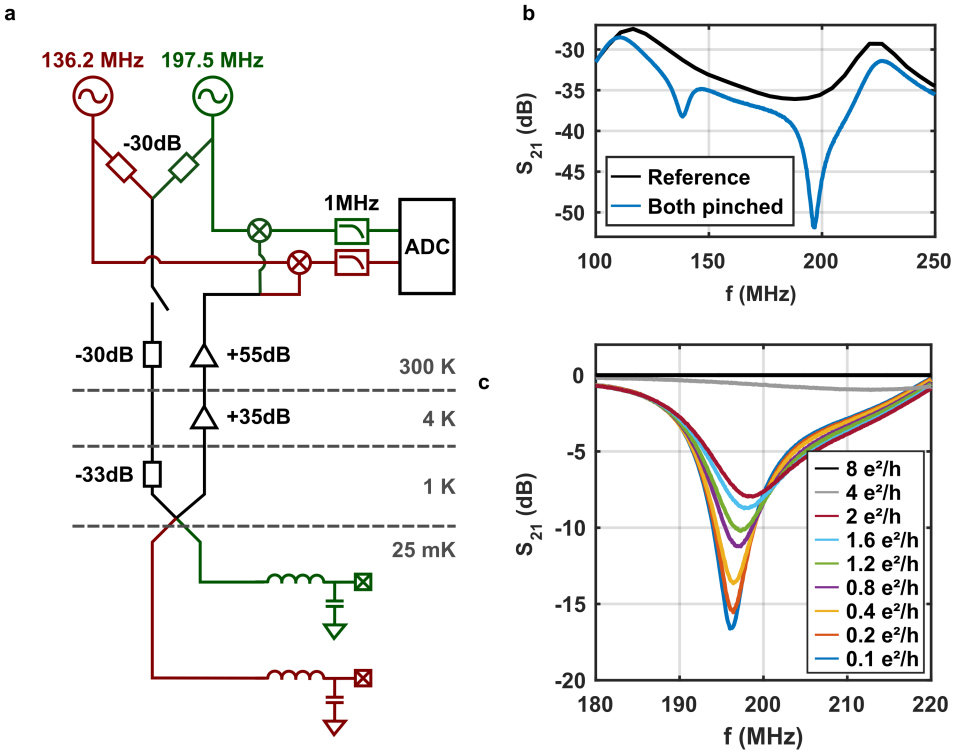

Figure 2.6: Reflectometry setup. a. Scheme of the readout setup. Two RF carriers are attenuated and reflected by the resonant circuits connected to the electrometers. The signal is then amplified, demodulated and sent to an acquisition card. **b.** Magnitude of the reflected signal. The two resonances appear when the electrometer conductance is decreased. **c.** Amplitude of the 197 MHz resonance as the left QPC is pinched-off, with the reference subtracted. The maximum sensitivity is close to 10 dB/$\frac{e^2}{h}$.

2.5.1 Setup

A scheme of the two resonant circuits connected to the sample is visible in Fig. 2.6. The circuits are composed of an inductor (470 and 820 nH) and the parasitic capacitance of the sample holder ($\sim$ 1.4 pF), in parallel of which a 0.2 pF capacitor is added for the right electrometer. To be able to apply DC current through the sample, a bias-T is realized with a 5 kΩ resistance and a 10 µF capacitor, and the DC part is connected to a DAC output with a 1/1000 voltage divider.

The two carriers (136 and 197 MHz) are generated by a Windfreak RF Synthesizer, split and attenuated before entering the refrigerator through the same coaxial cable. As the

power reaching the sample needs to be rather low (under −80 dBm, corresponding to a bias amplitude around 250 µV), the signal is strongly attenuated, with −93 dB in total. At the 1K pot stage, a directional coupler allows the incoming signal to reach the resonant circuits mounted on the sample holder. The reflected signal is sent through this directional coupler to an amplification chain consisting of a Caltech CITLF1 cryogenic low-noise amplifier at the 4K stage and a homemade amplifier at room temperature. They respectively provide +35 and +55 dB amplification, allowing the modulated signal to be brought to a similar power as the two references. This signal is split, demodulated with each carrier using Minicircuit passive mixers, and low-pass filtered at 1 MHz to remove the high-frequency components.

A National Instrument acquisition card digitalizes these two signals (from the two electrometers) at a rate of 100 kS/s per channel and the data is pre-treated of the fly by the measurement software, which will be detailed later. To minimize the noise induced on the sample, a homemade switch with a rising time of 100 ns is used to turn off the incoming RF signals during the spin manipulation.

2.5.2 Sensitivity evaluation

As we can see Fig. 2.6.b., the amplitude of each resonance dependant on the electrometer conductance. Focusing on the left electrometer, we progressively reduce the conductance by applying a negative voltage on LD1. While for an open QPC ($G \gg \frac{2e^2}{h}$), the resonance is barely visible, its amplitude increases as the QPC is pinched off, reaching around 20 dB more for a completely closed QPC. From the tangent of the $S_{21}(f_0) = f(G_{\mathrm{QPC}})$ curve, we can extract the sensitivity, which is in our case up to 10 dB/($\frac{\mathrm{e}^2}{\mathrm{h}}$). As the typical QPC sensitivity is around 0.15 $\frac{\mathrm{e}^2}{\mathrm{h}}$ per electron, this gives a 750 nV amplitude difference in the reflected signal for 1 or 2 electron occupying the dots, before amplification.

To study in more details the sensitivity of our reflectometry setup, we feed the demodulated signal of the left electrometer to a LeCroy WaveRunner HRO 6Zi oscilloscope, and we reconstruct the data histogram for one or two electrons loaded in the left double quantum dot (Fig. 2.7). As we vary the integration time, we observe two Gaussian distributions separated by 2.67 mV and whose standard deviation increase as the square root of the measurement rate, as expected for a white noise distribution. Placing a threshold at $V_{\mathrm{RF,L}} = 51.4\,\mathrm{mV}$, we define the signal to noise ratio (SNR) as the Gaussian distributions separation divided by the sum of their standard deviation. The $SNR = 1$ threshold is reached for an integration time of 6 µs, and the error on the charge assignment drops below 5 % for an integration time of 30 us. The extracted charge sensitivity is $2.4 \times 10^{-3}\,\mathrm{e}/\sqrt{\mathrm{Hz}}$, comparable to the one measured by Reilly *et al.*[Rei07]

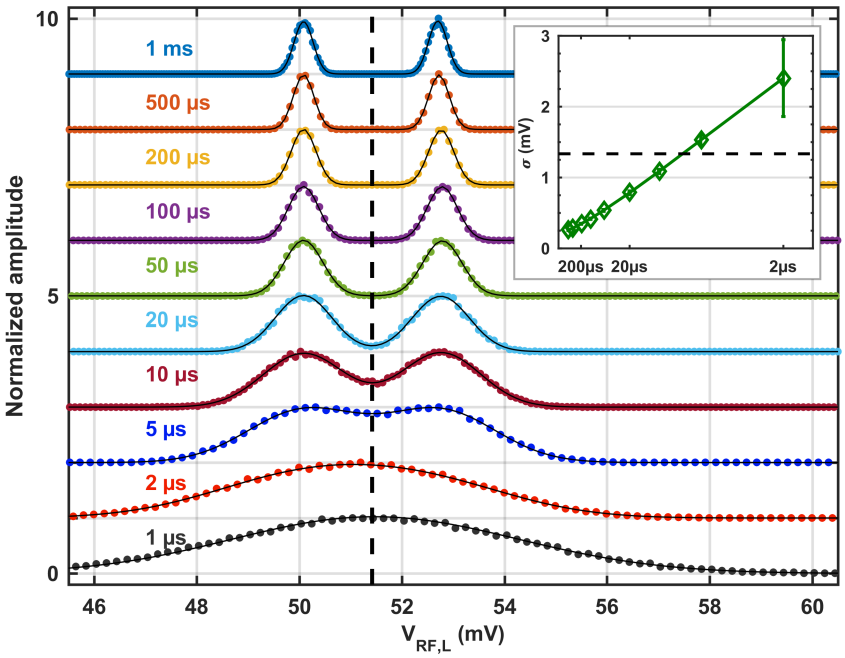

Figure 2.7: Noise distribution. Histogram of the signal obtained by loading successively 1 or 2 electrons in the left quantum dot as a function of the integration time. The curves have been normalized and offset for clarity, and fitted with a double Gaussian distribution (solid black line). The dashed black line represents the threshold used for charge assignment, positioned in the middle of the two peaks. **Inset.** Extracted standard deviation of the 2 electron Gaussian peaks as a function of $1/\sqrt{t_{\mathrm{meas}}}$. The noise is inversely proportional to the square root of the integration time, and overcomes the threshold for $t_{\mathrm{meas}} < 6\,\mu\mathrm{s}$ (SNR$= 1$). For $t_{\mathrm{meas}} > 30\,\mu\mathrm{s}$, the charge readout fidelity is greater than 95 %.

2.6 Measurement software

The whole measurement is piloted by a Python/Labview software, which was constantly updated throughout the work presented in this thesis. The precise evaluation of the limits and performances of each instrument allowed us to build a safe, fast, efficient and upgradable measurement software, allowing us to gain two orders of magnitude in the measurement speed compared to the work realized on the previous sample. In addition, to handle the complexity and variety of the required data analysis, a set of analysis scripts were created, allowing to perform semi-automatic treatment of the raw data.

2.6.1 Measurement sequence

At the core of the measurement is a Labview program, in charge of communicating with the different instruments. This program follows a measurement file generated by a Python software with a higher programming level, easily understandable by users. The Python part ensures the compatibility between the different instrument settings, while the Labview program simply plays the sequence and recovers the data.

As the communication between the Labview program and the instruments via a LAN

a

```
#########################
###  FAST SEQUENCE
#########################
seq = []
seq +=[['Trigger','1110']]
seq +=[['Timing',0.1]]
seq +=[['Trigger','1010']] # START ADC

seq +=[['LH3',0.3]]
seq +=[['LH2',0.08]]   # LOAD 2e
seq +=[['Timing',0.1]]

seq +=[['LH3',0.15]]   # ISOLATE
seq +=[['LH2',0.1]]

seq +=[['Trigger','1011']]
seq +=[['Timing',0.2]] # CHARGE SENSING
seq +=[['Trigger','1010']]

seq +=[['LH3',0.]]   # PULSE TO (X,Y)
seq +=[['LH2',-0.05]]
seq +=[['LH3',0.1]]
seq +=[['Timing',0.1]]

seq +=[['LH3',0.]]   # COME BACK
seq +=[['LH2',0.1]]
seq +=[['LH3',0.15]]

seq +=[['Trigger','1011']]
seq +=[['Timing',0.2]] # CHARGE SENSING
seq +=[['Trigger','1010']]

seq +=[['Jump',2]]  # JUMP
Map.sequence = seq

#########################
###  MAP
#########################
Map.sweep_dim = [20,51,51]
Map.segment_param = [159.6, 36, 40, 84, 40]
Map.ramp_slot(12,'dLH2_{meta}',-0.1,0.2,2)
Map.ramp_slot(13,'dLH3_{meta}',0.,0.45,1)
```

b

```
bounds_left = [-0.55,-0.2,+0.2,+0.6,+1.05];

%% Data histogram
figure(91);clf();hold on;
V_L = exp.readout(1).data(:);
valid = V_L~=0;
V_L = V_L(valid);
hist = histogram(V_L,100,'DisplayStyle','tile');
y_lim = get(gca(),'YLim');
for i=1:length(bounds_right)
    plot([bounds_right(i) bounds_right(i)],y_lim,...
    'LineStyle','--','Color',[0.3,0.3,0.3],'LineWidth',0.75);
end
ylim(y_lim);
set(gca(),'FontSize',14);
xlabel('\DeltaV_{RF,L}');
ylabel('Counts');
title('Histogram of QPC signal');

%% Converting to charge
NL = signal2charge(exp.readout(1).data,bounds_left);

%% Create virtual readouts
exp.readout = [];
for i=0:4
    exp.readout(i+1).name = ['P (N_L = ' num2str(i) ')'];
    exp.readout(i+1).unit = '';
    exp.readout(i+1).data = NL==i;
end
exp.readout_list= {exp.readout(:).name};

run('Auto_avg.m');  %% Average the first dimension
```

c

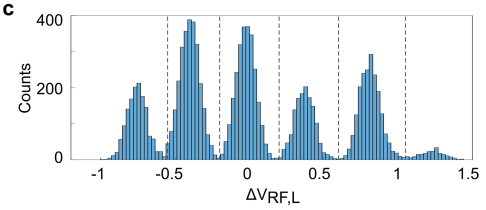

Figure 2.8: Script example. a. Part of a "losing map" script. The fast sequence contains the trigger, DAC and wait instructions. The data dimensions, varied parameters and pre-analysis information are specified at the bottom. **b.** Analysis script for this experiment. An histogram of the data is plotted, allowing the user to specify thresholds. The 0 to 4 electrons probability are computed for each (RH2, RH3) position. **c.** Data histogram output by the analysis script.

network is rather slow compared to our measurement bandwidth ($\sim 1\,\mathrm{kHz}$ and $100\,\mathrm{kHz}$ respectively), the performances are enhanced by playing a pre-programmed sequence and triggering the acquisition, recovering many data points for every communication. For this purpose, we program into the FPGA board controlling the DAC outputs a sequence with different orders:

- update one DAC output, with a $16\,\mu\mathrm{s}$ setting time.
- wait a certain amount of time (from $1\,\mu\mathrm{s}$ to several hours).
- generate a rising/falling on a trigger output, connected to another instrument (e.g. AWG or SAW generation). One of these trigger output is used to control the RF switch and turn the reflectometry measurement on and off.

- jumping to another slot in a sequence, for example to loop the same sub-sequence.

Figure 2.8 shows an example of measurement sequence, corresponding to a "losing map", where the ability to hold two electrons isolated from the reservoir is evaluated. In practice, a 100 µs pulse to an arbitrary configuration (RH2, RH3) is applied, before and after which the QPC signal is recorded for 200 µs. This mesurement is repeated 20 times, and the (RH2, RH3) position is varied.

2.6.2 Analysis script

A partial data treatment can be done by the Labview program (downsampling, average, difference between two segments), but the main analysis is done using Matlab scripts. Throughout the work covered in this thesis, over 100 of these scripts were created, from basic (smooth, reshape, concatenation of several experiments) to advanced (spin fidelity extraction, drift compensation, conditional probabilities).

Coming back to the previous example, the Labview pre-analysis consists in cutting the waveform into 20 segments, extracting the average signal recorded during the two 200 µs readout steps, and saving for each segment the signal difference into a measurement file. This data is imported into the Matlab program and a histogram is plotted, allowing the user to specify thresholds for every charge state. A script then computes the probability to hold 0, 1, 2, 3 or more electrons for every (RH2, RH3) position. Finally, this treated data is sent to an user interface able to display 1D curves and 2D surfaces, as well as perform additional data treatment (derivative, FFT filter).

Such a high-level, semi-automatic analysis scheme is a key tool to speed-up the data understanding. In addition, as the reflectometry signals are drifting over several hours or when the magnetic field is swept, features such as automatized peak recognition and drift compensation are of paramount importance for the realization of long measurements.

CHAPTER 3

Charge isolation and SAW-assisted transport

Since our qubits are encoded in electron spins, their manipulation always relies on some operation on the electrons themselves. The fidelities of these manipulations are often limited by the degree of control over the charge degree of freedom. In this chapter, we introduce several techniques implemented to measure and control the charge configuration of our double quantum dots. We focus on the isolated regime, where tunneling to and from the reservoirs is prevented, enhancing the degree of control over the charge occupancy. Finally, we study electron shuttling using the SAW trapping potential and our ability to transport two electrons with a ns-controlled delay.

3.1 Charge control and isolation

As developed in the previous chapters, we use a local electrometer coupled to a reflectometry setup to probe the charge occupancy of each double quantum dot. We can see Fig. 3.1.a. that, for this particular electrometer configuration, an electron addition leads to a more negative environment for the electrometer, and a lower conductance. In the following work, the electrometer is always placed in a similar configuration with a negative slope, allowing us to discriminate an electron exiting (positive shift) or entering the dot (negative shift). From the signal magnitude we can deduce which dot is concerned, as their coupling with the electrometer is slightly different. This coupling difference would also allow us to observe inter-dot transitions, but for this particular geometry the signal shift is rather weak as the electrometer is almost equally coupled to each dot.

To study the charge occupancy of the double-quantum dot, we monitor the electrometer conductance as a function of two wisely chosen gate voltages. This so-called *stability diagram* is a great source of information on the electrostatic potential landscape and the effect of each gate. From the study of such an experiment, we can infer the number of formed quantum dots, their position and absolute charge occupancy. We can also measure the inter-dot coupling between a pair of quantum dots, as well as the coupling to the electron reservoir.

3.1.1 Stability diagram

If we fix the electrometer at a sensitive position and ramp RH3 toward more negative values, we observe a general trend due to capacitive coupling with the detector, as well

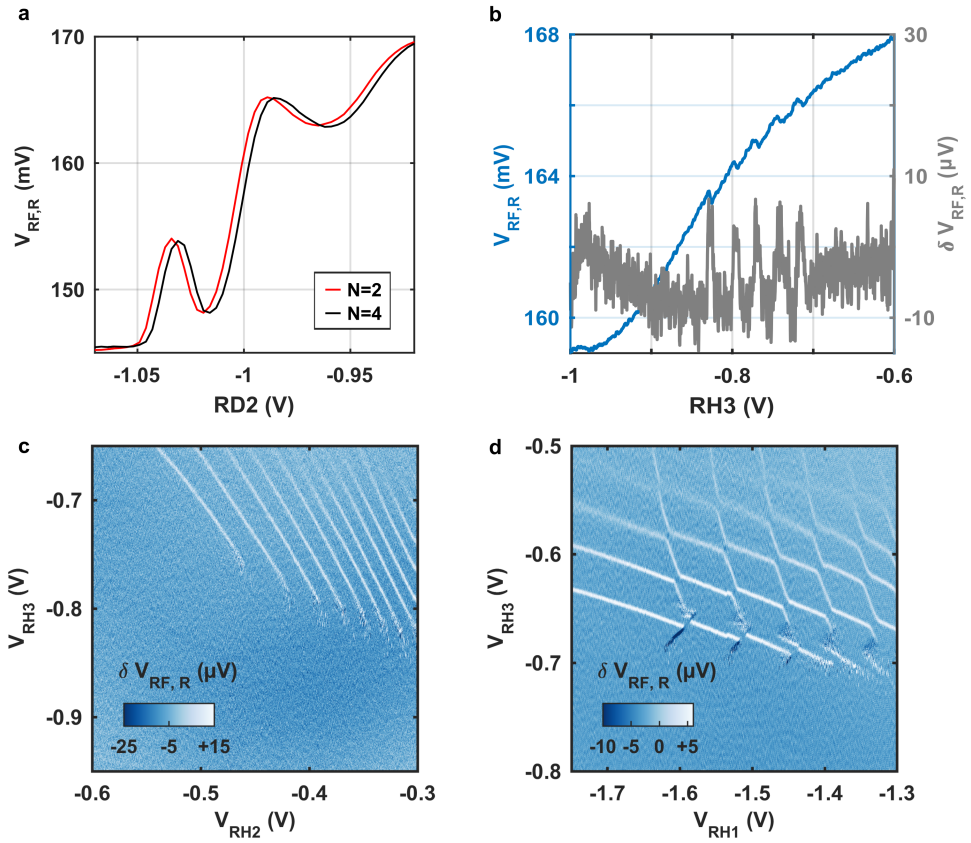

Figure 3.1: Stability diagrams. a. Example of QPC trace for 2 or 4 electrons loaded in the reservoir dot. At $V_{\mathrm{RD2}} = -1\,\mathrm{V}$ the QPC is sensitive and far enough from pinch-off. **b.** QPC signal as RH3 is swept. Abrupt shifts (also visible on the signal derivative, in gray) correspond to one electron leaving the quantum dot. **c.** Derivative of the QPC signal as a function of RH2 and RH3 for a single dot regime. The electron number in the reservoir dot varies from 0 (left) to 13 (top right). **d.** Derivative of the QPC signal as a function of RH1 and RH3 for a double dot regime. The vertical (resp. horizontal) lines correspond to electrons leaving the channel (resp. reservoir) dot. The inter-dot avoided crossings are well visible, as the two dots are here strongly coupled ($\gg 1\,\mathrm{GHz}$).

as abrupt signal jumps (blue curve Fig. 3.1.a.). These jumps are associated with single electrons tunneling to the reservoir, as the quantum dot potential is raised. Between two jumps, the electron number is fixed. Since the electrometer signal does not decrease as the dot is emptied, we can identify the last electron tunnel-out, and thus infer the absolute electron number for every transition.

If we repeat this sweep for different values of RH2 and plot the derivative of the signal (to remove the capacitive coupling), these jumps appear as lines in Fig 3.1.cd. From the line slope, we can extract the ratio of gate lever arm (conversion factors from gate voltage to energy, called α-factors), and estimate the dot position. Here, a negative shift on RH3 can be compensated by a positive shift of RH2 of slightly greater magnitude, meaning that

their coupling to the dot is similar. This indicates that the dot is equidistant to RH2 and RH3, in agreement with the sketched position of the reservoir dot in Fig. 2.1.

If we lower the RH1 gate, we see the emergence of a double quantum dot behavior, as visible in Fig 3.1.d. Here we have two sets of lines, one for each dot. The more vertical lines correspond to a dot more coupled to RH1 than RH3, the channel dot. Contrarily, the more horizontal lines correspond to the reservoir dot, more coupled to RH3. In this diagram, we can therefore identify every charge configuration (N_c, N_r), down to the single electron limit.

3.1.2 Isolated regime

In the single-dot regime stability diagram (Fig. 3.1.c.), we can see the transition lines fading out for $V_{RH3} < -0.8\,V$. This is a signature of the isolated regime, a metastable state in which the coupling to the reservoir is much smaller than the measurement time. Indeed, because of its geometry, the RH3 gate has two effects on the quantum dot. Applying a more negative voltage on this gate raises the dot potential, but also increases the tunnel barrier to the electron reservoir. Thus, the reservoir coupling is shut off and electrons are prevented from tunneling to the reservoir, even though their chemical potential is higher than the Fermi energy.[Ber15b]

To prove our ability to isolate two electrons in the right part of our structure, we perform a *losing map* experiment, presented in Fig. 3.2. It consists in loading two electrons and recording a reference signal at a measuring point M within the isolated regime. The system is then pulsed for 1 ms to a position P=($V_{RH2,\,P}$, $V_{RH3,\,P}$), and brought back to the point M for another measurement. Fig. 3.2.b. shows the signal difference as the position P is varied, each pixel being a single-shot realization. We can immediately identify in the top part of this plot the $N = 0$ to $N = 7$ areas, whose boundaries are at the same positions as the lines in the stability diagram Fig. 3.2.a. Here, the pulse to P opens the coupling to the reservoir and allows electron exchange. The final number of electrons thus only depends on P.

Contrarly, when $V_{RH3,\,P}$ is kept more negative (bottom part of the plot), the electron number is unchanged, as the coupling to the reservoir remains several orders of magnitude slower than the 1 ms pulse duration. In this isolated regime, a fixed number of electrons can be kept throughout the measurement sequence, facilitating the charge readout. Moreover, the double quantum dot potential manipulation is simplified, as no absolute potential reference is given by the reservoir. Finally, this isolated regime is crucial in our experiment, to protect the system from parasitic electron exchange with the reservoir while the potential is modulated by the SAW.

The following results were all obtained using this isolated regime, the coupling to the reservoir being only momentarily turned on for initialization and spin to charge projection. This allows us to always measure the output charge configuration at the same position, regardless of the type of experiment, facilitating the electrometer tuning and the analysis.

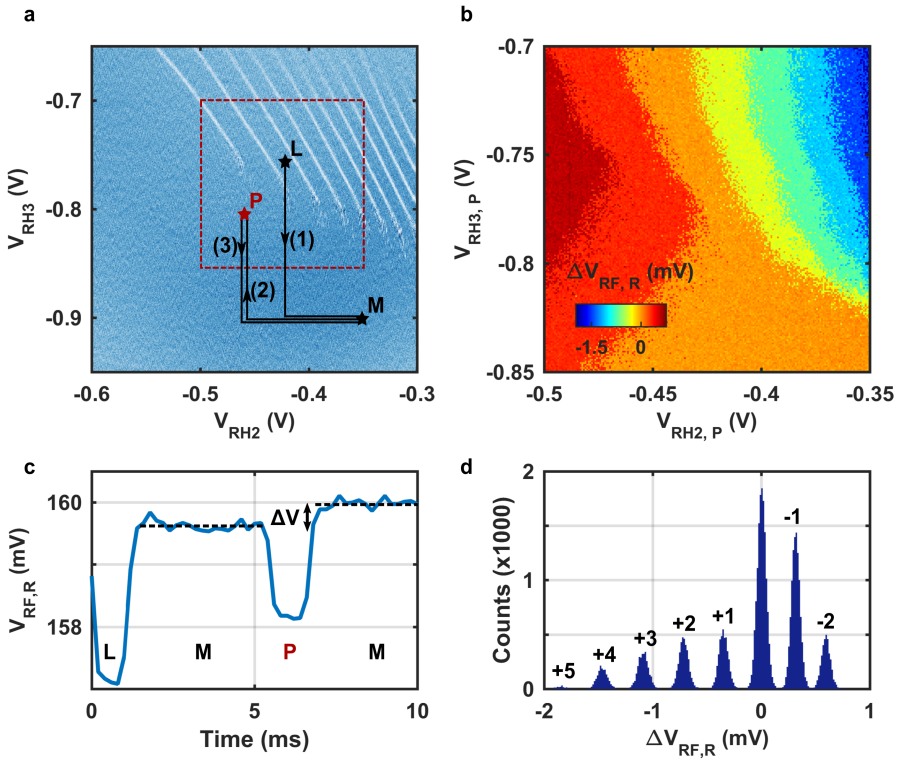

Figure 3.2: Isolated regime. a.c. Two electrons are loaded into the reservoir dot (L), after which the system is brought to the isolated regime (M) and a reference signal is recorded for 4 ms. The dot is then pulsed to an arbitrary (RH2, RH3) configuration (P) for 1 ms, and brought back to the measuring position for 4 ms. P is varied in within the red dashed rectangle. **b.** Single shot difference of QPC signal as a function of the position of P. For $V_{\mathrm{RH3,\,P}}$ positive enough, the dot can exchange electrons with the reservoir and the final number of electrons is the same as given by the stability diagram, from 0 (red) to 7 (blue). As $V_{\mathrm{RH3,\,P}}$ is kept negative enough, 2 loaded electrons can be kept in the dot for a large range of $V_{\mathrm{RH2,\,P}}$ (orange area). **d.** Signal difference histogram. The corresponding difference in number of electrons, with respect to the N=2 initial configuration, is indicated for every peak.

3.2 SAW-assisted transport

Now that we can isolate a given number of electrons, we can generate a SAW burst and study the electron propagation across the channel. Figure 3.3.a. and b. show two identical single-shot losing maps, with the addition on b. of a 18 dBm, 50 ns microwave burst applied on the transducer at its resonant frequency. We observe a large area where two electrons can be kept without the SAW burst, but are ejected when the SAW is turned on. This is a first demonstration that the SAW is able to kick electrons out of the right channel dot, but not necessarily towards the channel.

We thus perform a similar experiment focusing on the left side of the structure, loading two electrons on the right channel quantum dot and bringing its potential to a position where both electrons are sent by the SAW ([−1.8 V, -1.6 V] on Fig. 3.3). We measure the

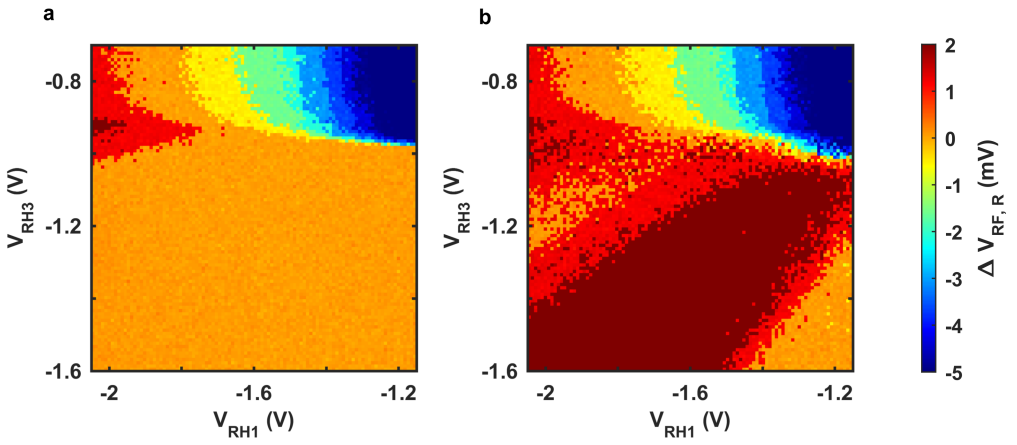

Figure 3.3: Sending map. a. Reference losing map. **b.** Same experiment, with the addition of a 18 dBm, 50 ns SAW burst applied while the system is at the pulsed position P. We can see the effect of the SAW on the lower part of the plot, with an area (in red) where two electrons can be kept without the SAW, but are ejected from the right double-dot if a SAW burst is applied.

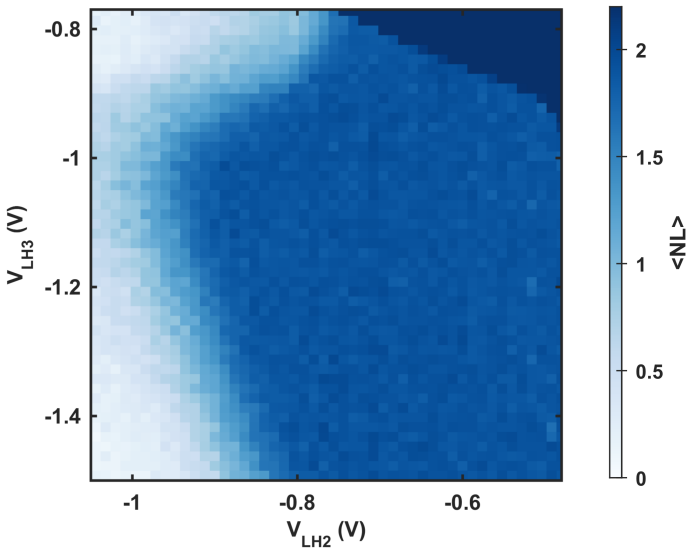

Figure 3.4: Catching map. Average charge caught in the left channel quantum dot as a function of V_{LH2} and V_{LH3}. Two electrons are loaded on the right side on the nanostructure and sent across the channel, after which the caught charge is inferred from the left electrometer signal. We observe a large area in the isolated regime where both electrons are caught with a high ($> 90\,\%$) probability.

charge occupancy of the left side of the structure for various reception configuration, in order to identify the ideal catching position. This *catching map*, shown Fig. 3.4., presents a large area where the probability to catch both electrons is above 90 %. For $V_{\mathrm{LH2}} < -0.9\,\mathrm{V}$, the quantum dot potential is too high and the incoming electrons either continue towards the reservoir or are stopped further in the channel. For $V_{\mathrm{LH3}} > -0.9\,\mathrm{V}$, the left double quantum dot is not in the isolated regime and electron tunnelling to (top-left corner) or from (top-right corner) the reservoir can occur, affecting the final charge state. In the following experiments, we use ($V_{\mathrm{LH3}} = -1.2\,\mathrm{V}$,$V_{\mathrm{LH2}} = -0.6\,\mathrm{V}$) as catching position.

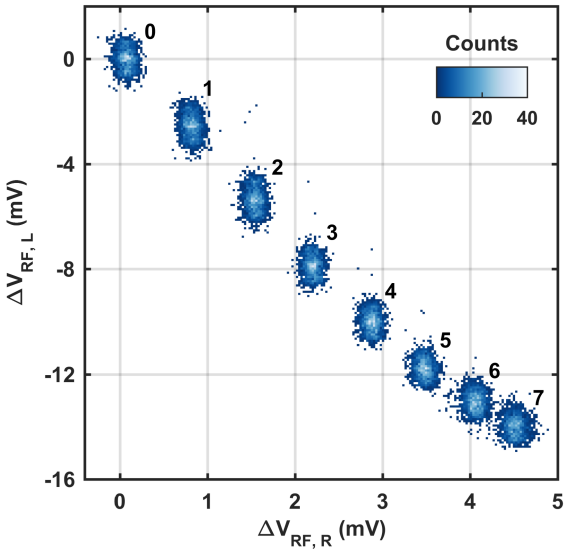

Figure 3.5: Multiple charge sending. 2D-histogram representing the number of counts of the signal shift $\Delta V_{\mathrm{RF,L}}$ and $\Delta V_{\mathrm{RF,R}}$ as the number of transferred electrons is varied. The left dot is initially empty, and the right dot is loaded with N electrons. When no electrons are loaded, no signal shift is observed on either side (N=0, top-left peak). As we load more electrons (up to 7 for the last bottom-right peak), we always observe opposite shifts on each side, proving that the numbers of caught and sent electrons are the same. The fidelity is above 98 %, the errors mainly corresponding to one electron not arriving in the receiving dot.

The optimal sending and catching configurations being determined, we test our ability to transfer several electrons. We initially empty the left double quantum dot, and load in the right double quantum dot a given number N of electrons. We then measure the difference of electrometer signal before and after the transfer, on both sides. We expect a positive shift on the right side, as N electrons leave the dot, and a negative shift on the left side. In addition, the magnitude of each shift should be proportional to N.

Figure 3.5. shows a two-dimensional histogram of the signal shift of each electrometer, allowing us to visualize the correlations on each side. Data from 2000 single-shot experiments are computed for $N = 0,1,...,7$. We observe 8 peaks, from $N = 0$ where no shift is recorded on either side, to $N = 7$ where the shift amplitude is the largest for each electrometer. This allows us to estimate the transfer fidelity, which is always above 95 %, and in particular

above 98 % for $N = 2$. This experiment proves that when N electrons leave the right side, N electrons are caught on the left side. The few errors occur when one electron does not reach the left dot, either because it got trapped in the channel or because the left quantum dot was not able to stop it.

For the two electron spin transfer experiments, presented later in this thesis, we always measure the charge immediately after transfer to eliminate the few $(2-4\,\%)$ sending errors from the statistics. Indeed, as we require some spin-to-charge conversion and another charge measurement to infer the spin state, these charge transfer errors (e.g. only one electron arriving) would artificially increase one of the spin population (triplet state in this example).

3.2.1 Effect of the SAW burst power and frequency

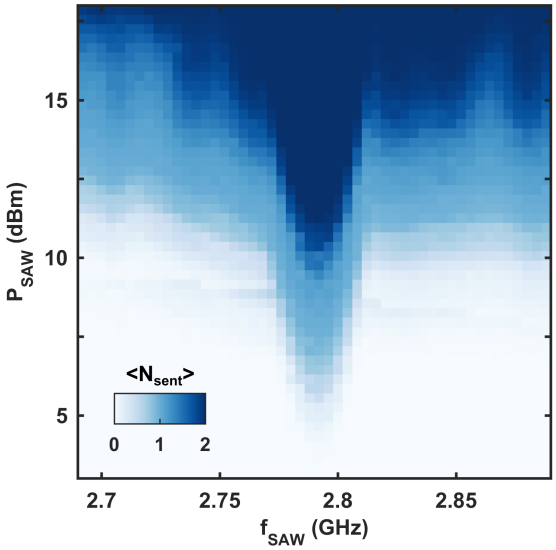

Figure 3.6: Effect of the SAW parameters. Average number of sent electrons as the SAW burst power and frequency is varied, for two electrons initially prepared in the sending dot. Electron sending is facilitated when the IDT is excited at its resonant frequency (2.79 GHz), and in this case is carried out by the generated SAW. Out of resonance, electron sending can also occur by capacitive coupling to the gates, but only for a greater power applied on the IDT.

Because of the rather fast travel time ($t_S = 2.1$ ns) of electrons at the SAW speed, we cannot discriminate this acoustic transport from *hot* electrons, kicked of the quantum dot by a potential modulation, and travelling several orders of magnitude faster than the SAW itself. For our electrometers, the sending and catching appear simultaneous in both cases. However, the SAW is generated only if the transducer (IDT) is excited near its resonant frequency, allowing us to discriminate the two types of transport.

Experimentally, we empty the receiver side and load two electrons on the sending side. We then apply a microwave burst of duration 100 ns and variable frequency and amplitude. Figure 3.6 presents the average charge sent, with 1000 repetitions per pixel. Indeed, we

observe that sending is facilitated when the frequency of the microwave burst matches the one of the IDT. In this resonant case, we can resonably assume that the transfer is mostly achieved via the SAW moving potential, and that electrons are confined throughout their transport.

For off-resonance microwave excitation, electrons can still be kicked out of the right dot (light- and darker-blue areas), but the required power is greater. In this case, the proposed mechanism is the capacitive coupling between the IDT and the double-dot gates, modulating the gate potential and allowing the electron to escape the trapping potential. In this case, the electron is not confined during transport, will likely get stuck in the channel, and may not be kicked towards the channel altogether.

To mitigate this uncontrolled excitation of our structure, we placed a metallic shield 800 µm on top of the sample (the IDT is 2 mm away from the right double-dot), to absorb most of the radiation and reduce the capacitive coupling. We also tune the microwave burst precisely at the IDT resonant frequency, reduce as much as possible its duration, and limit the applied power. Finally, the triggered injection (discussed in the following paragraph) protects the electron until the SAW reaches the right double-dot, effectively preventing non-acoustic transport.

3.2.2 Delay-controlled sending

As of now, we have very little control over the dynamics of the electron transfer. The shortest possible microwave burst (30 ns) corresponds to the generation of 150 moving quantum dots, and we cannot determine in which one each electron travels. Yet, in order to keep the singlet-triplet qubit coherence during its transfer, a key requirement is to send separately the two electrons with a delay controlled at a timescale smaller than the typical decoherence time of the singlet state, measured to be close to 10 ns in GaAs. To achieve this goal, we keep the system in a configuration where the moving SAW potential alone cannot send the electrons. To trigger each electron injection, the dot potential is momentarily raised by applying a ns voltage pulse on RP1, synchronized with the SAW passage. This way, we can trigger the injection of each electron into two different moving quantum dots with a ns resolution and introduce a controlled delay.[Ber16b; Her11]

We can see Fig. 3.7 that this technique indeed allows us to control the number of electrons injected, from 0 to 2 in this case. In order to perform such a delay-controlled sending we need to apply two AWG pulses, a first one at $t = 770$ ns with an amplitude of -0.1 V to inject the first electron, followed by a delayed second pulse of maximal amplitude (-0.45 V) to inject the second electron. The curves presented Fig. 3.7 allow us to estimate the fidelity of this charge transfer protocol, as the first electron is correctly sent by the first voltage pulse in 82 % of the single-shot realizations. Otherwise, this electron can be sent together with the other electron (13 %) or remain in the right quantum dot (5 %). In the later case, the final number of charges on both sides of the structure is incorrect and we can remove these data points from the analysis. In the former however, two electrons are actually sent, but not without the intended delay. This error rate will affect the singlet spin probability, as visible in the data presented in the last chapter of this thesis. However, we point out here that even when both electrons are sent by a single voltage pulse they are unlikely to travel in the same moving quantum dot, due to the combined action of the

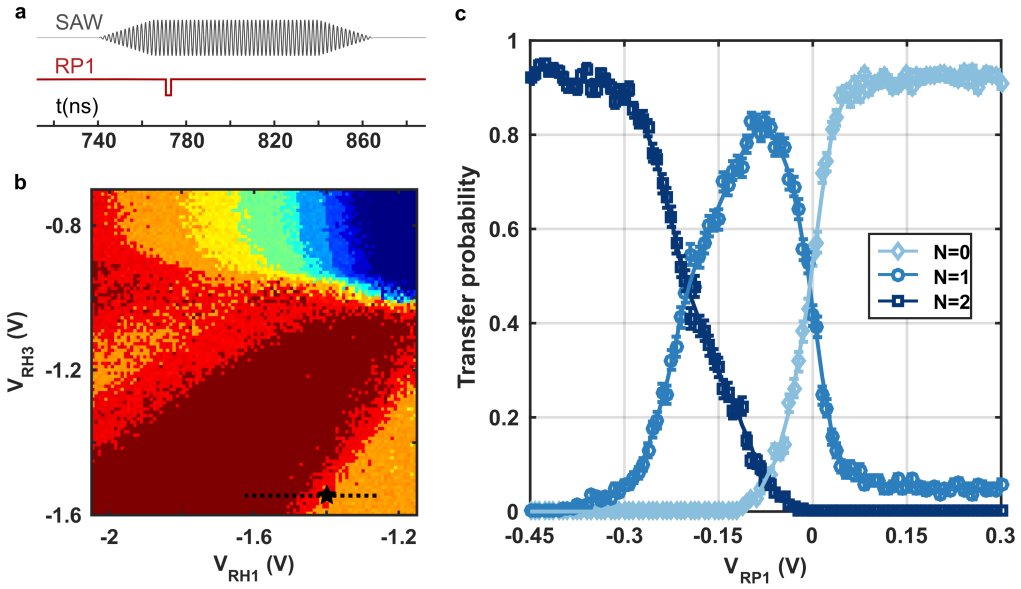

Figure 3.7: Controllable injection in moving quantum dots. a. A 2.1 ns AWG pulse is applied on RP1, synchronized with the SAW arrival, to momentarily raise the channel dot chemical potential and facilitate the injection into the moving quantum dots train. **b.** Sending position (star) used for this measurement. RP1 has approximately the same effect as RH1, with half the alpha factor. The dotted line indicates the span covered when varying RP1 from −0.45 V to 0.3 V. **c.** Probability to successfully transfer 0, 1 or 2 electrons as a function of the RP1 pulse amplitude, over 500 single-shot realizations for each point. The burst applied on the SAW is 18 dBm. We can see that the number of charge injected can be controlled at the nanosecond timescale with a high precision (> 80 %).

sending pulse rising time and the Coulombian repulsion.

To verify our ability to perform this time-resolved injection, we need a detection procedure at the reception dot able to probe the arrival time of each electron. It consists in applying a time-resolved voltage step on LP1 of the reception dot, jumping from a position where electron catching is unlikely to a more suitable receiving configuration. Any electron arriving before this step occurs will not be caught, allowing us to measure each electron electron travel time, as well as their separation.

Figure 3.8 shows the average charge caught as a function of the sending and catching delays. Three different charge regions are observed and correspond to the catching voltage step happening before, between or after the arrival of the two electrons, leading to the capture of 2, 1 or 0 electrons in the receiver dot, respectively. The boundaries between the three visible domains correspond therefore to the first and second electron arrival time.

We can extract two main results from this diagram. Firstly, each electron arrives indeed 2.1 ns after its injection time, proving that they travel at the speed of sound and are confined by the SAW potential throughout their transfer. Secondly, when the electrons are injected with an arbitrary delay ($\Delta t_{\text{sending}} = 0$ to 70 ns), they arrive with the same delay, proving our ability to control this introduced delay with a 1 ns resolution, limited by the

voltage pulses rising time.

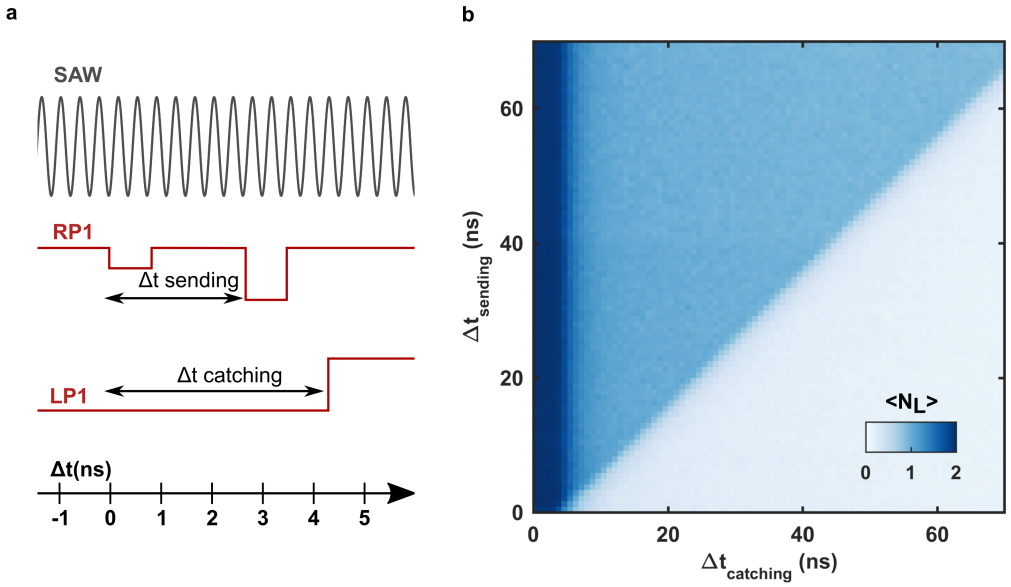

Figure 3.8: Delay-controlled sending. a. Scheme of the injection timing measurement. Two voltage pulses of a nanosecond duration, synchronized with the SAW burst, are applied on RP1 of the sending dot to trigger the injection of the two electrons into the moving quantum dots. To measure the electron distribution in the moving dots, the reception dot is kept in a configuration where electron catching is unlikely until a positive voltage pulse on LP1 is applied. We take the first electron injection as the reference time $t = 0\,\text{ns}$. **b.** Average charge caught on the reception dot depending on the injection and catching pulses delays. Each pixel is the average of 4000 single shot realizations. The vertical and diagonal boundaries correspond to the arrival time of the first and second electron, respectively. The vertical boundary begins at $t_S = 2.1\,\text{ns}$ as a consequence of the time of flight at the SAW velocity of the first electron between the two static dots. Moreover, the clean and sharp diagonal boundary with unity slope confirm our ability to control the separation of two electrons by up to 70 ns with a nanosecond resolution, using a double AWG voltage pulse. The precision of the sending is measured close to a nanosecond and fixed by the rise time of the AWG.

3.3 Conclusion

In this chapter, we have shown our ability to control and measure the charge degree of freedom of our double quantum dots. The isolated regime, where tunneling to and from the reservoir is suppressed, allows for an easier charge manipulation and readout. We studied extensively electron transport across the channel via the moving potential created by the surface acoustic wave. We discussed the effect of the sending and receiving configurations, as well as the SAW burst power and frequency, and demonstrated the simultaneous transfer of up to seven electrons with a fidelity above 98 % for two electrons.

Focusing on the case of two electrons, we demonstrated our ability to trigger electron injection into a specific part of the moving dot train via the application of a double-voltage pulse, controlled by an AWG with a ns resolution. We checked the electron propagation time, consistent with the SAW velocity, and proved our ability to control the injection delay between the two electrons.

This high degree of control over the charge degree of freedom is required to perform the complex spin manipulations described in the following chapter. Furthermore, a well-controlled transfer procedure is of paramount importance to avoid decoherence induced by electron separation.

CHAPTER 4

Spin manipulation and displacement

As mentioned in the first chapter, we encode our qubit information into the spin degree of freedom of the electron rather than its charge, more susceptible to charge noise and decoherence.[Li15; Pet04] Addressing the spin is more challenging, as its measurement is indirect and relies on a spin-to-charge conversion mechanism. Furthermore, as explained in the previous chapter, a high level of control over the charge manipulation is mandatory to operate on the electron spins. In this chapter, we study the physics of a singlet-triplet qubit, from its initialization and readout to the processes limiting its coherence. We demonstrate coherent exchange oscillations, performed in a static double quantum dot configuration, before studying the impact of the SAW modulation on a static qubit. Finally, we demonstrate a delocalized spin measurement, transferring the electrons via the SAW before reading out their spin on the other side of the nanostructure.

4.1 Initialization and readout

As for the charge control, the following results on spin manipulation and transport rely on a wide variety of experimental techniques and optimization steps. Describing them all in detail would be out of the scope of this thesis, therefore we will only cover the ones most relevant to understand the spin results presented later in this chapter. However, we point out here that most of the measurement speed increase, allowing for a greater volume of and cleaner data, has been achieved thanks to newly developed faster spin manipulation techniques. The good understanding of the spin qubit physics in GaAs, together with an optimization of the electronic equipment speed, has lead to a tenfold increase in the single-shot repetition rate, key element in a field statistical by nature.

4.1.1 Initialization

A good example of this optimization is the spin initialization. While it usually consisted of loading an arbitrary spin state and waiting for its relaxation to the ground state (several tenths of milliseconds), nowadays relaxation hot-spots are used to speed up this process down to a few microseconds, without any loss of initialization fidelity.[Yan13] In this work we exploited another technique, presented in Fig. 4.1., where the electron spin is adiabatically loaded into its ground state.

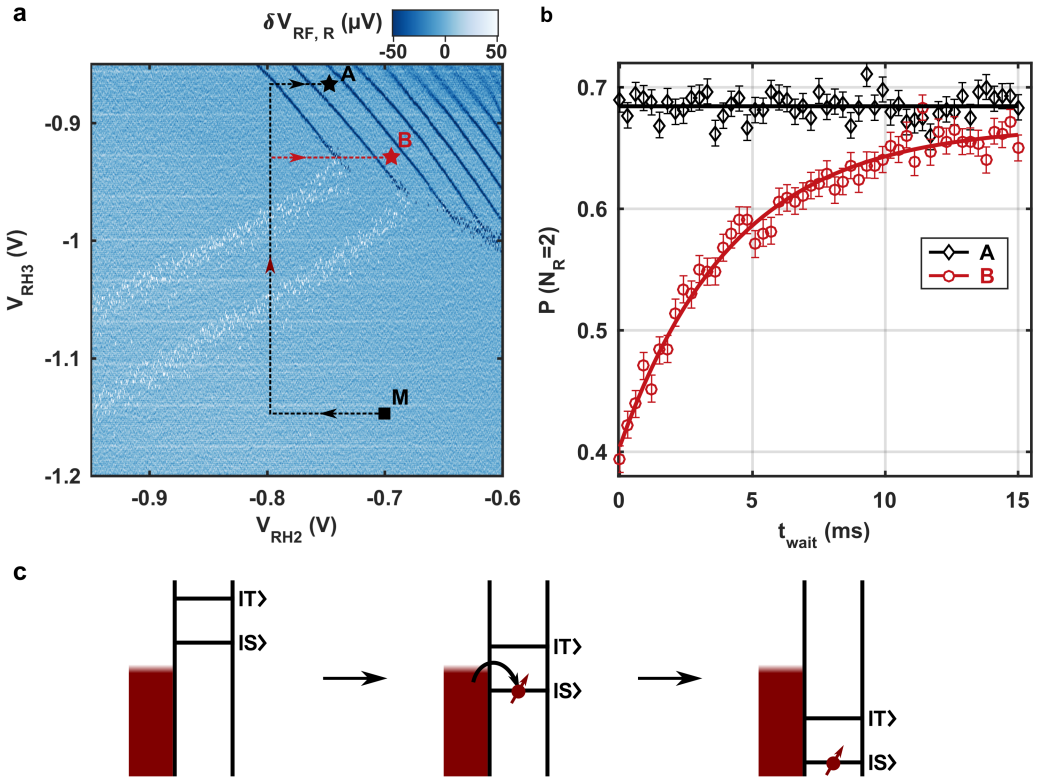

Figure 4.1: Spin initialization. a.c. Scheme of the loading procedure. The quantum dot is emptied by raising its potential and increasing the coupling to the reservoir, after which two electrons are loaded by pulsing to the position A or B and the system is brought to the isolated regime (M). **b.** Singlet spin probability as a function of waiting time for the two loading positions. Using B, mostly a triplet spin state is loaded and relaxes with a characteristic time $T_1 = 4.3 \pm 0.2\,\mathrm{ms}$. Increasing the reservoir coupling during the loading (position A) leads to a high-fidelity direct singlet initialization in 64 µs.

When two electrons are loaded into a quantum dot, the probability for their spin to form a singlet state is usually low. The underlying physical phenomenon explaining this property is the difference of coupling of the singlet and triplet spin states to the reservoir. Indeed, as the triplet spin states are composed of an excited orbital state with a greater spatial extent (c.f. Chap. 1), they are usually more coupled to the neighboring reservoirs than the singlet spin state (analogous to $1s/1p$ orbitals in atomic physics). This spin decays with a characteristic time $T_1 = 4\,\mathrm{ms}$ in the isolated regime, forcing us to wait at least $5T_1 = 20\,\mathrm{ms}$ to achieve a high-fidelity singlet initialization.

To fasten the initialization process, we load two electrons in a regime where the coupling to the reservoir is much greater than our voltage sweeping rate ($t_{\mathrm{res}} \gg 10\,\mathrm{MHz}$). As sketched Fig. 4.1.c, the energy separation between singlet and triplet spin states ensures that only the singlet spin state is available for a time much longer than the tunnel-in time, as the dot potential is lowered. By the time the quantum dot potential is low enough for a triplet spin state to be populated, two electrons in a singlet spin state already occupy the

quantum dot. This adiabatic singlet state loading provides a fast, high-fidelity initialization mechanism and only relies on our ability to control the coupling to the reservoir over several orders of magnitude.

Figure 4.1.b sums up these two initialization mechanisms. For intermediate reservoir coupling (position B), the singlet spin probability is initially rather low, and we need to let the spin decay over at least 15 ms. For high reservoir coupling (position A), the spin is immediately loaded in its ground state. In the following, we will quantitatively evaluate the achieved spin initialization fidelity.

4.1.2 Spin to charge conversion

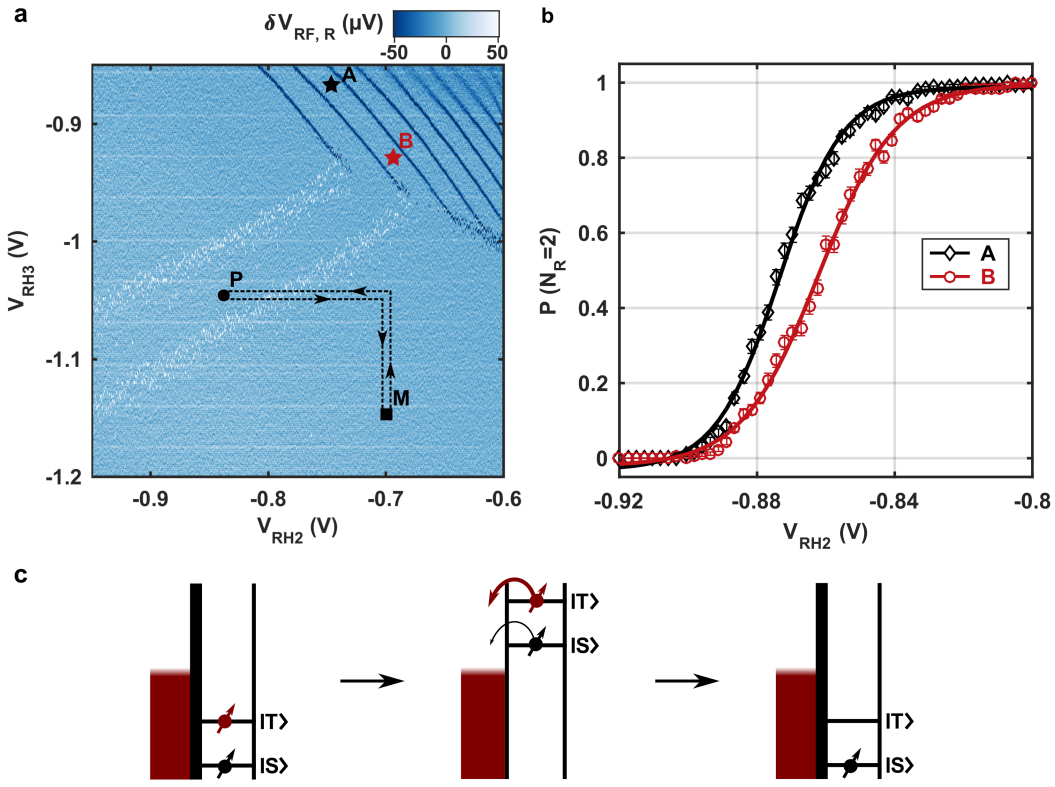

Figure 4.2: Spin-to-charge conversion. a.c. Scheme of the spin-to-charge conversion technique. The dot is pulsed for 16 µs to a configuration where the tunnel-out rate is ~ 1 MHz. A triplet state, being slightly more coupled to the reservoirs, will have a larger tunnel-out probability, leading to a charge difference when the system is brought back to M. **b.** Probability to keep two electrons for different P positions and the two initializations. At $V_{\mathrm{RH2}} = -0.865$ V, we observe a 30 % contrast between a mostly singlet or mostly triplet initialization, proving the spin selectivity.

As mentioned in the first chapter, direct spin measurement is impractical in our structures, as the associated magnetic dipole is extremely weak.[Rug04] Instead, we exploit a spin-to-charge conversion mechanism, and infer from the charge configuration the spin state. In our case, this mechanism again relies on a tunnel coupling difference to the reservoir. Because the triplet spin states are more strongly coupled, their typical tunnel-out time is

significantly lower than the singlet spin state, allowing us to discriminate between the two cases. However, all three triplet states having on first approximation the same tunnel-out rate, this mechanism does not allow us to distinguish them.

This tunnel-rate selective readout is usually performed in the intermediate reservoir coupling regime, to be able to time-resolve individual electron jumps to and from the reservoir. In our case, we exploited the isolated regime to construct a faster and more robust spin readout. It consists of increasing the reservoir coupling for $\tau = 16\,\mu s$, to a configuration where the a triplet spin state is associated to one electron tunnelling out, whereas for a singlet spin state the charge is preserved ($\Gamma_{|S\rangle} \ll \frac{1}{\tau} \ll \Gamma_{|T\rangle}$). The system is then brought back to the isolated regime, and a charge readout is performed. If only one electron is detected the measurement outcome is a triplet spin state, whereas an initial singlet spin state is associated with both electrons kept in the quantum dot.

The main advantage of this technique is that the tunnel-out time and the readout time are decoupled, as the charge configuration is frozen in the isolated regime. This allows us to increase the reservoir coupling for a duration shorter than our acquisition rate. In addition, because the system is always kept in a configuration where tunnelling-in of extra electrons is impossible, spin readout errors due to re-loading of a second electron are prevented.

To determine the optimal spin-to-charge conversion, we realize the experiment described Fig. 4.2. We load either mostly a singlet or mostly a triplet spin state (by using the two pre-determined loading positions A and B), and close the reservoir barrier (M), then pulse the system to a point P for $16\,\mu s$. Finally, we bring the system back to the M position and read-out the charge occupancy. Figure 4.2.b. presents the probability to keep two electrons in the quantum dot as a function of the position of P. We observe Fermi distributions for each state, a more negative V_{RH2} corresponding to a greater tunnel-out rate, and thus a lower probability for the two electrons to remain in the quantum dot. More importantly, we observe a contrast between the two spin initializations, a triplet spin state (loading position B) being always more likely to tunnel-out than a singlet spin state. We therefore chose $V_{RH2} = -0.865\,V$ as our spin-to-charge pulsing position. Immediately, we see that this spin to charge mapping is imperfect, as the contrast between the two curves in Fig. 4.2.b. is not unity. In other words, while a triplet spin state has always a greater tunnel-out probability than a singlet spin state, this difference is not large enough to provide a configuration where a singlet spin state will definitely not tunnel-out, and a triplet spin state definitely will. Later in this chapter, we will extract the fidelity of this spin readout and discuss data renormalization.

4.1.3 Spin mixing

Now that we can perform the initialization and readout of our spin state we can discuss its manipulation. As mentioned in the first chapter, the easiest knob we can use is to separate the two electrons in adjacent quantum dots for a controlled time. For example, if we load a singlet spin state into the reservoir dot (at position A in Fig. 4.1) and lower the detuning between this dot and the channel dot ($\varepsilon \approx V_{RH3} - V_{RH1}$), one electron will tunnel-out to the channel dot. Depending on the coupling (controlled by V_{RH2}) between these two dots, several regimes can appear:

- In the large coupling limit ($t_c \gg 10\,GHz$), the structure is effectively behaving as

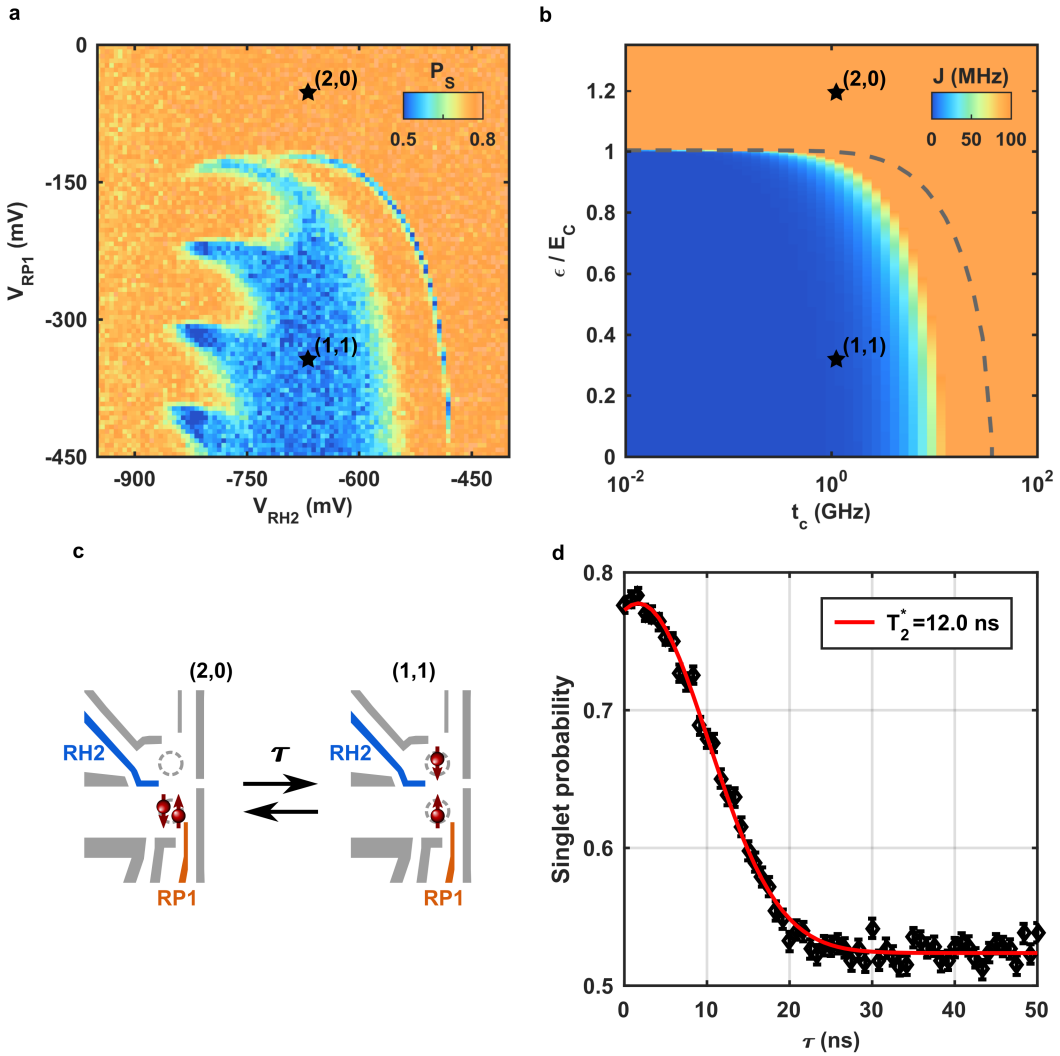

Figure 4.3: Spin mixing. a. Singlet spin probability after a 500 ns detuning pulse of amplitude V_{RP1} for different V_{RH2}. Each pixel is the average of 500 realizations, under an external magnetic field $B_z = 150\,\mathrm{mT}$. We can identify the S-T_0 mixing area as the central blue area, as well as the position of the S-T_+ avoided crossing (right curved line). In the extremely weak coupling regime ($RH2 < -700\,\mathrm{mV}$), the singlet state is preserved as tunnelling is prevented (see main text). **b.** Numerical simulation of the exchange energy $J = E_{\mathrm{T}_0} - E_{\mathrm{S}}$ as a function of the energy detuning ε and interdot coupling t_{c}. The calculated position of the S-T_+ avoided crossing is indicated by the gray dashed line. **c.** Mixing pulse scheme. The two spins are separated by a short detuning pulse on RP1, before being recombined in the channel quantum dot. **d.** Singlet spin probability as a function of the detuning pulse duration for the indicated point in the (1,1) configuration. The data is fitted with a Gaussian decay of characteristic time $T_2^* = 12.0 \pm 0.2\,\mathrm{ns}$.

one large single quantum dot. The dots are so strongly coupled that the singlet spin state remains an eigenstate of the system, and is unaffected by the detuning pulse.

- For intermediate coupling ($t_c = 100\,\text{MHz} - 10\,\text{GHz}$), in the (1,1) configuration the two spins will start to evolve separately according to their local Overhauser nuclear magnetic field, and when the electrons are brought back together in the (0,2) configuration their spin will not form a pure singlet state anymore.
- Finally, if the coupling is low compared to the duration of the detuning pulse ($t_c \ll 10\,\text{MHz}$), the (1,1) charge configurations cannot be reached and the electrons remain in a $|S_{(2,0)}\rangle$ state. In this regime, mixing can thus be prevented.

In order to confirm this ability to destroy the spin coherence, we therefore probe the probability to remain in a singlet spin state after a detuning pulse of 500 ns, while varying the interdot tunnel coupling over several orders of magnitude via the voltage applied on the interdot gate RH2. The obtained 2D plot, represented Fig.4.3 and later referred to as *spin map*, presents a complete spectroscopy of the mixing processes in an isolated double quantum dot.

Firstly, we indeed observe an area where the coherence is preserved regardless of the detuning, when the interdot coupling is the largest ($V_{RH2} > -480\,\text{mV}$). In this case, the interdot coupling is so strong that the singlet spin state remains the ground state regardless of the detuning. Secondly, for a smaller coupling ($V_{RH2} \approx -600\,\text{mV}$), spin mixing occurs in the (1,1) configuration and the singlet spin probability after recombination drops. Furthermore, we observe a line of lower singlet spin probability, attributed to the S-T_+ avoided crossing, and covered in details the next section. Finally, in the extremely weak coupling regime ($V_{RH2} < -700\,\text{mV}$), the singlet probability is preserved for $\varepsilon < E_c$. This corresponds to a regime where interdot tunnelling is prevented, forcing the electrons to remain in the singlet spin state. The lines where mixing does occur are attributed to resonances between the $|S_{(2,0)}\rangle$ state and excited (1,1) spin states. This phenomenon is exploited in App. C to estimate the coupling strength with these higher orbital states.

Figure 4.3.d. presents a measurement of the dynamics of the S-T_0 mixing process, where the singlet spin probability is plotted as a function of the detuning pulse duration. This measurement is fitted with a Gaussian decay of characteristic time $T_2^* = 12.0 \pm 0.2\,\text{ns}$. As explained in the first chapter, this number is characteristic of the number N of neighboring nuclear spins:

$$T_2^* = \frac{\hbar\sqrt{2}}{|g|\mu_B\sigma_{HF}} \propto \sqrt{N} \tag{4.1}$$

From the dephasing time T_2^* we can extract the width of the Overhauser magnetic field distribution, $\sigma_{HF} = 3.2 \pm 0.1\,\text{mT}$. This value is in good agreement with the expected number of neighboring nuclei $N \sim 10^6$.

In the following work, we use the high-coupling regime ($V_{RH2} = -400\,\text{mV}$) to transfer two electrons between the reservoir dot and the channel dot without affecting their spin state. Indeed, while the SAW-assisted shuttling involves the two channel dots, the spin initialization and readout both involve the reservoir dots on each side. Such a spin-preserving passage from (2,0) to (0,2) and back is therefore required on both double

quantum dots.

4.1.4 Spin funnel

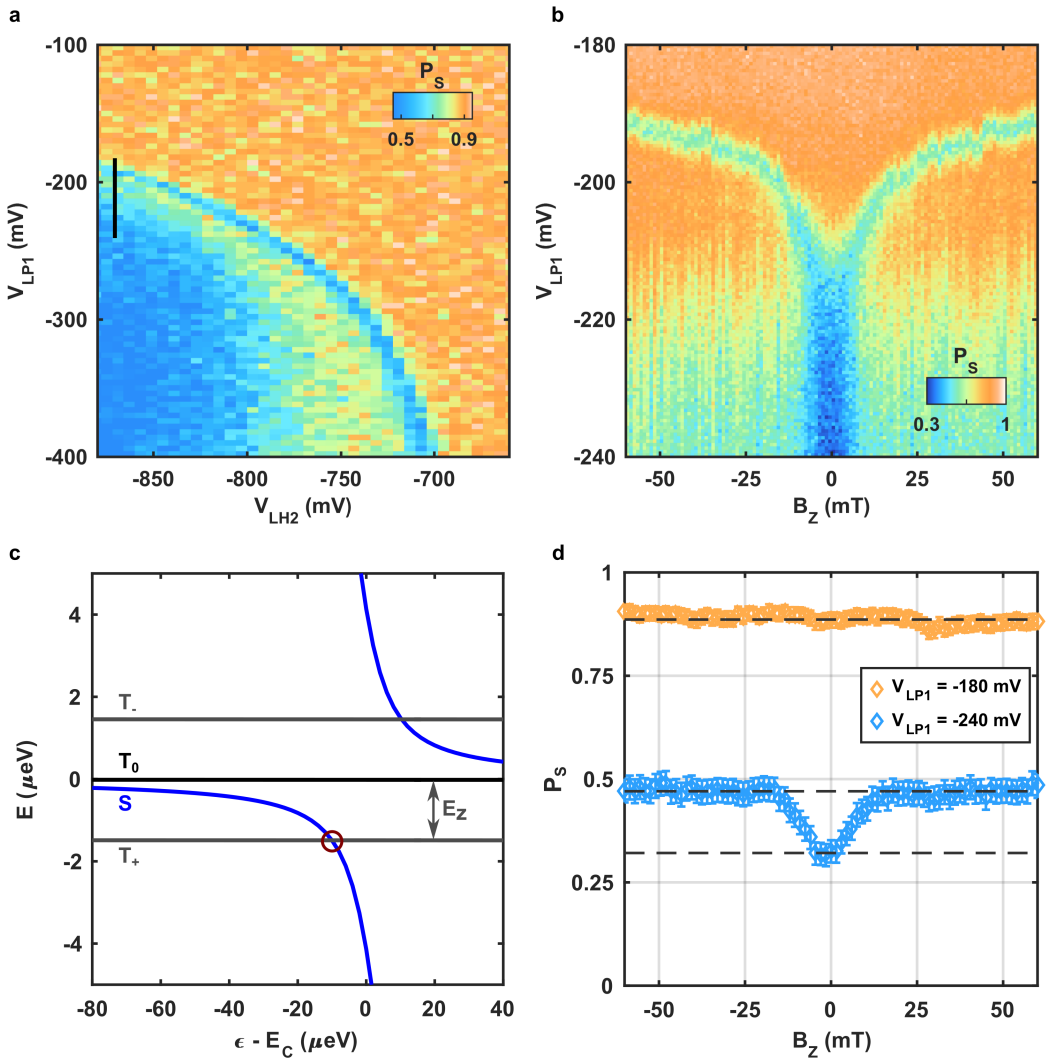

Figure 4.4: Spin funnel. a. Spin mixing map, similar to the previous figure but realized on the left double quantum dot under a smaller external magnetic field, $B_z = 60\,\mathrm{mT}$. **b.** Cut along the line indicated by the black line in **a.**, as the external magnetic field is varied. The observed funnel corresponds to the position of the S-T_+ avoided crossing for $B_z > 0$, and the S-T_- avoided crossing for $B_z < 0$. **c.** Sketch of the S-T_+ avoided-crossing position. As the external magnetic field is lowered, the energy of the T_+ state increases and its intersection with the singlet state shifts towards a lower energy detuning. **d.** Cut in **b.** for $V_{\mathrm{LP1}} = -180\,\mathrm{mV}$ and $V_{\mathrm{LP1}} = -240\,\mathrm{mV}$. From the three asymptotes (indicated by the gray dashed lines) we can infer the spin initialization and readout fidelities (see main text).

In the previous experiment, we see the signature of the S-T_+ avoided crossing as the curved line of lower singlet spin probability. Indeed, while the coupling between these

two spin states is rather weak (as it involves a spin flip), the x and y components of the Overhauser magnetic field or the spin-orbit coupling are able to couple $m_S = 0$ and $m_S = \pm 1$ spin states, and effectively create this small avoided-crossing. When the detuning is pulsed close to this position, these mixing mechanisms affect the singlet spin probability. For long pulses (500 ns), and averaging over many realizations, we therefore expect a statistical mixture of $50\,\%\ S - 50\,\%\ T_+$.

To verify that we indeed observe this mechanism, we exploit the non-zero magnetic moment of the T_+ and T_- states ($m_S = \pm 1$). By increasing the external magnetic field, we increase the Zeeman splitting of these states and shift the S-T_+ avoided-crossing towards higher detuning. This experiment, presented Fig. 4.4, is called a *spin funnel* measurement.

Experimentally, we measure the singlet spin probability as a function of the detuning ε and external magnetic field B_z, for a rather low interdot coupling $t_c \sim 1\,\mathrm{GHz}$. Contrary to the previous spin map Fig. 4.3, here the experiment is performed on the left double quantum dot, the detuning pulse being induced by a more negative voltage on LP1.

On top of the S-T_0 mixing (for $V_{\mathrm{LP1}} < -220\,\mathrm{mV}$) previously described, which remains unaffected by the magnetic field, we can clearly identify two lines of lower singlet spin probability forming a funnel shape. As indicated by the scheme Fig. 4.4c., this funnel shape reproduces very well the expected avoided-crossing position as the Zeeman splitting is varied. For a positive external magnetic field $B_z > 0$, the singlet spin state crosses the T_+ state, while for a $B_z < 0$ we see the crossing with the T_- state (we remind here that GaAs has a negative g-factor $g = -0.425$). For $B_z \approx 0$, the dominant energy scale in the (1,1) configuration is now the fluctuating Overhauser magnetic field provided by the surrounding nuclear spins. As a consequence, all four spin states can be considered degenerated, and the singlet spin probability is significantly lower than for simple S-T_0 mixing. The darker blue area in Fig. 4.4.b. gives us an idea of the necessary external magnetic field to lift the triplet spin states degeneracy, which is close to $|B_z| > 3\sigma_{\mathrm{HF}} = 10\,\mathrm{mT}$.

4.1.5 Initialization and readout fidelities

To calibrate the initialization and readout fidelities, we use the two line cuts presented Fig. 4.4.d. Here, two electrons are initialized in a singlet spin state and a 500 ns detuning pulse is applied. For the larger pulse (blue data points), the two electrons are separated and spin mixing occurs. For the smaller pulse (orange data points), the two electrons are kept together in the (2,0) configuration. We record the singlet spin probability as a function of the magnetic field for both pulses.

We call α the probability to measure a singlet spin state when the system is in a triplet spin state, β the probability to measure a triplet spin state instead of a singlet spin state, and γ the singlet spin initialization errors. When the two electrons are kept in the (2,0) configuration, the singlet spin probability is equal to:

$$P_{\mathrm{S}}^{a} = (1-\gamma)(1-\beta) + \gamma\alpha \tag{4.2}$$

However, when mixing in the (1,1) configuration occurs two cases need to be distinguished. For a large enough magnetic field $|B_z| \gg \sigma_{\mathrm{HF}}$, the degeneracy between the triplet spin states is lifted by the Zeeman energy, and mixing only occurs between the singlet and the

T_0 spin states. For a complete spin mixing, the output singlet spin probability is $\frac{1}{2}$. In the zero-magnetic field case $B_z = 0\,\mathrm{mT}$, mixing occurs with the T_+ and T_- as well and this expected singlet spin probability is $\frac{1}{3}$.[Mer02] Taking into account our error sources, we have:

$$\begin{aligned} P_S^b &= \left(\frac{1}{2} - \frac{\gamma}{3}\right)(1-\beta) + \left(\frac{1}{2} + \frac{\gamma}{3}\right)\alpha \quad \text{for } |B_Z| \gg 3\,\mathrm{mT} \\ P_S^c &= \frac{1-\beta}{3} + \frac{2\alpha}{3} \quad \text{for } B_Z \approx 0\,\mathrm{mT} \end{aligned} \tag{4.3}$$

From the data on Fig. 4.3.d. we extract these three values for the left double quantum dot (dashed gray lines). This allows us to determine the α, β and γ fidelities:

$$\begin{aligned} \alpha &= 0.02 \pm 0.05 \\ \beta &= 0.08 \pm 0.06 \\ \gamma &= 0.04 \pm 0.07 \end{aligned} \tag{4.4}$$

For the left side of the structure, we thus obtain a spin readout fidelity $\mathcal{F}_L = 1 - \frac{\alpha+\beta}{2} = 95 \pm 5\,\%$, and an initialization fidelity of $(1-\gamma) = 96 \pm 7\,\%$. For the right side of the structure, performing the same analysis we obtain a much smaller spin readout fidelity $\mathcal{F}_R = 75 \pm 5\,\%$ and a identical initialization fidelity.

This large difference in the spin-to-charge conversion fidelities for each side can lead to false interpretation when measurement on each side are compared, as well as an underestimation of the spin transfer fidelity. For these reasons, in the following results we sometimes present calibrated data (indicated by the *cal* label), where the spin-to-charge fidelity has been used to normalize the data as:

$$P_S^{cal} = \frac{P_S^{meas} - \alpha}{1 - \alpha - \beta} \tag{4.5}$$

Usually, the spin-to-charge conversion fidelities are re-evaluated for each side right before starting an important experiment, to monitor the sample slight evolution with time. In practice, we record a reference on both sides of the sample with and without a mixing pulse, and compute the new α and β coefficients for both sides of the structure.

4.2 Impact of the SAW modulation

The S-T_+ avoided crossing can also be exploited to measure the detuning modulation induced by the SAW potential as the wave passes through the double quantum dot. The sample was designed with a detuning axis orthogonal to the SAW wavefront, precisely in order to minimize this modulation. Indeed, in a previous version of this sample the spin transfer fidelity was greatly affected by a parasitic double quantum dot behavior, aligned with the SAW propagation axis.[Ber15a] The multiple passages through the S-T_+ avoided-crossing induced a spin mixing immediately before and after the actual electron sending.

To quantify this modulation, we perform the experiment described Fig. 4.5 in which a detuning pulse, identical to the one used in the previous section, is applied for 500 ns.

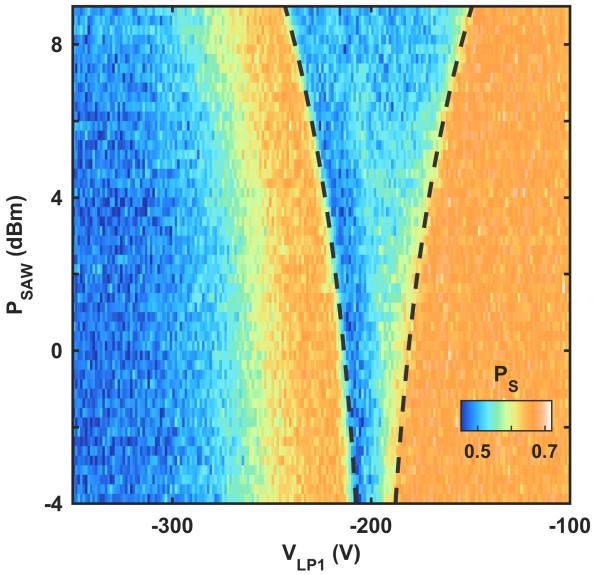

Figure 4.5: Impact of the SAW modulation. Singlet spin probability as a function of detuning when a SAW burst of increasing power is applied, for $B_z = 25\,\mathrm{mT}$. We observe a wider S-T_+ mixing area as a consequence of the detuning modulation by the SAW. This modulation amplitude scales as $17.0 \pm 1\,\mathrm{mV}/\sqrt{\mathrm{mW}}$, as indicated by the dashed lines.

However, we now synchronize this pulse with a 1 µs SAW burst, and we record the singlet spin probability as a function of the detuning and SAW power. We observe a widening of the S-T_+ mixing area, proportional to the SAW amplitude (square root of its power). We extract a coupling factor $\alpha_{\mathrm{SAW,\,LP1}} = 17.0 \pm 1\,\mathrm{mV}/\sqrt{\mathrm{mW}}$, giving for the maximum SAW power $P = 18\,\mathrm{dBm}$ an equivalent amplitude $\Delta V_{\mathrm{LP1}} = 135 \pm 7\,\mathrm{mV}$ on LP1.

This value gives us an idea of how far in detuning we need to keep the double quantum dot to prevent accidental mixing during the electron sending. Experimentally, we will often use a sending position deep in the (2,0) regime, separated from the position used in this double-dot regime by at least 400 mV on LP1. In addition, we point out here that the SAW modulation may also have an impact on the tunnel coupling t_c, to which the measurement presented Fig. 4.5. is insensitive. However, as we always keep our double-quantum dots in the (2,0) regime while the SAW is applied, this tunnel coupling modulation has no effect on the electron spin.

4.3 Exchange oscillations

In this section, we perform a two-qubit gate exploiting the the exchange interaction between two electron spins separated in adjacent quantum dots. Then, we demonstrate a delocalized spin measurement, shuttling the two electrons immediately after this coherent manipulation, and performing the spin readout on the left side of the structure. Finally, we discuss the spin transfer fidelity associated with the electron transfer protocol.

4.3.1 Landau-Zener criteria

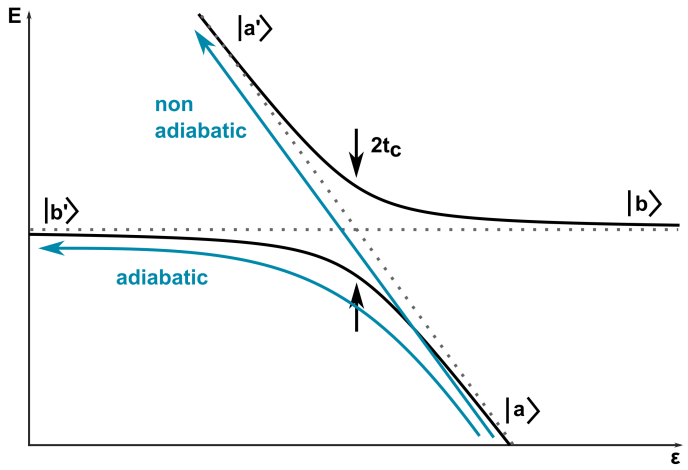

Figure 4.6: Landau-Zener criteria. Illustration of a adiabatic and non-adiabatic transition across an avoided crossing of coupling t_c. In the latter case, the detuning is ramped at a rate allowing the spin state to always remain in the ground state. In the former, the spin state can jump towards the excited level $|a'\rangle$.

As introduced in the first chapter, exchange oscillations rely on a non-adiabatic change of spin basis, leading to a phase accumulation between the $|\downarrow\uparrow\rangle$ and $|\uparrow\downarrow\rangle$ states. Since in our case the S-T_0 basis is required for spin readout and initialization, we also require a mapping from the $|\downarrow\uparrow\rangle$-$|\uparrow\downarrow\rangle$ basis to the $|S\rangle$-$|T_0\rangle$ basis, achieved in our case by an adiabatic detuning ramp. In this section, we introduce this adiabaticity criteria, often called the Landau-Zener criteria.

We consider an avoided crossing between two spin states $|a\rangle$ and $|b\rangle$ of coupling t_c, as represented Fig 4.6. The system is prepared in the state $|a\rangle$ and the detuning is ramped across the avoided crossing at a given rate. If this rate is larger than the coupling between the two spin states, the system will remain in its original spin state and end up in the upper branch $|a'\rangle$ (eventually followed by a relaxation process). However, if the detuning sweeping rate Γ is much smaller than the coupling t_c^2/h, the system will adiabatically follow the ground state of the system and end up in the lower branch $|b'\rangle$. Overall, the non-adiabatic passage probability is given by the Landau-Zener theory[Lan32; Zen32] as:

$$P_{|a\rangle\rightarrow|a'\rangle} = \exp\left(-\frac{2\pi t_c^2}{\hbar\Gamma}\right) \quad \text{with } \Gamma = \frac{dE}{dt} \tag{4.6}$$

Typically, for a coupling of $t_c/h = 1\,\text{GHz}$ this adiabaticity criteria imposes a detuning ramp across the avoided crossing for a duration on the order of several tenths of nanoseconds. In the following part, we exploit this technique to adiabatically transform a spin state or, on the contrary, to pass through an avoided-crossing without affecting the spin state.

4.3.2 Exchange oscillations

In absence of any artificial magnetic field gradient or ESR feedline, it is still possible to perform a two-qubit gate driven by the exchange interaction between two spins in adjacent dots. As the spin trajectory for this gate was already covered in the first chapter, we here focus on the experimental realization of this operation.

We consider the right double quantum dot, tuned to the low interdot coupling regime ($t_c \sim 1\,\mathrm{GHz}$). In this regime, when two antiparallel electrons are separated in the (1,1) configuration, the dominant energy scale is the Overhauser magnetic field difference ΔB_z created by the difference in local nuclear environment between the two quantum dots. The antiparallel spin eigenbasis is therefore $(|{\downarrow\uparrow}\rangle\ ;\ |{\uparrow\downarrow}\rangle)$, and we will suppose $\Delta B_z > 0$, making $|{\downarrow\uparrow}\rangle$ the antiparallel ground spin state. In the (2,0) configuration, the exchange interaction between the two spins is maximal and the eigenbasis is $(|S\rangle\ ;\ |T_0\rangle)$. As we can only initialize and measure a singlet spin state, the principle of the experiment is to establish a conversion mechanism to map $|S\rangle$ to $|{\downarrow\uparrow}\rangle$ (and $|T_0\rangle$ to $|{\uparrow\downarrow}\rangle$).

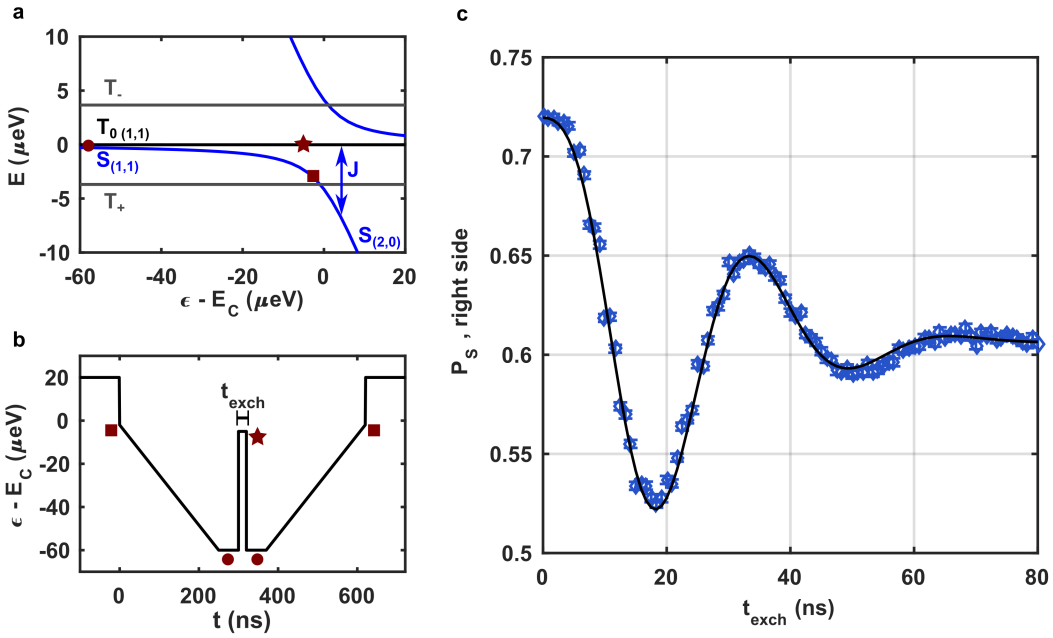

Figure 4.7: Exchange oscillations. a.b. Measurement scheme. The initial singlet spin state is converted to the $|{\downarrow\uparrow}\rangle$ state by an adiabatic detuning ramp towards the (1,1) configuration. The exchange interaction is turned on for t_{exch} by a detuning pulse, after which the system is brought back to the (1,1) configuration and another adiabatic ramp brings the spin state back to the (S,T_0) basis. **c.** Singlet spin probability as a function of the exchange pulse duration. The measurement is performed at $B_z = 150\,\mathrm{mT}$, each point being the average of 60000 single-shot realizations. We observe coherent oscillations of frequency $J = 29.1 \pm 0.2\,\mathrm{MHz}$ damped by a Gaussian decay of characteristic time $T_2^{\mathrm{Rabi}} = 35.7 \pm 0.8\,\mathrm{ns}$.

Figure 4.7.ab. presents the succession of detuning pulses and ramps applied to RP1, as well as a scheme of the different positions on the energy diagram. The sequence is as follows:

- A singlet spin state is initialized and the detuning is brought close to the (2,0)-(1,1) degeneracy line.

- A sub-ns detuning pulse is applied to pass the S-T_+ avoided crossing, assuring the singlet preservation. This pulse needs to be adiabatic with respect to the tunnel coupling, but non-adiabatic with respect to the S-T_+ coupling.

- The detuning is slowly ramped towards $\varepsilon = 0$, converting the $|S_{(2,0)}\rangle$ state to $|{\downarrow}{\uparrow}_{(1,1)}\rangle$. This ramp needs to be adiabatic with respect to both the interdot and hyperfine couplings.

- The exchange coupling is abruptly turned on by a detuning pulse bringing the system towards the (2,0) configuration, where the $|{\downarrow}{\uparrow}\rangle$ state is not an eigenvector anymore and starts evolving towards $|{\uparrow}{\downarrow}\rangle$ and back.

- After a given pulse duration t_{exch} the system is abruptly brought back to the (1,1) configuration, freezing the spin state into a superposition of $|{\downarrow}{\uparrow}_{(1,1)}\rangle$ and $|{\uparrow}{\downarrow}_{(1,1)}\rangle$.

- Another adiabatic detuning ramp is used to convert the $|{\downarrow}{\uparrow}_{(1,1)}\rangle$ and $|{\uparrow}{\downarrow}_{(1,1)}\rangle$ states to $|S_{(2,0)}\rangle$ and $|T_{0\,(2,0)}\rangle$ respectively. The S-T_+ crossing is again avoided by a sub-ns detuning pulse.

After this sequence, the probability to measure a singlet spin state oscillates with the exchange pulse duration as:

$$P_{\mathrm{S}} = \cos^2\left(\pi J\left(\varepsilon\right) t_{\mathrm{exch}}\right) \tag{4.7}$$

As developed in the first chapter, the main decoherence mechanism is usually the detuning noise, modulating the exchange interaction $J(\varepsilon)$ and giving rise to a dephasing time T_2^{Rabi}. Close to the avoided crossing $\varepsilon \approx E_{\mathrm{c}}$, the detuning noise has a linear dependence on the exchange energy:

$$\begin{aligned} J &\approx \frac{(\varepsilon - E_{\mathrm{c}}) + \sqrt{(\varepsilon - E_{\mathrm{c}})^2 + (2t_{\mathrm{c}})^2}}{2} \\ \text{and } \frac{\partial J}{\partial(\varepsilon - E_{\mathrm{c}})} &\propto \frac{J}{2t_{\mathrm{c}}} \end{aligned} \tag{4.8}$$

In consequence, the detuning noise has a stronger impact as J is increased, limiting the number of visible oscillations. This inter-dependence between Rabi frequency and dephasing time has been verified experimentally,[Ber15b] and sweet-spots have been exploited to overcome the impact of this detuning noise.

These coherent oscillations are visible Fig. 4.7.c., and are fitted with a frequency $J = 29.1 \pm 0.2\,\mathrm{MHz}$ and a dephasing time $T_2^{\mathrm{Rabi}} = 35.7 \pm 0.8\,\mathrm{ns}$. For $t_{\mathrm{exch}}^{\pi} = 18\,\mathrm{ns}$, the exchange pulse realizes a π pulse, transforming the $|{\downarrow}{\uparrow}\rangle$ state into the $|{\uparrow}{\downarrow}\rangle$ state and vice versa. This operation corresponds to a swap of of the two spins carried by each electron, called a SWAP gate. Using an exchange pulse half as long $t_{\mathrm{exch}}^{\pi/2} = 9\,\mathrm{ns}$, we realize a $\sqrt{\mathrm{SWAP}}$

gate, represented in the $(|\downarrow\downarrow\rangle\ ;\ |\downarrow\uparrow\rangle\ ;\ |\uparrow\downarrow\rangle\ ;\ |\uparrow\uparrow\rangle)$ basis by:

$$U_{\sqrt{\mathrm{SWAP}}} = \begin{pmatrix} 1 & 0 & 0 & 0 \\ 0 & \frac{1+i}{2} & \frac{1-i}{2} & 0 \\ 0 & \frac{1-i}{2} & \frac{1+i}{2} & 0 \\ 0 & 0 & 0 & 1 \end{pmatrix} \tag{4.9}$$

This quantum gate is universal, as any two-qubit gate can be obtained using the $\sqrt{\mathrm{SWAP}}$ and single-qubit gates. As such, it therefore has a particular importance in quantum computing and its demonstration in semiconductor spin qubits is relatively easy, only requiring a nanosecond control over the quantum dots electrostatic potential.

The rather poor contrast of the oscillations presented Fig. 4.7.c. ($A_{\mathrm{R}} = 22.6 \pm 0.4\,\%$) can be explained by several factors. First, taking into account the low spin-to-charge conversion fidelity for this particular experiment ($\mathcal{F}_{\mathrm{R}} = 77.2\,\%$), we obtain a more acceptable value $A_{\mathrm{R}}^{\mathrm{cal}} = 58.6 \pm 1\,\%$. Secondly, as stated before the detuning noise leads to an uncertainty in the Rabi frequency, which is the main decoherence mechanism. Finally, it can be challenging to fulfill all adiabaticity / non-adiabaticity conditions for the sequence (see above). For example, the position from which the adiabatic ramp starts (red square on Fig. 4.7.ab.) needs to be carefully chosen, in order not to be too close to the S-T_+ avoided crossing but still at a detuning where the splitting with the $|T_{0,(1,1)}\rangle$ spin state is large in order to avoid spin mixing.

4.3.3 Spin transfer

Now that we demonstrated the ability to manipulate a two-electron spin state using the right double quantum dot, we can try to perform a delocalized spin measurement using the SAW-assisted electron shuttling presented in the previous chapter. The principle of this experiment is to load two electrons forming a singlet spin state on the right of the structure, and empty the left side.

We then perform exchange oscillations identical to those presented Fig. 4.7. However, instead of measuring the singlet spin probability on the right side, we generate a SAW burst and shuttle the two electrons towards the left side of the structure, tuned in the single dot regime. The electrons are caught and spin-to-charge conversion is performed, in order to measure the singlet spin probability oscillations with the exchange pulse duration t_{exch} applied on the right side before sending. We remove from the data analysis the few single-shot realizations where the charge transfer was unsuccessful (6 %), which would alter the spin probability.

The singlet spin probability measured after transfer is represented Fig. 4.8. We observe oscillations identical in frequency and dephasing time as those presented Fig. 4.7. ($J = 29.2 \pm 0.2\,\mathrm{MHz}$, $T_2^{\mathrm{Rabi}} = 34.4 \pm 0.8\,\mathrm{ns}$), proving the effectiveness of this delocalized spin measurement. However, these oscillations present a much lower contrast ($A_{\mathrm{L}} = 9.3 \pm 0.2\,\%$) than the right side measurement presented Fig. 4.7., even when the different spin-to-charge

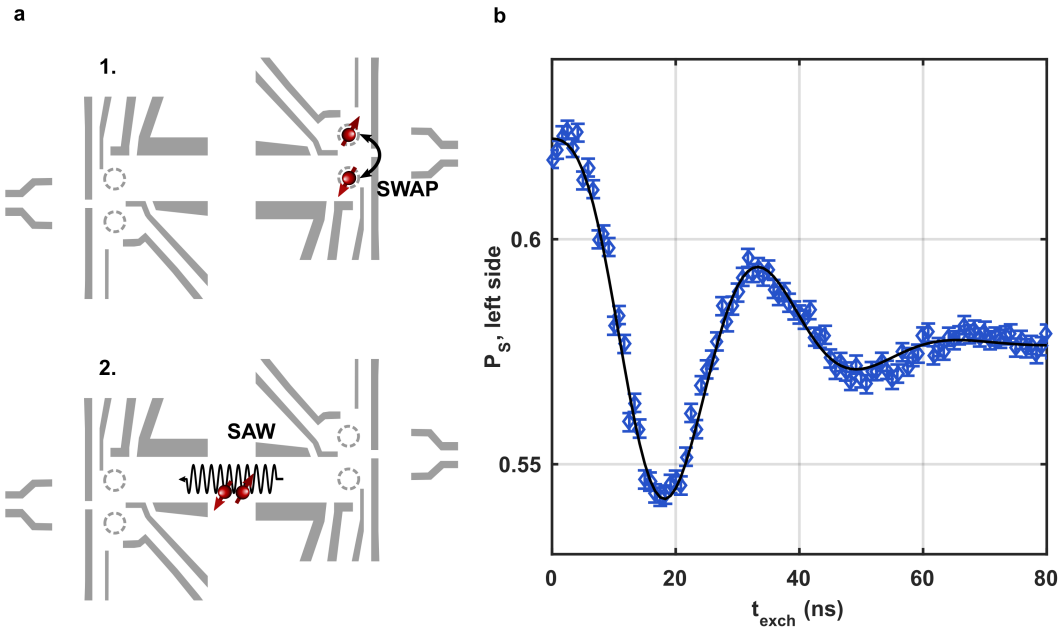

Figure 4.8: Spin transfer after manipulation. a. Measurement scheme. A singlet spin state is initialized on the right side of the structure, and an exchange identical to the one presented in the previous figure is performed. The system is then pulsed to the transfer configuration, and a SAW burst is applied to shuttle both electrons to the left side of the structure. There, spin-to-charge conversion is performed in order to measure the singlet spin probability. **b.** Singlet spin probability as a function of the exchange pulse duration. The measurement is again performed at $B_z = 150\,\mathrm{mT}$, each point being the average of 60000 single-shot realizations. The oscillations are fitted with a cosine of frequency $J = 29.2 \pm 0.2\,\mathrm{MHz}$ damped by a Gaussian decay of characteristic time $T_2^{\mathrm{Rabi}} = 34.4 \pm 0.8\,\mathrm{ns}$.

conversion fidelities on each side are taken into account:

$$\begin{aligned} A_{\mathrm{L}}^{\mathrm{cal}} &= \frac{A_{\mathrm{L}}}{2(\mathcal{F}_{\mathrm{L}} - 0.5)} = \frac{0.093}{0.258} = 0.360 \pm 0.008 \\ A_{\mathrm{R}}^{\mathrm{cal}} &= \frac{A_{\mathrm{R}}}{2(\mathcal{F}_{\mathrm{R}} - 0.5)} = \frac{0.226}{0.386} = 0.586 \pm 0.01 \end{aligned} \tag{4.10}$$

The ratio of these two contrasts gives a first idea of the spin transfer fidelity, which is $\frac{1+A_{\mathrm{L}}^{\mathrm{cal}}/A_{\mathrm{R}}^{\mathrm{cal}}}{2} = 81 \pm 1\,\%$ (see [Ber16a] Suppl. III for the definition of the transfer fidelity). We remind the reader that this number takes into account errors in the sending procedure and the respective spin readout fidelities on both sides of the nanostructure. This experiment proves our ability to manipulate a spin state and preserve it during the shuttling of the electrons themselves. However, the fidelity of this process is quite low, greatly limiting possible applications. It appear therefore important to identify the mechanisms responsible for the observed loss of coherence, and evaluate our ability to prevent them.

Origin of the decoherence

As introduced in the first pages of this thesis, the main requirement to achieve coherent transport of a singlet-triplet qubit is to keep the two electrons, support of the quantum information, together as much as possible. Indeed, no single-spin operation applied simultaneously to both electrons can affect the singlet spin state. Here, we try as much as possible to send the two electrons together, using the triggered sending technique presented in the previous chapter. However, because of the combined action of Coulomb repulsion and rising time of the sending voltage pulse, it is unlikely for two electrons to travel in the exact same SAW minimum. In this experiment however, we estimate that the two electrons are always injected at least 2.1 ns apart, which is the duration of the voltage pulse.

The first decoherence mechanism we can consider is the hyperfine interaction with the surrounding nuclear spins. However, due to an extreme motional narrowing effect,[Fle17] an electron spin in motion should not decohere due to this effect. Thus, decoherence due to hyperfine interaction can only occur when one electron is in motion and the other is not, which, as mentioned in the previous paragraph, corresponds to an extremely short time (under 2.1 ns). Therefore, the hyperfine interaction alone cannot explain the observed loss of contrast between Fig. 4.7 and Fig. 4.8.

In addition, we observe that the singlet preservation fidelity decreases as we move to higher external magnetic fields (see App. D.). This observation point towards an additional decoherence mechanism, involving electrical noise during the transport, and investigated by Huang *et al*[Hua13] specifically in the case of SAW-induced transport. This mechanism is based on a stochastic path followed by an electron in motion, affected by electrical noise in its confining potential (in our case both the SAW and channel gates). Its predicted effect, detailed in App. D, reproduces quite well the observed dependency of the singlet preservation fidelity as a function of the external magnetic field.

In conclusion, the contrast reduction observed in Fig. 4.8 compared to the reference in Fig. 4.7 can be explained by decoherence mechanisms affecting the electron spin during its motion. In particular, hyperfine interaction dominates the decoherence process for a static electron. For a moving electron spin, the electrical noise affecting its path has been identified as the main decoherence mechanism. However, we remind the reader here that both of these contributions would have no effect on a singlet spin state if the two electrons were transported in the same moving quantum dot. In our experiment, the limited SAW amplitude and the rise time of the sending voltage pulse limit our ability to fulfill this requirement, but a high-fidelity single electron injection in a specific SAW minimum has already been reported.[Tak19] Providing a sufficient SAW confinement, the high-fidelity simultaneous transfer of two electrons should be achievable.

4.4 Conclusion

In this chapter, we presented the techniques used to initialize a singlet spin state, and read out the singlet spin probability. While both of these techniques require an electron reservoir, our ability to tune the coupling to this reservoir over many orders orders of magnitude allows us to implement faster schemes for both of these steps. The singlet spin state adiabatic loading, for example, guarantees a high-fidelity initialization, two orders

of magnitude faster than a relaxation-based initialization. Using the isolated regime, the spin-to-charge conversion can be decoupled from the actual charge readout, allowing us to minimize the re-loading errors and setting the charge measurement bandwidth as the measurement speed bottleneck.

Using nanosecond detuning pulses, we investigated the spectroscopy of a double quantum dot and the different mixing processes, for a wide range of interdot tunnel coupling. Exploiting the magnetic field dependence of the $m_S = \pm 1$ spin states T_+ and T_-, we presented a spin funnel experiment and extracted from it the spin initialization and readout fidelities for both sides of the structure. The S-T_+ avoided crossing also allowed us to estimate the detuning modulation induced by the SAW, and to determine how far in the (2,0) configuration the system needs to be kept in order not to experience unwanted spin mixing.

Finally, we exploited the exchange interaction between two neighbor electron spins to realize local two-spin oscillations, using only our ability to control the energy detuning with nanosecond voltage pulses. As a first demonstration of the spin-preserving nature of the electron shuttling procedure, we performed a delocalized singlet spin probability measurement, transferring both electrons to the left side of the structure to read out their spin state. From these last two experiments, we extract a spin transfer fidelity of $81 \pm 1\,\%$, and discuss the mechanisms responsible for the observed decoherence during the transport. In particular, the role of the spin-orbit coupling when the two electrons are sent with a small delay will be investigated in the next chapter.

CHAPTER 5

Coherent single-spin shuttling and remote entanglement

In the previous chapter, we have identified the sending delay uncertainty as imperative to explain the decoherence observed during the singlet spin transfer procedure. To try to quantify this effect, we exploit the delay-controlled sending procedure established in Chap. 3 to sequentially transfer two electrons initially forming a singlet spin state. After transfer, we use the spin-to-charge conversion on the left reservoir dot to measure the probability to obtain a singlet spin state, for several separation times. In opposition with the non-local spin readout presented before, the absence of manipulation in the static double dots allows us to explore the spin preservation fidelity at low applied magnetic fields.

Measuring the singlet spin probability after transfer as a function of the sending delay and the external magnetic field, we observe an interference pattern, signature of the coherence of the single-spin transport. We demonstrate that these oscillations are the result of coherent single-spin rotations, driven by the spin-orbit coupling during the electron propagation, and Larmor precession under the external magnetic field when the electron is static.

We show that this transfer procedure can be interpreted as a Bell measurement, able to prove and quantify the entanglement between the two electron spins. From the oscillation contrast, we demonstrate that these spins remain entangled even when separated by 6 µm, asserting the SAW-induced shuttling as a reliable technique to create distant entangled electrons. Finally, we exploit our ability to destroy spin coherence using spin mixing in a double quantum dot to quantify some of the density matrix elements of the initial state.

5.1 Two-electron spin quantum interferences

5.1.1 At zero external magnetic field

As introduced in the previous chapter, a singlet spin state should always be preserved if both electron spins experience the same evolution at all time, i.e. if they are shuttled together. Contrarily, if the two electrons are sent with a delay larger than the typical decoherence time ($\sim 10\,\mathrm{ns}$), mixing processes (e.g. difference of Overhauser magnetic field on each side of the channel) lower the final singlet probability after recombination. We thus begin with the study of the singlet preservation fidelity for $B_z = 0\,\mathrm{mT}$ and $\Delta t = 0 - 70\,\mathrm{ns}$.

In order to remove the few occurrences (3.2 % for this experiment) where one electron is not transferred, either because it stayed on the right double quantum dot or because

it was not caught in the left one, we actually measure the charge twice: before and after spin-to-charge conversion. The first measurement is used to check that we indeed received two electrons, while the second determines the spin projection. As this charge measurement is performed in the isolated regime, it does not affect the electron spin. In addition, the singlet spin probability presented in the following measurements is re-normalized using the spin-to-charge conversion fidelity for the left side $\mathcal{F}_{\mathrm{L}} = 95.3\,\%$, according to the procedure described in section 4.1.5.

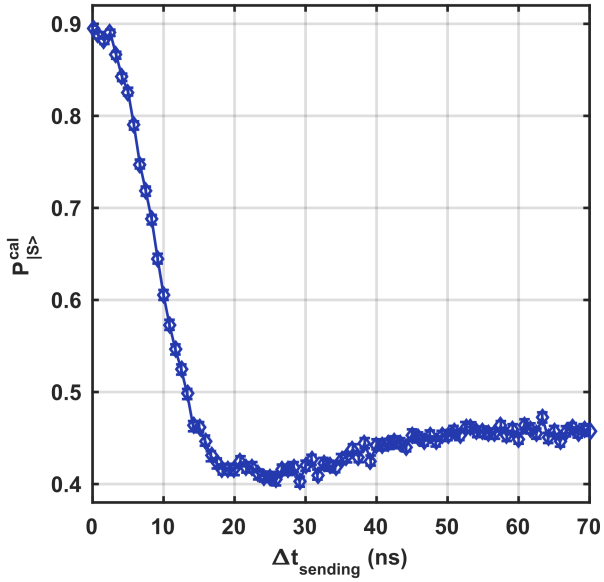

Figure 5.1: Coherent transfer at zero magnetic field. Singlet spin probability after transfer at zero external magnetic field, as a function of the sending delay between the two electrons. Each pixel corresponds to 10000 single-shot realizations. As the electrons are separated for a longer duration, we observe decoherence of the initial singlet spin state they formed, analogous to the spin mixing processes in adjacent double quantum dots.

Figure 5.1. presents the output of such an experiment at zero external magnetic field $B_z = 0$. As expected, we observe the signature of a spin mixing process for large sending delays, when the electrons are separated for too long. The singlet spin probability decays with a characteristic time $T_2 = 9.2 \pm 0.2\,\mathrm{ns}$, extracted from the width at half maximum. This dephasing time is comparable to the coherence times measured at zero magnetic field for adjacent quantum dots, indicating a predominant contribution of the hyperfine coupling at $B_z = 0\,\mathrm{mT}$.

We obtain a singlet preservation fidelity of $89.5 \pm 0.3\,\%$ for the minimum achievable separation time. We remind the reader that, even at $\Delta t = 0\,\mathrm{ns}$ the two electrons are shuttled in different moving quantum dots, due to the combined effect of the rise time of the sending voltage pulse and the charging energy of the sending dot. In addition, the Coulomb repulsion inside the moving dot itself may contribute to an additional reduction of the probability to inject both electrons in the same moving dot. As mentioned in the third chapter, we expect a minimum delay between the two electrons of 0.7 ns. Added

up to the SAW travel time across the channel, this means that the electrons are at least separated by 2.8 ns. In this condition, we nevertheless obtain a high singlet probability after recombination, proving that the the coherence of the initial spin state has been preserved throughout the electron separation. This measurement is thus a demonstration of the coherence-preserving nature of the transfer procedure at zero magnetic field.

5.1.2 Non-zero external magnetic field

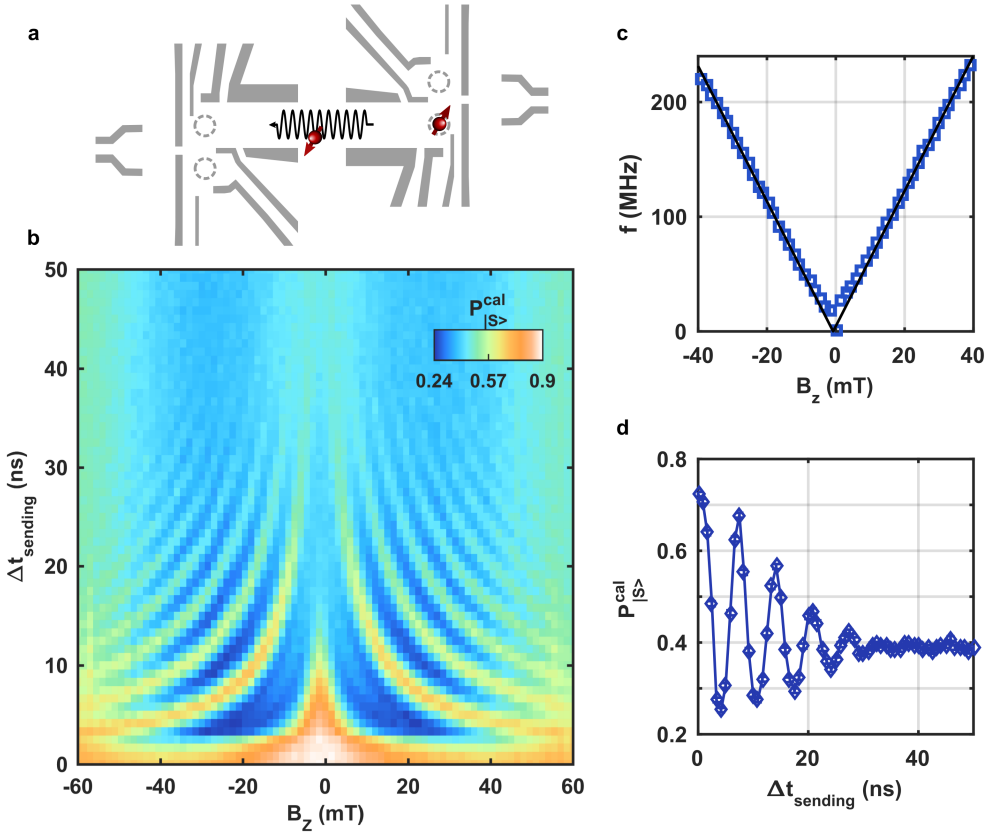

Figure 5.2: Non-local two-electron spin quantum interferences. a. Spin transfer scheme. Two electrons, initially in a singlet spin state, are sequentially shuttled across the channel by a propagating surface acoustic wave. **b.** Singlet spin probability after transfer as a function of the sending delay and the external magnetic field. Each pixel corresponds to 10000 single-shot realization, the charge transfer errors ($\approx 3\,\%$) being removed from the spin measurement. We observe a high-contrast interference pattern, signature of coherent single-spin rotations driven by the electron motion via spin-orbit coupling. The singlet spin probability has been calibrated using the previously extracted spin-to-charge conversion fidelity on the left side of the structure. **c.** Oscillation frequency extracted from **b.**, showing a linear dependance with the external magnetic field. From this measurement we extract a electron g-factor of $g = -0.42 \pm 0.01$. **d.** Cut in **b.** for $B_z = 22.5\,\mathrm{mT}$. We obtain a minimum singlet probability of 0.249 ± 0.005 for $\Delta t_{\mathrm{sending}} = 4.16\,\mathrm{ns}$.

Repeating the previous experiment for a non-zero magnetic field, we see the emergence

of an interference pattern represented Fig. 5.2. We can identify high contrast oscillations in the singlet spin probability after transfer, whose frequency appear proportional to the applied magnetic field, as indicated in Fig. 5.2.b. From this linear dependance, we extract the electron g-factor:

$$\omega = \frac{|g|\mu_{\mathrm{B}} B_z}{\hbar} \text{ with } g = -0.42 \pm 0.01 \tag{5.1}$$

For $|B_z| < 22.5\,\mathrm{mT}$, we observe a doubling of this frequency. The maximum oscillation contrast ($52.2 \pm 0.4\,\%$), is obtained around $B_z = \pm 22.5\,\mathrm{mT}$. This large contrast points at a highly coherent single-spin rotation during the transfer, which we will link in the following section to the spin-orbit interaction affecting each spin propagating at the speed of sound through the channel.

The coherent oscillations presented Fig. 5.2. are characterized by a progressive loss of contrast both in magnetic field and sending delay. In the next section, we establish a numerical model in order to identify the main sources of decoherence explaining this phenomenon. As we will see, the decoherence towards large $\Delta t_{\mathrm{sending}}$ is mainly due to the difference of hyperfine interaction between the two ends of the channel, during the phase where both electrons are static and separated. On the contrary, the observed decoherence for a minimum electron separation time $\Delta t_{\mathrm{sending}} = 0\,\mathrm{ns}$ involves necessarily a decoherence process during the electron propagation, which we attribute to the inhomogeneities of electrostatic potential along the path of the electrons.

5.2 Role of the spin-orbit coupling

5.2.1 Single-spin rotation

In order to explain the interference pattern obtained Fig. 5.2., we need to consider the impact of the spin-orbit coupling during each electron transfer, under a given external magnetic field B_z. During its journey across the channel, each electron is confined by the SAW and travels at a constant velocity $v_{\mathrm{SAW}} = 2.79\,\mu\mathrm{m/ns}$, corresponding to a time of flight of $t_{\mathrm{S}} = 2.1\,\mathrm{ns}$. The spin-orbit interaction felt by the electron can be treated as an in-plane magnetic field $\boldsymbol{B}_{\mathrm{SO}}$, whose magnitude and orientation depends on the electron momentum $\boldsymbol{p}$. As introduced before, for a propagation along [110] or [$\bar{1}$10] axis, this effective magnetic field is perpendicular to the direction of motion. We will therefore consider a motion along $\boldsymbol{u_y}$, and a single-spin Hamiltonian :

$$\mathrm{H}_{\boldsymbol{p}\neq\boldsymbol{0}} = \mathrm{H_Z} + \mathrm{H_{SO}} = \frac{g\mu_{\mathrm{B}}}{2}\left(B_z\sigma_z + B_{\mathrm{SO}}\sigma_x\right) \tag{5.2}$$

Applied for a duration t_{S}, this Hamiltonian leads to the unitary evolution

$$\begin{aligned} \mathrm{U} &= \exp\left(-\frac{i\mathrm{H}_{\boldsymbol{p}\neq\boldsymbol{0}} t_{\mathrm{s}}}{\hbar}\right) \\ &= \cos\left(\frac{\omega_{\mathrm{tot}} t_{\mathrm{s}}}{2}\right)\mathrm{I}_2 - i\left[\frac{\omega_{\mathrm{SO}}}{\omega_{\mathrm{tot}}}\sigma_x + \frac{\omega_z}{\omega_{\mathrm{tot}}}\sigma_z\right]\sin\left(\frac{\omega_{\mathrm{tot}} t_{\mathrm{s}}}{2}\right) \\ &\text{with } \omega_{\mathrm{tot}} = \sqrt{\omega_{\mathrm{SO}}^2 + \omega_z^2} = \frac{g\mu_{\mathrm{B}}}{\hbar}\sqrt{B_{\mathrm{SO}}^2 + B_z^2} \end{aligned} \tag{5.3}$$

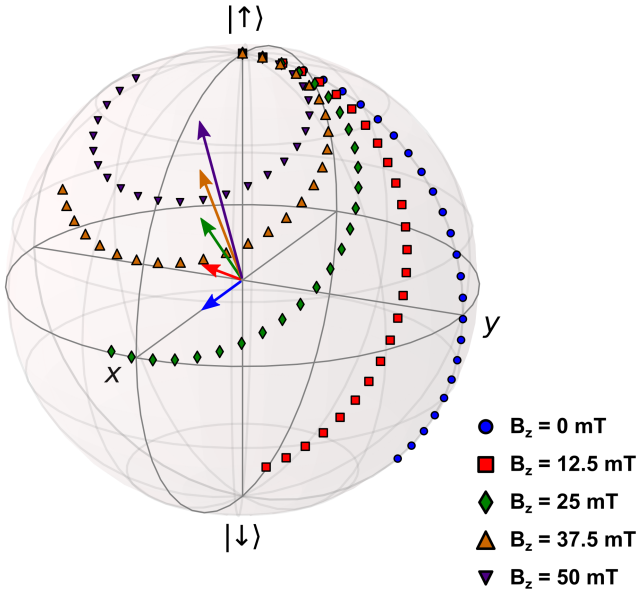

Figure 5.3: Single-spin trajectories. Single-spin rotation experienced by an electron spin initially in the $|\uparrow\rangle$ state during its transfer across the channel, for different external magnetic fields. For $B_z = 0\,\mathrm{mT}$, the spin-coupling drives a 0.7 ß rotation around the $\boldsymbol{u_x}$ axis. As the magnetic field is increased, the rotation axis has a stronger $\boldsymbol{u_z}$ component and the trajectory remains closer to the initial state. For a specific magnetic field $B_z \approx 25\,\mathrm{mT}$, the rotation maps the $|\uparrow\rangle$ and $|\downarrow\rangle$ to opposite points of the Bloch sphere equator. In this case, the unitary transformation endured by the electron spin is close to an Hadamard gate.

This unitary evolution is actually a rotation by an angle $\theta = \omega_{\mathrm{tot}} t_{\mathrm{S}}$ around the axis $\boldsymbol{u} = [B_{\mathrm{SO}},0,B_z]/B_{\mathrm{tot}}$, as represented Fig. 5.3. For $B_z = 0\,\mathrm{mT}$, this is equivalent to a simple rotation around $\boldsymbol{u_x}$, by an angle only determined by the channel length:

$$\theta_{\mathrm{SO}} = \omega_{\mathrm{SO}} t_{\mathrm{S}} = \frac{\pi v_{\mathrm{SAW}}}{l_{\mathrm{SO}}} t_{\mathrm{S}} = \frac{l}{l_{\mathrm{SO}}}\pi \tag{5.4}$$

with l_{SO} is the spin-orbit length, for which a propagating spin experiences a π pulse. This characteristic length is anisotropic and has been measured in GaAs by several methods. Using Kerr microscopy, Sanada *et al*[San11] extract $l_{\mathrm{SO}}^{[110]} = 10.9 \pm 0.1\,\mu\mathrm{m}$ and $l_{\mathrm{SO}}^{[\bar{1}10]} = 8.5 \pm 0.1\,\mu\mathrm{m}$. Since our channel is 6 µm long and oriented along the $[\bar{1}10]$ axis, we expect:

$$\theta_{\mathrm{SO}} = \frac{l}{l_{\mathrm{SO}}}\pi = 0.70\pi \pm 0.02\pi \tag{5.5}$$

As the external magnetic field $|B_z|$ increases, the rotation axis $\boldsymbol{u}$ tilts towards $\boldsymbol{u_z}$, leading to a phase accumulation and a smaller latitude amplitude on the Bloch sphere (Fig. 5.3). It can be demonstrated (see App. A.) that there exists a magnetic field for which the rotation maps the poles to opposite points on the equator. At this particular magnetic field ($B_z \approx 25\,\mathrm{mT}$ for our θ_{SO}), U is equivalent to an Hadamard gate with an additional

phase accumulation, represented in the $(|\downarrow\rangle\ ;\ |\uparrow\rangle)$ basis by:

$$\mathrm{U}_0 = \frac{1}{\sqrt{2}} \begin{pmatrix} e^{i\phi_0} & 1 \\ 1 & -e^{-i\phi_0} \end{pmatrix} \tag{5.6}$$

5.2.2 Decoherence during transfer

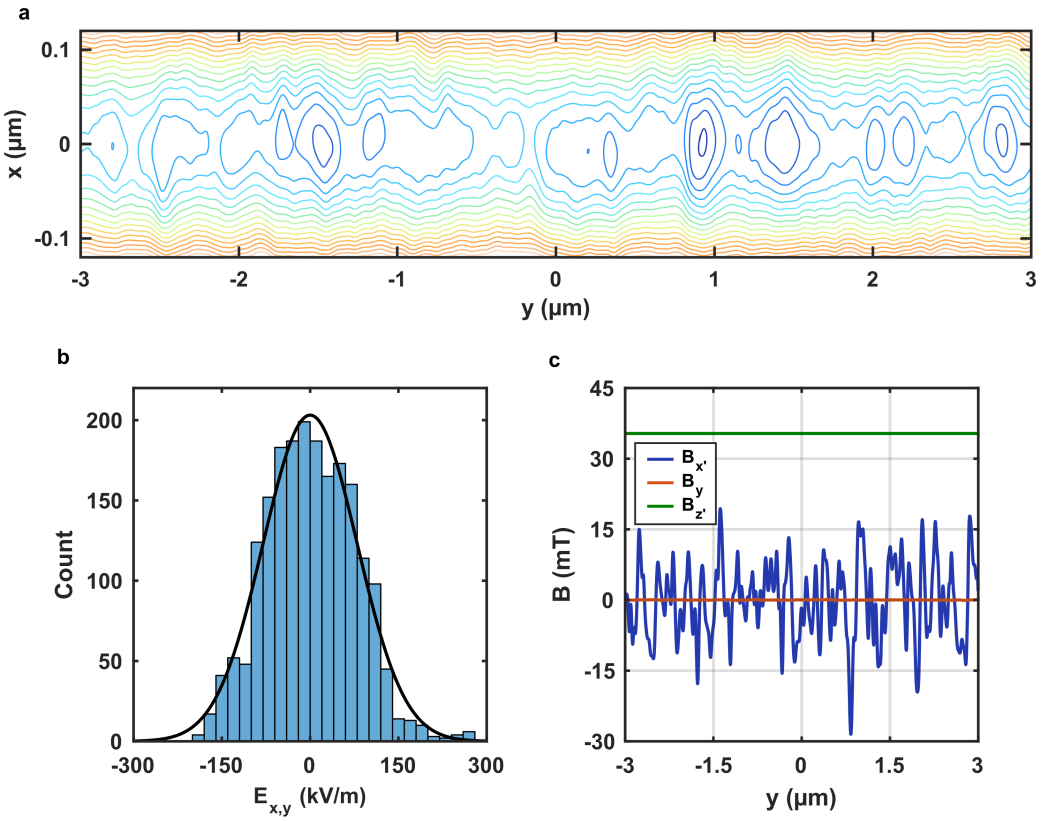

Figure 5.4: Effect of the potential inhomogeneities. a. Simulation of the channel electrostatic potential. On top of the parabolic confinement given by the metallic gates (along x), the ionized Si dopants in the heterostructure lead to potential fluctuations with a typical scale of 100 nm. The iso-potential contours are 8 mV apart. **b.** Histogram of the potential gradient along the $x = 0\,\mu$m line. The distribution is fitted with a Gaussian curve of standard deviation $\sigma_E = 110\,$kV/m. **c.** Equivalent magnetic field experienced by an electron propagating at $v = 2.79\,\mu$m/ns under an external magnetic field $B_z = B_{\mathrm{SO}} = 25\,$mT (with $x\prime$ and $z\prime$ defined in the main text).

In our GaAs/AlGaAs heterostructure, the electrons forming the 2DEG come from the Si-doped layer, 25 nm to 100 nm above it. Therefore, we expect a positive charge density in this layer at least equal to the 2DEG electron density, $n_e = 2.6 \times 10^{11}\,\mathrm{cm}^{-2}$. In addition, a significant portion ($\sim 10\,\%$) of electrons coming from the donors are located at the top interface of the substrate. Because the location of these ionized Si atoms is random,

they add a spatially fluctuating electrostatic potential to the confinement imposed by the channel gates. In the numerical simulation visible in Fig. 5.4.ab., we can see that these inhomogeneities have a typical scale of the order of 100 nm, with typical potential gradients around $\sigma_E = 110\,\mathrm{kV/m}$. These values are in good agreement with the literature[Hua13; Nix90].

From the perspective an electron travelling at the speed of sound $v = 2.79\,\mu\mathrm{m/ns}$ across the channel, this spatially fluctuating electric field corresponds to a magnetic field fluctuating in time, as developed by Huang *et al*[Hua13]. In their model, these fluctuations are of the form:

$$\boldsymbol{\delta B} = 2\boldsymbol{B} \times \boldsymbol{\Omega}$$
$$\text{with } \boldsymbol{\Omega} = \frac{-1}{m^*} \begin{pmatrix} \frac{1}{\omega_y^2 l_{\mathrm{SO}}^y} \frac{\partial V}{\partial y}(r_0) \\ \frac{1}{\omega_{x\prime}^2 l_{\mathrm{SO}}^{x\prime}} \frac{\partial V}{\partial x\prime}(r_0) \\ 0 \end{pmatrix} \tag{5.7}$$

where $z\prime$ is the direction of the total magnetic field $\boldsymbol{B} = \boldsymbol{B_z} + \boldsymbol{B}_{\mathrm{SO}}$. Intuitively, the potential gradient along the direction of propagation y creates a fluctuating magnetic field $\delta B_{x\prime}$ orthogonal to both the total magnetic field $\boldsymbol{B}$ and the direction of propagation. The magnitude of $\delta B_{x\prime}$ depends on the ratio of potential gradient $\frac{\partial V}{\partial y}$ to the confinement $\hbar\omega_y = 0.3\,\mathrm{meV}$, and is inversely proportional to the spin-orbit length l_{SO}^y. Similarly, a fluctuating magnetic field colinear to the electron motion δB_y is created by the lateral motion of the electron. However, as the confinement along the x direction is much larger than the one provided by the SAW ($\hbar\omega_x = 4\,\mathrm{meV}$), the amplitude of δB_y is much lower than the one of $\delta B_{x\prime}$.

This effect is visible in Fig. 5.4.c., where the three components of the magnetic field applied on the propagating electrons are plotted throughout the transfer. For $B_z = B_{\mathrm{SO}} = 25\,\mathrm{mT}$, the potential fluctuations along the electron path driven mainly a fluctuating magnetic field along $x\prime$. However, this spatially-fluctuating magnetic field alone cannot explain the decoherence observed in the experimental data, but fluctuations in time also need to be considered. This is not surprising if we consider the energy of the SAW, perturbing the heterostructure and changing the ionization of the Si atoms in the doped layer.

In the simulation presented in the next section, we separate the channel into sections of 100 nm, which we find to be the typical correlation length of the potential inhomogeneities. We then generate for each section a random electric field, following a normal distribution of standard deviation $\sigma_E = 110\,\mathrm{kV/m}$. We compute the effect of the noisy drive on the single-spin rotation U over the total channel length. We find that the best fitting parameter for the observed decoherence in the system is a SAW-induced confinement of $\hbar w_y = 300\,\mu\mathrm{eV}$, which is in good agreement with an independent SAW amplitude estimation for the same input power (see Fig. 4.5). In addition, we observe that the large decoherence observed at high magnetic field and small delay can only be explained if we consider a different path for each electron explained mostly by the SAW perturbation ionizing different dopants and perhaps also due to the Coulomb repulsion during the motion. Thus, we generate a

different set of δB for each electron transfer.

5.2.3 Sequential sending

In the experiment presented in Fig. 5.2., the two electrons are initially in a singlet spin state $|\mathrm{S}\rangle = \frac{1}{\sqrt{2}}(|\uparrow\downarrow\rangle - |\downarrow\uparrow\rangle)$. They are sent one after another with a controlled delay Δt, hence the total unitary evolution:

$$\mathrm{U_{tot}} = \mathrm{Z}_\phi \times \mathrm{U} \otimes \mathrm{U} \times \mathrm{Z}_\phi \tag{5.8}$$

where $\phi = g\mu_\mathrm{B} B_z \Delta t/\hbar$ is the Larmor phase accumulated by one static spin under B_z for a duration Δt.

After transfer, the probability for the two electron spins to form a singlet state is:

$$\begin{aligned} P_\mathrm{S} &= |\langle S|\,\mathrm{U_{tot}}\,|S\rangle|^2 \\ &= \left|1 + |\mathrm{U}_{\uparrow\downarrow}|^2\left[\cos(\phi) - 1\right]\right|^2 \\ \text{where } |\mathrm{U}_{\uparrow\downarrow}|^2 &= \frac{\omega_\mathrm{SO}^2}{\omega_\mathrm{tot}^2}\sin^2\left(\frac{\omega_\mathrm{tot} t_\mathrm{S}}{2}\right) \end{aligned} \tag{5.9}$$

The singlet spin state probability therefore oscillates with the phase ϕ accumulated when one electron is static. This probability has always a maximum of 1 for $\phi = 0\ [2\pi]$, when constructive interferences bring the two-qubit system back to a singlet state no matter what the unitary transformation U is.

However, the oscillation contrast given by $2|\mathrm{U}_{\uparrow\downarrow}|^2$, depends on the axis and angle of the single spin rotation. It is equal to 1 for the condition:

$$\begin{aligned} |\mathrm{U}_{\uparrow\downarrow}|^2 &= \frac{1}{2} \\ \Leftrightarrow \sin^2\left(\frac{\pi l}{2 l_\mathrm{SO}}\sqrt{1 + \frac{B_z^2}{B_\mathrm{SO}^2}}\right) &= \frac{1}{2}\left(1 + \frac{B_z^2}{B_\mathrm{SO}^2}\right) \end{aligned} \tag{5.10}$$

This condition is equivalent to the one presented before, where the single-spin rotation maps the Bloch sphere poles $|\downarrow\rangle$ and $|\uparrow\rangle$ to opposite points located on the equator. As stated before, this condition is fulfilled for our particular channel length $l/l_\mathrm{SO} = 0.7\,\mathrm{ns}$ close to $|B_z| = B_{SO} = 25\,\mathrm{mT}$. In this case the singlet spin probability is simply:

$$P_\mathrm{S} = \left|\frac{1 + \cos(\phi)}{2}\right|^2 = \cos^4\left(\frac{\phi}{2}\right) \tag{5.11}$$

For $|B_z| < B_\mathrm{SO}$, $|\mathrm{U}_{\uparrow\downarrow}|^2 > \frac{1}{2}$ and we expect two minima per oscillation period. This corresponds to the frequency doubling observed in the data Fig. 5.2.

5.2.4 Numerical simulation

In the simulation whose output is presented in Fig. 5.5.a., we try to reproduce the main features of the experimental data. First, we introduce decoherence due to the hyperfine interaction during the static phase, different for both electron as occurring on different

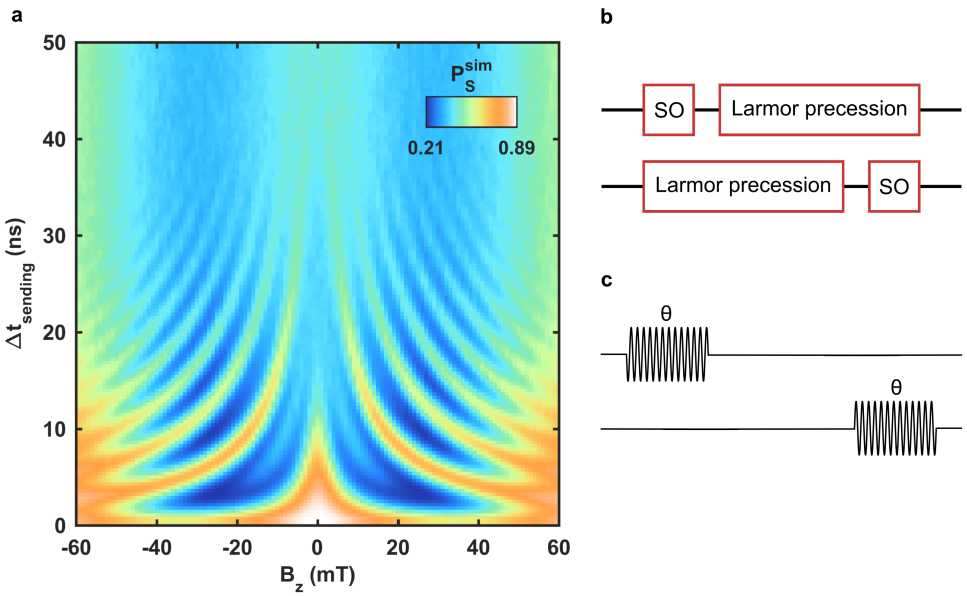

Figure 5.5: Numerical simulation. a. Simulated singlet spin probability as a function of the external magnetic field and the sending delay. The main features of the experimental data are well reproduce, and the simulation parameters are in good agreement with the expected values for GaAs. **b.** Scheme of each electron spin evolution. Both electrons experience the same single-spin rotation due to spin orbit coupling during their transfer and accumulate a phase ϕ due to the external magnetic field when they are static. **c.** Equivalent experiment with ESR pulses. Two pulses, driving a θ rotation, are applied to each qubit with a delay.

sides of the structure. We thus generate for each simulation shot two three-dimensional vectors $\boldsymbol{B}_{\mathrm{HF}}^{\boldsymbol{L}}$ and $\boldsymbol{B}_{\mathrm{HF}}^{\boldsymbol{R}}$ whose amplitudes follow a normal probability law of mean value 0 mT and standard deviation $\sigma_{\mathrm{HF}} = 2\,\mathrm{mT}$, this latter value being extracted from the T_2^* measurement in adjacent double quantum dots. No hyperfine interaction is considered during the displacement, as the large SAW speed leads to an important motional narrowing effect. However, we introduce the effect of the potential disorder, as developed in the previous section.

Finally, because of the finite bandwidth of the room-temperature electronics, we expect the voltage pulse used to inject the two electrons to exhibit a rising time close to $\sigma_t = 0.7\,\mathrm{ns}$. Because of this effect, we consider that the two electrons are at least separated by 0.7 ns, even when a single voltage pulse is applied. In addition, we consider an error rate of 5 % when electrons are not injected with the intended delay but instead by the same voltage pulse, leading to a 0.7 ns separation. This error rate is in agreement with the single electron transfer fidelity when two electrons are present in the sending dot.

The simulation output, visible in Fig. 5.5.a. and realized with 100 repetitions per pixel, is in good agreement with the experimental data. As we can see, this model is able to reproduce the main features of the experimental map obtained Fig. 5.2. In particular, we observe that the singlet probability at zero intended delay $\Delta t_{\mathrm{S}} = 0\,\mathrm{ns}$ oscillates with the applied magnetic field B_z. In addition, the behavior for the large sending delay limit

$\Delta t_S = 50\,\text{ns}$ is quite well reproduced. The parameters used in this simulation are either extracted from independent measurements on this sample or in agreement with similar works[Hua13; San11], to the exception of an 10 % contrast loss, not captured by our model and added manually. We can speculate that injection from static to moving quantum dots could be responsible for this limitation of the transfer process fidelity.

This simulation allows us to confirm that the main source of decoherence at large delays is the hyperfine coupling, whereas at small delays the potential inhomogeneities are responsible for the decoherence. It is interesting to note that this latter effect is always proportional to $\boldsymbol{B}$, and responsible for most of the contrast loss extracted in Chap. 4. In order to mitigate both of these effects, it appears crucial to send the two electrons together to achieve a highly coherent transfer, either by increasing the SAW amplitude or engineering the SAW burst shape. In addition, the effect of potential inhomogeneities can be mitigated by increasing the SAW confinement, limiting the electron motion inside the moving quantum dot.

5.3 Entanglement demonstration

For several decades, the debate on the existence of hidden variables making quantum mechanics an incomplete theory was mainly driven by thoughts experiments. Most famously, the EPR paradox[Ein35] (named after Einstein, Podolsky and Rosen) aimed at demonstrating the imperfect nature of quantum mechanics and its predicted violation of locality and realism. In 1964, John Bell presented an elegant mathematical criteria[Bel64] to settle this philosophical debate with an experimental result. Early work by Aspect *et al*[Asp76; Asp81], followed by a succession of more precise experiments to account for the measurement apparatus imperfections,[Giu15; Hen15; Shu12] indubitably proved the existence of entanglement between distant particles, and the ruled out hidden local variables.

Following Bell's initial demonstration, several experimental proofs can be produced to assert entanglement. Some involve measuring the probability to detect the system in specific *maximally entangled* quantum states, and setting thresholds above with entanglement is demonstrated. The Clauser-Horne-Shimony-Holt (CHSH) inequality was famously developed for the measurement of polarization correlations in a pair of photons, with an imperfect measurement apparatus.[Cla69] Other entanglement demonstrations rely on the measurement of some density matrix elements of the quantum state.[Ben96a; Sac00] Here, we present a protocol where two electrons, initially prepared in a singlet spin state, are separated and subjected to individual single-spin rotations before recombination. As we will see, the measurement of the singlet probability after transfer allows us to probe the entanglement of the initial state, and demonstrate that the electron spins remain entangled when separated one on each side of the 6 µm channel.

5.3.1 Entanglement threshold

We consider two spins in a non-entangled state, meaning that each spin contains its own information. The two-spin state can therefore be factorized:

$$|\psi\rangle = (a\,|\downarrow\rangle + b\,|\uparrow\rangle) \otimes (c\,|\downarrow\rangle + d\,|\uparrow\rangle) \tag{5.12}$$

with $|a|^2 + |b|^2 \leq 1$ and $|c|^2 + |d|^2 \leq 1$. From this normalization conditions, we obtain:

$$\begin{aligned} & |a|^2 + |b|^2 + |c|^2 + |d|^2 \leq 2 \\ \Leftrightarrow\ & (|a| - |d|)^2 + 2|ad| + (|b| - |c|)^2 + 2|bc| \leq 2 \\ \Leftrightarrow\ & |ad| + |bc| \leq 1 \\ \Leftrightarrow\ & (|ad| + |bc|)^2 \leq 1 \\ \Leftrightarrow\ & |ad|^2 + |bc|^2 + 2|abcd| \leq 1 \end{aligned} \tag{5.13}$$

On the another hand, the probability to measure a singlet spin state is:

$$\begin{aligned} P_{|S\rangle} &= |\langle S|\psi\rangle|^2 \\ &= \frac{|bc - ad|^2}{2} \\ &= \frac{|ad|^2 + |bc|^2 - 2\,\mathrm{Re}\left(\overline{bc}ad\right)}{2} \end{aligned} \tag{5.14}$$

Since $\mathrm{Re}\left(\overline{bc}ad\right) \leq |abcd|$, we necessarily have $P_{|S\rangle} \leq \frac{1}{2}$. Non-entangled particles cannot have a probability to be measured in a singlet state greater than $\frac{1}{2}$. A violation of this inequality would prove our assumption to be incorrect, meaning that the two-electron spin state is entangled, i.e. non-factorable.

Another important theorem is that entanglement cannot be destroyed or created by a coherent single-spin operation. Therefore, by measuring a singlet state probability above $\frac{1}{2}$ we can demonstrate that our spins remain entangled when separated.

5.3.2 Oscillation contrast

Our delay-controlled experiment can be interpreted as a form of Bell measurement, with two single-spin rotations on each qubit by the same angle θ with a phase evolution ϕ in-between. However, while in a standard Bell experiment only the phase ϕ is varied (and $\theta = \pi/2$), our experiment allows us to vary both θ and ϕ over a wide range ($\theta = 0 - 0.7\,$ß and $\phi = 0 - 2\,$ß). This allows us to perform a more complete analysis of the interference pattern, partially compensating our inability to perform a full quantum tomography in this sample.

For several magnetic fields B_z, we obtained in Fig. 5.2 a singlet probability above $\frac{1}{2}$ when the two electrons are separated ($\Delta t > 0$). In particular, $P^{\mathrm{cal}}_{|S\rangle}$ is always above this threshold for $\phi = 2\pi$, with a maximum of $P^{\mathrm{cal}}_{|S\rangle} = 0.692 \pm 0.005$ for $\Delta t = 9.2\,\mathrm{ns}$ and $B_z = -18\,\mathrm{mT}$. In this case, the first electron arrives well before the second is set in motion, so for some time both electrons are static and separated by the channel length, 6 µm. Yet, when recombined, the probability for their spin to form a singlet state is above the Bell threshold, proving entanglement at distance.

However, as the two electrons are recombined into a single quantum dot before the spin measurement, and since the singlet is then the ground spin state, this proof of entanglement is not free of experimental errors. Although the complete transfer and measurement sequence is one order of magnitude faster than the decay time in an isolated quantum dot

$T_1 = 4\,\text{ms}$, one may for example argue that some relaxation hotspot encountered during the sequence artificially increases the singlet probability. In addition, the few occurrences ($< 13\,\%$) where both electrons are sent with a 0.7 ns delay instead of the intended $\Delta t_{\text{sending}}$ lead to a slight over-estimation of the singlet spin probability.

To circumvent this issue, we study the singlet spin contrast between $\phi = 0$ ($B_z = 0\,\text{mT}$) and $\phi = \pi$ ($B_z = 22.5\,\text{mT}$, $\Delta t_{\text{sending}} = 4.16\,\text{ns}$). In the latter case, we expect destructive interferences to output a spin state mostly in the parallel basis ($m_S = \pm 1$). From Bell's inequality, we deduce that this spin contrast cannot be higher than $\frac{1}{2}$ for non-entangled states. On the contrary, for perfect singlet spin state initialization, the maximum of contrast is expected to be 1. However, because decoherence processes both increase $P_{|S\rangle}(\pi)$ and decrease $P_{|S\rangle}(0)$, the contrast $\Delta P_{|S\rangle} = P_{|S\rangle}(0) - P_{|S\rangle}(\pi)$ is extremely affected by these decoherence mechanisms.

In the experimental data presented Fig. 5.2., the minimum and maximum singlet probabilities for $\Delta t > 2.1\,\text{ns}$ are respectively 0.890 ± 0.003 and 0.249 ± 0.005. It corresponds then to an oscillation contrast of 0.641 ± 0.008, larger than 0.5 and thus a proof of entanglement. Even when the fidelity of the spin readout is not taken into account to calibrate the experimental data, we still observe a contrast well above this threshold (0.575 ± 0.008). While the results are affected by decoherence mechanisms, this is a demonstration of entanglement preservation all along the transfer process, and therefore to the creation of remote entanglement at 6 µm in a semiconductor quantum circuits. This second entanglement proof is stronger than the previous one, and enables us to prove that the SAW-assisted transfer is not only able to preserve an electron spin state, but also a efficient long-distance entanglement provider. Naturally, the strong hyperfine coupling of GaAs destroys this entanglement on extremely short timescales ($T_2 \approx 10\,\text{ns}$), but could be extended by dynamical decoupling techniques.

5.4 Density matrix evaluation

As we have seen, the contrast of the interferences observed Fig. 5.2. is due to the quantum correlations of the initial singlet spin state. In this section, we try to evaluate some elements of the density matrix ρ of the initial spin state and demonstrate that the sequential transfer procedure acts as a partial state tomography measurement. In this regard, we exploit our ability to destroy a spin state coherence via spin mixing in adjacent quantum dots before performing the sending procedure. We separate the two electrons for 500 ns in the (1,1) configuration of the right double quantum dot, as covered in Chap. 4. After such a mixing operation, the anti-parallel/parallel probabilities are preserved ($\rho_{\downarrow\uparrow} + \rho_{\uparrow\downarrow}$ is unchanged), but the phase information is lost ($\rho_{i,j} = 0$ for $i \neq j$).

As we can only perform a partial state tomography, we have to formulate a few assumptions on the initial state of our system. We assume that no correlations exist between the parallel and anti-parallel spin basis, but only $\rho_{\downarrow\downarrow,\uparrow\uparrow}$ and $\rho_{\downarrow\uparrow,\uparrow\downarrow}$ are non-zero. In this

uncoupled spin basis the density matrix is thus of the form:

$$\begin{pmatrix} \rho_{\downarrow\downarrow} & 0 & 0 & \rho_{\downarrow\downarrow,\uparrow\uparrow} \\ 0 & \rho_{\downarrow\uparrow} & \rho_{\downarrow\uparrow,\uparrow\downarrow} & 0 \\ 0 & \overline{\rho_{\downarrow\uparrow,\uparrow\downarrow}} & \rho_{\uparrow\downarrow} & 0 \\ \overline{\rho_{\downarrow\downarrow,\uparrow\uparrow}} & 0 & 0 & \rho_{\uparrow\uparrow} \end{pmatrix} \tag{5.15}$$

At the particular magnetic field $B_z = 25\,\mathrm{mT}$, the expected spin singlet probabilities after transfer for $\phi = \pi$ and $\phi = 2\pi$ are in this case:

	$t_{\mathrm{mix}} = 0\,\mathrm{ns}$	$t_{\mathrm{mix}} = 500\,\mathrm{ns}$
$\phi = \pi$	$\frac{\rho_{\uparrow\uparrow}+\rho_{\downarrow\downarrow}}{2} - Re(\rho_{\uparrow\uparrow,\downarrow\downarrow})$	$\frac{\rho_{\uparrow\uparrow}+\rho_{\downarrow\downarrow}}{2}$
$\phi = 2\pi$	$\frac{\rho_{\uparrow\downarrow}+\rho_{\downarrow\uparrow}}{2} - Re(\rho_{\uparrow\downarrow,\downarrow\uparrow})$	$\frac{\rho_{\uparrow\downarrow}+\rho_{\downarrow\uparrow}}{2}$

(5.16)

With the addition of the mixing pulse, the transfer procedure is thus a direct measurement of the parallel and anti-parallel spin probabilities and correlations. As expected, in the absence of quantum correlations the mixing operation has no effect. Such an experiment is thus able to give a lower bound off the magnitude of these off-diagonal terms.

Figure 5.6. represents the outcome of this type of measurement realized at $B_{\mathrm{Z}} = 25\,\mathrm{mT}$. The measured singlet spin probabilities after transfer at $\phi = \pi$ and $\phi = 2\pi$ allows us to give an estimation of the off-diagonal density matrix elements:

$$\begin{aligned} Re(\rho_{\downarrow\downarrow,\uparrow\uparrow}) &= +0.01 \pm 0.02 \\ Re(\rho_{\downarrow\uparrow,\uparrow\downarrow}) &= -0.16 \pm 0.02 \end{aligned} \tag{5.17}$$

We obtain a high anti-parallel correlation and no parallel correlations, in good agreement with an initial singlet spin state:

$$|S\rangle\langle S| = \begin{pmatrix} 0 & 0 & 0 & 0 \\ 0 & \frac{1}{2} & -\frac{1}{2} & 0 \\ 0 & -\frac{1}{2} & \frac{1}{2} & 0 \\ 0 & 0 & 0 & 0 \end{pmatrix} \tag{5.18}$$

From singlet spin probability measured at $\phi = \pi$ and $\phi = 2\pi$ with a mixing pulse, we should be able to determine the parallel and anti-parallel probabilities $P_{sym} = \rho_{\downarrow\downarrow} + \rho_{\uparrow\uparrow}$ and $P_{anti} = \rho_{\downarrow\uparrow} + \rho_{\uparrow\downarrow}$. However, because of the decoherence processes affecting our transfer procedure, we can only access an upper bound of the anti-parallel probability, using the maximum singlet probability obtained with the mixing pulse:

$$P_{anti} > 2P^{\mathrm{cal}}_{|S\rangle}(2\pi) = 0.85 \pm 0.02 \tag{5.19}$$

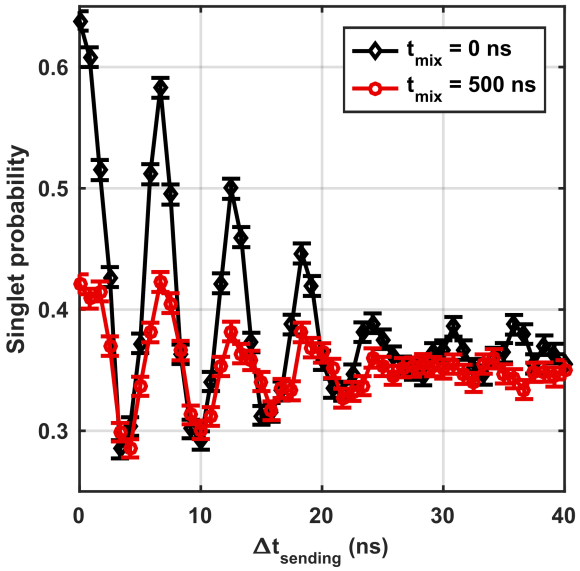

Figure 5.6: Initial state coherence. Singlet spin probability at $B_z = 25\,\mathrm{mT}$ for two different state preparation. The black set of points corresponds to an initial singlet spin state, while for the red set of points a 500 ns mixing pulse separates the two electrons in the right double quantum dot, effectively destroying their coherence before the sending procedure. The contrast between these two curves at $\phi = \pi$ (resp. $\phi = 2\pi$) is a direct measure of parallel (resp. anti-parallel) correlations of the initial spin state. We observe that the mixing operation has a strong impact on the singlet spin probability after transfer for $\phi = 2\pi$, while for $\phi = \pi$ it has no effect. This result is a signature of an initial singlet spin state.

This high antiparallel probability is once again in good agreement with a initial singlet state. From these density matrix elements, we can calculate a lower bound of the Bell fidelity[Ben96b; Sac00]:

$$\mathcal{F}_\mathrm{B} = \frac{P_\mathrm{anti}}{2} + |\rho_{\downarrow\uparrow,\uparrow\downarrow}| > 0.58 \pm 0.02 \tag{5.20}$$

As a Bell fidelity above $\frac{1}{2}$ is a proof of entanglement, this experiment is a third proof of the initial spin state correlations.

5.5 Conclusion

In this chapter, we study the transfer of a two-electron singlet spin state, propelled by a propagating surface acoustic wave. We sequentially shuttle each electron across the channel, and measure the probability for their spin to form a singlet state after recombination. At zero magnetic field, we observe a maximum singlet preservation of 89.5 % when the two electrons are transported with a minimum delay, and decoherence as the electrons are separated for a longer duration. Varying the external magnetic field, we obtain a high-contrast interference pattern, signature of the single-spin rotation endured by the

electron during its motion. We develop a model based on the spin-orbit interaction created by the fast SAW-assisted shuttling, and discuss the main decoherence mechanisms affecting the two-electron spin transfer. In particular, we see the evidence of spin mixing during the motion, driven by the electrostatic potential inhomogeneities along the path of the electron.

We interpret the sequential sending procedure as a Bell measurement, in order to probe the correlations of the initial spin state and demonstrate the persistance of entanglement at distance, when the two electrons are separated by the 6 µm long channel. Although decoherence processes affect the measurement visibility, we can still provide evidences of the preservation of an entanglement above Bell threshold. Firstly, the singlet spin probability after transfer is above 50 % regardless of the magnetic field at the position of the first constructive interference, $\phi = 2\pi$. Secondly, close to $B_z = 25\,\mathrm{mT}$ the contrast between this value and the one measured at $\phi = \pi$ is also greater than 50 %, which is a more restrictive entanglement demonstration. The low singlet spin probability obtained in this later case is an evidence of the coherent transformation of the two-electron spin state towards the parallel spin basis ($|{\downarrow\downarrow}\rangle$, $|{\uparrow\uparrow}\rangle$).

Finally, we exploit our ability to let a singlet-triplet qubit decohere in the (1,1) configuration of an adjacent double quantum dot to study the anti-parallel correlations of the initial state. For this purpose, we use a long mixing pulse to let the two electron spins decohere before performing the sending procedure. Comparing the measurement output after transfer with and without mixing pulse, we extract a lower bound of the anti-diagonal elements of the density matrix $Re(\rho_{\downarrow\downarrow,\uparrow\uparrow}) = +0.01 \pm 0.02$ and $Re(\rho_{\downarrow\uparrow,\uparrow\downarrow}) = -0.16 \pm 0.02$. The presence of strong anti-parallel correlations is in agreement with an initial singlet spin state, and another proof of the entanglement-preserving nature of the spin transfer procedure.

Conclusion and perspectives

In this work, we demonstrated the realization of a coherent link between two quantum nodes, achieving the coherent transfer of a singlet spin state between two double quantum dots separated by a 6 µm depleted channel. Exploiting a ns-control over the transfer of individual electrons, we are able to introduce a delay between two entangled electrons and study the decoherence processes affecting them both during the transfer and in the static quantum dots. The singlet preservation fidelity reaches 89.5 ± 0.3 % at zero magnetic field, proving the coherent nature of the spin transfer protocol. Under a non-zero magnetic field, we observe oscillations in the singlet probability measured after transfer, that we attribute to the effect of spin-orbit interactions during the shuttling of individual electrons driving single-spin rotations. Added up to the coherent Larmor precession of the two spins during their separation, they give rise to a high-contrast interference pattern, that we exploit to probe the remote entanglement between these two electron spins.

Interpreting this experiment as a form of Bell measurement, we demonstrate the entanglement preservation throughout the transfer protocol, in particular when both electrons are static and separated by 6 µm. For this, we consider the singlet probability after transfer as B_z and $\Delta t_{\text{sending}}$ are varied, and measure a maximum contrast of 0.641 ± 0.008 well above the 50 % threshold required for an entanglement proof. In addition, we perform a partial evaluation of the initial density matrix, which we find in good agreement with an initial singlet state. Although affected by decoherence processes and impaired by our inability to perform full-state tomography, this experiment is still able to demonstrate the entanglement between two remotely separated electron spins, proving the SAW-assisted electron displacement as a robust long-range entanglement mediator.

The high-frequency single-spin rotations at the single electron level are several times faster than any decoherence process during the transfer, as the result of the large electron velocity ($v_{\text{SAW}} = 2700$ m/s, the speed of sound in GaAs). However, the effect of potential inhomogeneities, perturbing the electron path from a straight line, appear as a main decoherence mechanism in our system, particularly towards high magnetic fields. This experimental result is important in the framework of the current race towards scalability of quantum semiconductor circuits. Indeed, it appears crucial to reduce the potential inhomogeneities along the electron path, or to induce their confinement. This can be done in GaAs by engineering the SAW pulse to create a so-called *chirp* pulse, where the resonant frequency of the transducer is spatially varied. As visible in Fig. 6.7. Here, an IDT of 3 GHz bandwidth is excited by a voltage pulse of increasing frequency, such that

each frequency is progressively added as the SAW burst propagates towards the right side. These different frequencies then destructively interfere, reducing the pulse to a single SAW minimum. In addition to the lower excitation of the system as the SAW propagates, two moving dots with an arbitrary separation can be engineered (see Fig. 6.7c.), providing a much more precise control over the electron separation time. All together, this SAW pulse engineering should mitigate the observed decoherence during the electron transfer protocol.

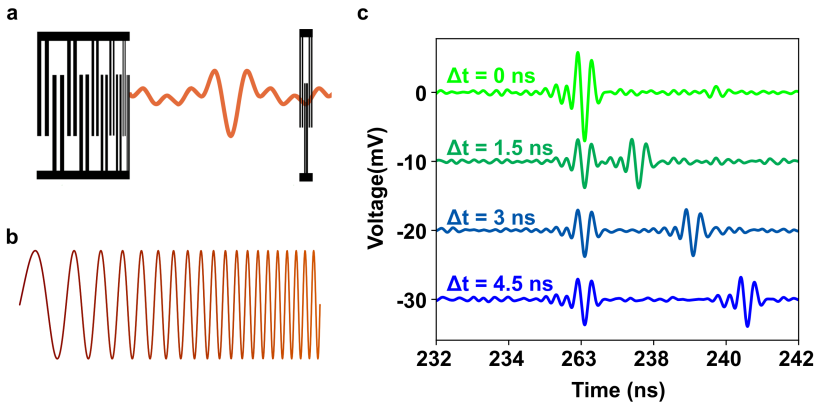

Figure 6.7: SAW pulse engineering. a. Scheme of the chirp IDT and the detector. **b.** Voltage pulse applied on one electrode of the transducer. The frequency is progressively increased within a time equal to the SAW propagation time under the IDT. **c.** Room-temperature measurements of two single SAW minima generated with a 0, 1.5, 3 and 4.5 ns delay. As the phase velocity is constant in this frequency range, this delay remains constant throughout the propagation.

Due to the poor coherence time of GaAs, the focus of the semiconductor quantum circuits community is now evolving towards Si-based samples, which present key advantages in terms of scalability. In particular, recent qubit demonstrations using Si-MOS transistors have been provided.[Mau16; Urd19] The type of electron shuttling used in this thesis could be adapted to this technology, providing a few adjustments. First, as Silicon is not piezoelectric, one would need to either deposit a piezoelectric material on top of the substrate (which steers away from the transistor industry protocols), or mimic the propagating electrical potential by using metallic gates. This last technique is presented in Fig. 6.8., where an artistic view illustrates the spin-shuttling protocol. This type of samples have already been fabricated, and will soon be measured as a continuation of the work presented in this thesis.

Using a Si substrate will also be beneficial in terms of coherence time, as we saw that the poor coherence time of GaAs ($T_2^* = 12$ ns) limits our qubit control. Using isotopically purified ^{28}Si, coherence times several orders of magnitude higher can be achieved. Moreover, electrons in bulk Si have a weak spin-orbit coupling, limiting their susceptibility to electrostatic noise during the electron transport. However, recent results point at a strong increase of the spin-orbit coupling as the electron wavefunction is pushed towards an interface, which is particularly the case in Si-MOS devices. Therefore, surface roughness and other potential inhomogeneities may still play an important role in the decoherence along the electron path, and will need to be accounted for. It thus appears

critical to manage the electron path and confinement in order to perform a reproducible and controlled coherent electron spin transfer protocol.

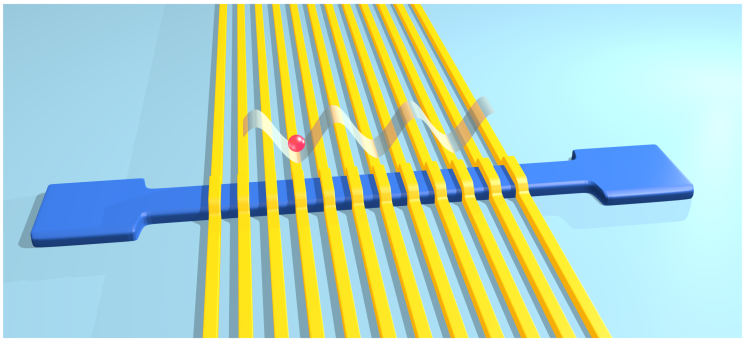

Figure 6.8: Si-MOS sample. Artistic view of a Si-MOS based electron transfer experiment, where metallic gates are used to generate the propagating electrical potential.

Bibliography

[Ang07] S. J. Angus, A. J. Ferguson, A. S. Dzurak, and R. G. Clark: 'Gate-Defined Quantum Dots in Intrinsic Silicon', *Nano Letters* **7** (2007), 2051–2055, DOI: 10.1021/nl070949k (see p. 6).

[Asp76] Alain Aspect: 'Proposed experiment to test the nonseparability of quantum mechanics', *Physical Review D* **14** (1976), 1944–1951, DOI: 10.1103/PhysRevD.14.1944 (see p. 86).

[Asp81] Alain Aspect, Philippe Grangier, and Gérard Roger: 'Experimental Tests of Realistic Local Theories via Bell's Theorem', *Physical Review Letters* **47** (1981), 460–463, DOI: 10.1103/PhysRevLett.47.460 (see pp. 1, 86).

[Aws18] David D. Awschalom, Ronald Hanson, Jörg Wrachtrup, and Brian B. Zhou: 'Quantum technologies with optically interfaced solid-state spins', en, *Nature Photonics* **12** (2018), 516–527, DOI: 10.1038/s41566-018-0232-2 (see p. 2).

[Baa16] T. A. Baart, M. Shafiei, T. Fujita, C. Reichl, W. Wegscheider, and L. M. K. Vandersypen: 'Single-spin CCD', *Nature Nanotechnology* **11** (2016), 330–334, DOI: 10.1038/nnano.2015.291 (see p. 2).

[Bar14] R. Barends et al.: 'Superconducting quantum circuits at the surface code threshold for fault tolerance', en, *Nature* **508** (2014), 500–503, DOI: 10.1038/nature13171 (see p. 2).

[Bar10] C. Barthel, J. Medford, C. M. Marcus, M. P. Hanson, and A. C. Gossard: 'Interlaced Dynamical Decoupling and Coherent Operation of a Singlet-Triplet Qubit', *Phys. Rev. Lett.* **105** (2010), 266808, DOI: 10.1103/PhysRevLett.105.266808 (see p. 10).

[Bar09] C. Barthel, D. J. Reilly, C. M. Marcus, M. P. Hanson, and A. C. Gossard: 'Rapid Single-Shot Measurement of a Singlet-Triplet Qubit', en, *Physical Review Letters* **103** (2009), DOI: 10.1103/PhysRevLett.103.160503 (see p. 22).

[Bel64] J. S. Bell: 'On the Einstein Podolsky Rosen paradox', *Physics Physique Fizika* **1** (1964), 195–200, DOI: 10.1103/PhysicsPhysiqueFizika.1.195 (see p. 86).

[Ben96a] Charles H. Bennett, David P. DiVincenzo, John A. Smolin, and William K. Wootters: 'Mixed-state entanglement and quantum error correction', en, *Physical Review A* **54** (1996), 3824–3851, DOI: 10.1103/PhysRevA.54.3824 (see p. 86).

[Ben96b] Charles H. Bennett, Gilles Brassard, Sandu Popescu, Benjamin Schumacher, John A. Smolin, and William K. Wootters: 'Purification of Noisy Entanglement and Faithful Teleportation via Noisy Channels', en, *Physical Review Letters* **76** (1996), 722–725, DOI: 10.1103/PhysRevLett.76.722 (see p. 90).

[Ber16a] B. Bertrand, S. Hermelin, S. Takada, M. Yamamoto, S. Tarucha, A. Ludwig, A. D. Wieck, C. Bäuerle, and T. Meunier: 'Fast spin information transfer between distant quantum dots using individual electrons', en, *Nature Nanotechnology* **11** (2016), 672–676, DOI: 10.1038/nnano.2016.82 (see p. 73).

[Ber15a] Benoit Bertrand: 'Transport d'information de spin à l'échelle de l'électron unique', Theses, Université Grenoble Alpes, 2015 (see pp. 35, 67).

[Ber16b] Benoit Bertrand, Sylvain Hermelin, Pierre-André Mortemousque, Shintaro Takada, Michihisa Yamamoto, Seigo Tarucha, Arne Ludwig, Andreas D Wieck, Christopher Bäuerle, and Tristan Meunier: 'Injection of a single electron from static to moving quantum dots', *Nanotechnology* **27** (2016), 214001, DOI: 10.1088/0957-4484/27/21/214001 (see p. 54).

[Ber15b] Benoit Bertrand, Hanno Flentje, Shintaro Takada, Michihisa Yamamoto, Seigo Tarucha, Arne Ludwig, Andreas D. Wieck, Christopher Bäuerle, and Tristan Meunier: 'Quantum Manipulation of Two-Electron Spin States in Isolated Double Quantum Dots', en, *Physical Review Letters* **115** (2015), DOI: 10.1103/PhysRevLett.115.096801 (see pp. 13, 27, 49, 71).

[Blu11] Hendrik Bluhm, Sandra Foletti, Izhar Neder, Mark Rudner, Diana Mahalu, Vladimir Umansky, and Amir Yacoby: 'Dephasing time of GaAs electron-spin qubits coupled to a nuclear bath exceeding 200 us', en, *Nature Physics* **7** (2011), 109–113, DOI: 10.1038/nphys1856 (see pp. 20, 22).

[Blu10] Hendrik Bluhm, Sandra Foletti, Diana Mahalu, Vladimir Umansky, and Amir Yacoby: 'Enhancing the Coherence of a Spin Qubit by Operating it as a Feedback Loop That Controls its Nuclear Spin Bath', *Physical Review Letters* **105** (2010), 216803, DOI: 10.1103/PhysRevLett.105.216803 (see pp. 20, 23).

[Bra05] P.-F. Braun, X. Marie, L. Lombez, B. Urbaszek, T. Amand, P. Renucci, V. K. Kalevich, K. V. Kavokin, O. Krebs, P. Voisin, and Y. Masumoto: 'Direct Observation of the Electron Spin Relaxation Induced by Nuclei in Quantum Dots', *Phys. Rev. Lett.* **94** (2005), 116601, DOI: 10.1103/PhysRevLett.94.116601 (see p. 22).

[Byc84] Yu. A. Bychkov and E. I. Rashba: 'Properties of a 2D electron gas with lifted spectral degeneracy', *JETP lett* **39** (1984), 78 (see p. 24).

[Cla69] John F. Clauser, Michael A. Horne, Abner Shimony, and Richard A. Holt: 'Proposed Experiment to Test Local Hidden-Variable Theories', *Physical Review Letters* **23** (1969), 880–884, DOI: 10.1103/PhysRevLett.23.880 (see p. 86).

[Col13] J. I. Colless, A. C. Mahoney, J. M. Hornibrook, A. C. Doherty, H. Lu, A. C. Gossard, and D. J. Reilly: 'Dispersive Readout of a Few-Electron Double Quantum Dot with Fast rf Gate Sensors', en, *Physical Review Letters* **110** (2013), DOI: 10.1103/PhysRevLett.110.046805 (see p. 19).

[Cre11] Andrea Crespi, Roberta Ramponi, Roberto Osellame, Linda Sansoni, Irene Bongioanni, Fabio Sciarrino, Giuseppe Vallone, and Paolo Mataloni: 'Integrated photonic quantum gates for polarization qubits', en, *Nature Communications* **2** (2011), 1–6, DOI: 10.1038/ncomms1570 (see p. 2).

[Dat90] S. Datta and B. Das: 'Electronic analog of the electro-optic modulator', *Applied Physics Letters* **56** (1990), 665, DOI: 10.1063/1.102730 (see p. 28).

[Dek99] C. Dekker: 'Carbon nanotubes as molecular quantum wires', *Physics today* **52** (1999), 22–30 (see p. 5).

[DiV00] D. P. DiVincenzo: 'The Physical Implementation of Quantum Computation', *Fortschritte der Physik* **48** (2000), 771–783 (see p. 1).

[Dre55] G. Dresselhaus: 'Spin-Orbit Coupling Effects in Zinc Blende Structures', *Phys. Rev.* **100** (1955), 580–586, DOI: 10.1103/PhysRev.100.580 (see p. 24).

[Dut05] M. V. G. Dutt, J. Cheng, B. Li, X. Xu, X. Li, P. R. Berman, D. G. Steel, A. S. Bracker, D. Gammon, S. E. Economou, R.-B. Liu, and L. J. Sham: 'Stimulated and Spontaneous Optical Generation of Electron Spin Coherence in Charged GaAs Quantum Dots', *Phys. Rev. Lett.* **94** (2005), 227403, DOI: 10.1103/PhysRevLett.94.227403 (see p. 22).

[Ein35] A. Einstein, B. Podolsky, and N. Rosen: 'Can Quantum-Mechanical Description of Physical Reality Be Considered Complete?', *Physical Review* **47** (1935), 777–780, DOI: 10.1103/PhysRev.47.777 (see p. 86).

[Eks17] Maria K. Ekström, Thomas Aref, Johan Runeson, Johan Björck, Isac Boström, and Per Delsing: 'Surface acoustic wave unidirectional transducers for quantum applications', en, *Applied Physics Letters* **110** (2017), 073105, DOI: 10.1063/1.4975803 (see p. 29).

[Elz03] J. M. Elzerman, R. Hanson, J. S. Greidanus, L. H. Willems van Beveren, S. De Franceschi, L. M. K. Vandersypen, S. Tarucha, and L. P. Kouwenhoven: 'Few-electron quantum dot circuit with integrated charge read out', en, *Physical Review B* **67** (2003), DOI: 10.1103/PhysRevB.67.161308 (see p. 9).

[Elz04] J. M. Elzerman, R. Hanson, L. H. Willems van Beveren, B. Witkamp, L. M. K. Vandersypen, and L. P. Kouwenhoven: 'Single-shot read-out of an individual electron spin in a quantum dot', *Nature* **430** (2004), 431–435, DOI: 10.1038/nature02693 (see p. 15).

[Fey82] R. P. Feynman: 'Simulating physics with computers', English, *International Journal of Theoretical Physics* **21** (1982), 467–488, DOI: 10.1007/BF02650179 (see p. 1).

[Fle17] H. Flentje, P.-A. Mortemousque, R. Thalineau, A. Ludwig, A. D. Wieck, C. Bäuerle, and T. Meunier: 'Coherent long-distance displacement of individual electron spins', en, *Nature Communications* **8** (2017), DOI: 10.1038/s41467-017-00534-3 (see p. 74).

[Fod00] C. L. Foden, V. I. Talyanskii, G. J. Milburn, M. L. Leadbeater, and M. Pepper: 'High-frequency acousto-electric single-photon source', *Phys. Rev. A* **62** (2000), 011803, DOI: 10.1103/PhysRevA.62.011803 (see p. 30).

[Fol09] Sandra Foletti, Hendrik Bluhm, Diana Mahalu, Vladimir Umansky, and Amir Yacoby: 'Universal quantum control of two-electron spin quantum bits using dynamic nuclear polarization', en, *Nature Physics* **5** (2009), arXiv: 1009.5343, 903–908, DOI: 10.1038/nphys1424 (see p. 19).

[Fow12] A. Fowler, M. Mariantoni, J. Martinis, and A. Cleland: 'Surface codes: Towards practical large-scale quantum computation', *Phys. Rev. A* **86** (2012), 032324, DOI: 10.1103/PhysRevA.86.032324 (see p. 2).

[Giu15] Marissa Giustina et al.: 'Significant-Loophole-Free Test of Bell's Theorem with Entangled Photons', en, *PHYSICAL REVIEW LETTERS* (2015), 7 (see p. 86).

[Gol04] V. N. Golovach, A. Khaetskii, and D. Loss: 'Phonon-Induced Decay of the Electron Spin in Quantum Dots', *Phys. Rev. Lett.* **93** (2004), 016601, DOI: 10.1103/PhysRevLett.93.016601 (see p. 20).

[Gro96] L. K. Grover: 'A Fast Quantum Mechanical Algorithm for Database Search', *Proceedings of the Twenty-eighth Annual ACM Symposium on Theory of Computing*, event-place: Philadelphia, Pennsylvania, USA, 1996, 212–219, DOI: 10.1145/237814.237866 (see p. 1).

[Gus09] S. Gustavsson, R. Leturcq, M. Studer, I. Shorubalko, T. Ihn, K. Ensslin, D. C. Driscoll, and A. C. Gossard: 'Electron counting in quantum dots', *Surface Science Reports* **64** (2009), 191–232, DOI: 10.1016/j.surfrep.2009.02.001 (see p. 9).

[Hah50] E. L. Hahn: 'Spin Echoes', *Phys. Rev.* **80** (1950), 580–594, DOI: 10.1103/PhysRev.80.580 (see p. 20).

[Han05] R. Hanson, L. H. Willems van Beveren, I. T. Vink, J. M. Elzerman, W. J. M. Naber, F. H. L. Koppens, L. P. Kouwenhoven, and L. M. K. Vandersypen: 'Single-Shot Readout of Electron Spin States in a Quantum Dot Using Spin-Dependent Tunnel Rates', en, *Physical Review Letters* **94** (2005), DOI: 10.1103/PhysRevLett.94.196802 (see p. 16).

[Han07] R. Hanson, L. P. Kouwenhoven, J. R. Petta, S. Tarucha, and L. M. K. Vandersypen: 'Spins in few-electron quantum dots', *Reviews of Modern Physics* **79** (2007), 1217–1265, DOI: 10.1103/RevModPhys.79.1217 (see pp. 8, 9, 21).

[HC18] Patrick Harvey-Collard, Benjamin D'Anjou, Martin Rudolph, N. Tobias Jacobson, Jason Dominguez, Gregory A. Ten Eyck, Joel R. Wendt, Tammy Pluym, Michael P. Lilly, William A. Coish, Michel Pioro-Ladrière, and Malcolm S. Carroll: 'High-Fidelity Single-Shot Readout for a Spin Qubit via an Enhanced Latching Mechanism', *Physical Review X* **8** (2018), 021046, DOI: 10.1103/PhysRevX.8.021046 (see p. 18).

[Hen15] B. Hensen et al.: 'Loophole-free Bell inequality violation using electron spins separated by 1.3 kilometres', en, *Nature* **526** (2015), 682–686, DOI: 10.1038/nature15759 (see pp. 1, 86).

[Her11] Sylvain Hermelin, Shintaro Takada, Michihisa Yamamoto, Seigo Tarucha, Andreas D. Wieck, Laurent Saminadayar, Christopher Bäuerle, and Tristan Meunier: 'Electrons surfing on a sound wave as a platform for quantum optics with flying electrons', en, *Nature* **477** (2011), 435–438, DOI: 10.1038/nature10416 (see pp. 2, 30, 54).

[Hua13] Peihao Huang and Xuedong Hu: 'Spin qubit relaxation in a moving quantum dot', *Physical Review B* **88** (2013), 075301, DOI: 10.1103/PhysRevB.88.075301 (see pp. 74, 83, 86, 120).

[Ito14] Kohei M. Itoh and Hideyuki Watanabe: 'Isotope engineering of silicon and diamond for quantum computing and sensing applications', en, *MRS Communications* **4** (2014), 143–157, DOI: 10.1557/mrc.2014.32 (see p. 20).

[Jel04] F. Jelezko, T. Gaebel, I. Popa, M. Domhan, A. Gruber, and J. Wrachtrup: 'Observation of Coherent Oscillation of a Single Nuclear Spin and Realization of a Two-Qubit Conditional Quantum Gate', *Phys. Rev. Lett.* **93** (2004), 130501, DOI: 10.1103/PhysRevLett.93.130501 (see p. 2).

[Joh05] A. C. Johnson, J. R. Petta, C. M. Marcus, M. P. Hanson, and A. C. Gossard: 'Singlet-triplet spin blockade and charge sensing in a few-electron double quantum dot', *Phys. Rev. B* **72** (2005), 165308, DOI: 10.1103/PhysRevB.72.165308 (see p. 18).

[Kaw14] E. Kawakami, P. Scarlino, D. R. Ward, F. R. Braakman, D. E. Savage, M. G. Lagally, Mark Friesen, S. N. Coppersmith, M. A. Eriksson, and L. M. K. Vandersypen: 'Electrical control of a long-lived spin qubit in a Si/SiGe quantum dot', en, *Nature Nanotechnology* **9** (2014), 666–670, DOI: 10.1038/nnano.2014.153 (see p. 26).

[Ken02] T.A. Kennedy, F.T. Charnock, J.S. Colton, J.E. Butler, R.C. Linares, and P.J. Doering: 'Single-Qubit Operations with the Nitrogen-Vacancy Center in Diamond', *physica status solidi (b)* **233** (2002), 416–426 (see p. 2).

[Kle96] D. L. Klein, P. L. McEuen, J. E. Bowen Katari, R. Roth, and A. P. Alivisatos: 'An approach to electrical studies of single nanocrystals', *Applied Physics Letters* **68** (1996), 2574–2576, DOI: 10.1063/1.116188 (see p. 5).

[Kop06] F. H. L. Koppens, C. Buizert, K-J. Tielrooij, I. T. Vink, K. C. Nowack, T. Meunier, L. P. Kouwenhoven, and L. M. K. Vandersypen: 'Driven coherent oscillations of a single electron spin in a quantum dot', *Nature* **442** (2006), 766–771, DOI: 10.1038/nature05065 (see pp. 2, 25, 26).

[Kou97] L. P. Kouwenhoven, C. M. Marcus, P. L. McEuen, S. Tarucha, R. M. Westervelt, and N. S. Wingreen: 'Electron Transport in Quantum Dots', English, *Mesoscopic Electron Transport*, vol. 345, 1997, 105–214, DOI: 10.1007/978-94-015-8839-3_4 (see p. 5).

[Kou01] L. P. Kouwenhoven, D. G. Austing, and S. Tarucha: 'Few-electron quantum dots', *Reports on Progress in Physics* **64** (2001), 701–736, DOI: 10.1088/0034-4885/64/6/201 (see p. 5).

[Lan32] L. D. Landau: 'On the theory of transfer of energy at collisions II', *Phys. Z. Sowjetunion* **2** (1932), 46–51 (see p. 69).

[Lan18] A. J. Landig, J. V. Koski, P. Scarlino, U. C. Mendes, A. Blais, C. Reichl, W. Wegscheider, A. Wallraff, K. Ensslin, and T. Ihn: 'Coherent spin–photon coupling using a resonant exchange qubit', En, *Nature* **560** (2018), 179, DOI: 10.1038/s41586-018-0365-y (see p. 2).

[Law19] W. I. L. Lawrie et al.: 'Quantum Dot Arrays in Silicon and Germanium', en, *arXiv:1909.06575 [cond-mat]* (2019), arXiv: 1909.06575 (see p. 6).

[Li15] Hai-Ou Li, Gang Cao, Guo-Dong Yu, Ming Xiao, Guang-Can Guo, Hong-Wen Jiang, and Guo-Ping Guo: 'Conditional rotation of two strongly coupled semiconductor charge qubits', en, *Nature Communications* **6** (2015), 1–9, DOI: 10.1038/ncomms8681 (see p. 59).

[Li13] Jiun-Yun Li, Chiao-Ti Huang, Leonid P. Rokhinson, and James C. Sturm: 'Extremely high electron mobility in isotopically-enriched 28Si two-dimensional electron gases grown by chemical vapor deposition', *Applied Physics Letters* **103** (2013), 162105, DOI: 10.1063/1.4824729 (see p. 6).

[Lim05] M. M. de Lima and P. V. Santos: 'Modulation of photonic structures by surface acoustic waves', *Reports on Progress in Physics* **68** (2005), 1639, DOI: 10.1088/0034-4885/68/7/R02 (see p. 2).

[Los98] D. Loss and D. P. DiVincenzo: 'Quantum computation with quantum dots', *Phys. Rev. A* **57** (1998), 120–126, DOI: 10.1103/PhysRevA.57.120 (see p. 2).

[Mal19] Filip K. Malinowski, Frederico Martins, Thomas B. Smith, Stephen D. Bartlett, Andrew C. Doherty, Peter D. Nissen, Saeed Fallahi, Geoffrey C. Gardner, Michael J. Manfra, Charles M. Marcus, and Ferdinand Kuemmeth: 'Fast spin exchange across a multielectron mediator', En, *Nature Communications* **10** (2019), 1196, DOI: 10.1038/s41467-019-09194-x (see p. 2).

[Mau16] R. Maurand, X. Jehl, D. Kotekar-Patil, A. Corna, H. Bohuslavskyi, R. Laviéville, L. Hutin, S. Barraud, M. Vinet, M. Sanquer, and S. De Franceschi: 'A CMOS silicon spin qubit', en, *Nature Communications* **7** (2016), 1–6, DOI: 10.1038/ncomms13575 (see p. 94).

[McE00] P. L. McEuen: 'Single-wall carbon nanotubes', *Physics World* **13** (2000), 31–36 (see p. 5).

[McN11] R. P. G. McNeil, M. Kataoka, C. J. B. Ford, C. H. W. Barnes, D. Anderson, G. a. C. Jones, I. Farrer, and D. A. Ritchie: 'On-demand single-electron transfer between distant quantum dots', en, *Nature* **477** (2011), 439–442, DOI: 10.1038/nature10444 (see pp. 2, 30).

[Mei90] U. Meirav, M. A. Kastner, and S. J. Wind: 'Single-electron charging and periodic conductance resonances in GaAs nanostructures', *Physical Review Letters* **65** (1990), 771–774, DOI: 10.1103/PhysRevLett.65.771 (see p. 6).

[Mer02] I. A. Merkulov, Al L. Efros, and M. Rosen: 'Electron spin relaxation by nuclei in semiconductor quantum dots', *Physical Review B* **65** (2002), arXiv: cond-mat/0202271, DOI: 10.1103/PhysRevB.65.205309 (see p. 67).

[Meu07] T. Meunier, I. T. Vink, L. H. Willems van Beveren, K-J. Tielrooij, R. Hanson, F. H. L. Koppens, H. P. Tranitz, W. Wegscheider, L. P. Kouwenhoven, and L. M. K. Vandersypen: 'Experimental Signature of Phonon-Mediated Spin Relaxation in a Two-Electron Quantum Dot', en, *Physical Review Letters* **98** (2007), DOI: 10.1103/PhysRevLett.98.126601 (see p. 20).

[Meu06] T. Meunier, I. T. Vink, L. H. Willems van Beveren, F. H. L. Koppens, H. P. Tranitz, W. Wegscheider, L. P. Kouwenhoven, and L. M. K. Vandersypen: 'Nondestructive measurement of electron spins in a quantum dot', en, *Physical Review B* **74** (2006), DOI: 10.1103/PhysRevB.74.195303 (see p. 15).

[Mi18] X. Mi, M. Benito, S. Putz, D. M. Zajac, J. M. Taylor, Guido Burkard, and J. R. Petta: 'A coherent spin–photon interface in silicon', *Nature* **555** (2018), 599–603, DOI: 10.1038/nature25769 (see p. 2).

[Mil19] A. R. Mills, D. M. Zajac, M. J. Gullans, F. J. Schupp, T. M. Hazard, and J. R. Petta: 'Shuttling a single charge across a one-dimensional array of silicon quantum dots', en, *Nature Communications* **10** (2019), 1–6, DOI: 10.1038/s41467-019-08970-z (see p. 2).

[Mor18] Pierre-Andre Mortemousque, Emmanuel Chanrion, Baptiste Jadot, Hanno Flentje, Arne Ludwig, Andreas D. Wieck, Matias Urdampilleta, Christopher Bauerle, and Tristan Meunier: 'Coherent control of individual electron spins in a two dimensional array of quantum dots', *arXiv:1808.06180 [cond-mat]* (2018), arXiv: 1808.06180 (see p. 2).

[Nak99] Y. Nakamura, Yu. A. Pashkin, and J. S. Tsai: 'Coherent control of macroscopic quantum states in a single-Cooper-pair box', *Nature* **398** (1999), 786–788, DOI: 10.1038/19718 (see p. 2).

[Nak94] S. Nakata, M. Tomizawa, M. Yamamoto, K. Ikuta, and T. Mizutani: 'Electrical transport properties and confinement potential analysis of buried AlGaAs/GaAs quantum wires', *Journal of Applied Physics* **76** (1994), 2330–2335, DOI: 10.1063/1.357605 (see pp. 5, 6).

[Nix90] John A. Nixon and John H. Davies: 'Potential fluctuations in heterostructure devices', *Physical Review B* **41** (1990), 7929–7932, DOI: 10.1103/PhysRevB.41.7929 (see p. 83).

[Now07] K. C. Nowack, F. H. L. Koppens, Yu. V. Nazarov, and L. M. K. Vandersypen: 'Coherent Control of a Single Electron Spin with Electric Fields', en, *Science* **318** (2007), 1430–1433, DOI: 10.1126/science.1148092 (see pp. 11, 19, 26).

[Pag77] D. Paget, G. Lampel, B. Sapoval, and V. I. Safarov: 'Low field electron-nuclear spin coupling in gallium arsenide under optical pumping conditions', *Physical Review B* **15** (1977), 5780–5796, DOI: 10.1103/PhysRevB.15.5780 (see p. 21).

[Par02] J. Park, A. N. Pasupathy, J. I. Goldsmith, C. Chang, Y. Yaish, J. R. Petta, M. Rinkoski, J. P. Sethna, H. D. Abruña, P. L. McEuen, and D. C. Ralph: 'Coulomb blockade and the Kondo effect in single-atom transistors', *Nature* **417** (2002), 722–725, DOI: 10.1038/nature00791 (see pp. 5, 6).

[Par55] R. H. Parmenter: 'Symmetry Properties of the Energy Bands of the Zinc Blende Structure', *Phys. Rev.* **100** (1955), 573–579, DOI: 10.1103/PhysRev.100.573 (see p. 24).

[Pet05] J. R. Petta, A. C. Johnson, J. M. Taylor, E. A. Laird, A. Yacoby, M. D. Lukin, C. M. Marcus, M. P. Hanson, and A. C. Gossard: 'Coherent Manipulation of Coupled Electron Spins in Semiconductor Quantum Dots', en, *Science* **309** (2005), 2180–2184, DOI: 10.1126/science.1116955 (see pp. 2, 26).

[Pet04] J. R. Petta, A. C. Johnson, C. M. Marcus, M. P. Hanson, and A. C. Gossard: 'Manipulation of a Single Charge in a Double Quantum Dot', *Phys. Rev. Lett.* **93** (2004), 186802, DOI: 10.1103/PhysRevLett.93.186802 (see p. 59).

[Pla12] J. J. Pla, K. Y. Tan, J. P. Dehollain, W. H. Lim, J. J. L. Morton, D. N. Jamieson, A. S. Dzurak, and A. Morello: 'A single-atom electron spin qubit in silicon', *Nature* **489** (2012), 541–545, DOI: 10.1038/nature11449 (see p. 2).

[Pla13] J. J. Pla, K. Y. Tan, J. P. Dehollain, W. H. Lim, J. J. L. Morton, F. A. Zwanenburg, D. N. Jamieson, A. S. Dzurak, and A. Morello: 'High-fidelity readout and control of a nuclear spin qubit in silicon', *Nature* **496** (2013), 334–338, DOI: 10.1038/nature12011 (see p. 25).

[Pob07] F. Pobell: *Matter and methods at low temperatures*, vol. 2, Springer, 2007 (see p. 36).

[Pol09] Alberto Politi, Jonathan C. F. Matthews, and Jeremy L. O'Brien: 'Shor's Quantum Factoring Algorithm on a Photonic Chip', en, *Science* **325** (2009), 1221–1221, DOI: 10.1126/science.1173731 (see p. 2).

[Poo96] C. P. Poole: *Electron spin resonance: a comprehensive treatise on experimental techniques*, Courier Dover Publications, 1996 (see p. 25).

[Rai01] J. M. Raimond, M. Brune, and S. Haroche: 'Manipulating quantum entanglement with atoms and photons in a cavity', *Reviews of Modern Physics* **73** (2001), 565–582, DOI: 10.1103/RevModPhys.73.565 (see p. 2).

[Ras60] E. I. Rashba: 'Properties of semiconductors with an extremum loop. 1. Cyclotron and combinational resonance in a magnetic field perpendicular to the plane of the loop', *Soviet Physics-Solid State* **2** (1960), 1109–1122 (see p. 24).

[Ray85] Lord Rayleigh: 'On Waves Propagated along the Plane Surface of an Elastic Solid', *Proceedings of the London Mathematical Society* **s1-17** (1885), 4–11, DOI: 10.1112/plms/s1-17.1.4 (see p. 28).

[Rei07] D. J. Reilly, C. M. Marcus, M. P. Hanson, and A. C. Gossard: 'Fast single-charge sensing with a rf quantum point contact', en, *Applied Physics Letters* **91** (2007), 162101, DOI: 10.1063/1.2794995 (see pp. 10, 43).

[Rei08] D. J. Reilly, J. M. Taylor, J. R. Petta, C. M. Marcus, M. P. Hanson, and A. C. Gossard: 'Suppressing Spin Qubit Dephasing by Nuclear State Preparation', en, *Science* **321** (2008), 817–821, DOI: 10.1126/science.1159221 (see p. 22).

[Rug04] D. Rugar, R. Budakian, H. J. Mamin, and B. W. Chui: 'Single spin detection by magnetic resonance force microscopy', *Nature* **430** (2004), 329–332, DOI: 10.1038/nature02658 (see p. 61).

[Sac00] C. A. Sackett, D. Kielpinski, B. E. King, C. Langer, V. Meyer, C. J. Myatt, M. Rowe, Q. A. Turchette, W. M. Itano, D. J. Wineland, and C. Monroe: 'Experimental entanglement of four particles', en, *Nature* **404** (2000), 256–259, DOI: 10.1038/35005011 (see pp. 86, 90).

[San11] H. Sanada, T. Sogawa, H. Gotoh, K. Onomitsu, M. Kohda, J. Nitta, and P. V. Santos: 'Acoustically Induced Spin-Orbit Interactions Revealed by Two-Dimensional Imaging of Spin Transport in GaAs', en, *Physical Review Letters* **106** (2011), DOI: 10.1103/PhysRevLett.106.216602 (see pp. 25, 81, 86).

[San13] H. Sanada, Y. Kunihashi, H. Gotoh, K. Onomitsu, M. Kohda, J. Nitta, P. V. Santos, and T. Sogawa: 'Manipulation of mobile spin coherence using magnetic-field-free electron spin resonance', *Nature Physics* **9** (2013), 280–283, DOI: 10.1038/nphys2573 (see p. 25).

[Sca14] P. Scarlino, E. Kawakami, P. Stano, M. Shafiei, C. Reichl, W. Wegscheider, and L. M. K. Vandersypen: 'Spin-Relaxation Anisotropy in a GaAs Quantum Dot', en, *Physical Review Letters* **113** (2014), DOI: 10.1103/PhysRevLett.113.256802 (see p. 24).

[Sch04] R. Schleser, E. Ruh, T. Ihn, K. Ensslin, D. C. Driscoll, and A. C. Gossard: 'Time-resolved detection of individual electrons in a quantum dot', *Applied Physics Letters* **85** (2004), 2005–2007, DOI: 10.1063/1.1784875 (see p. 9).

[Shi96a] J. M. Shilton, V. I. Talyanskii, M. Pepper, D. A. Ritchie, J. E. F. Frost, C. J. B. Ford, C. G. Smith, and G. A. C. Jones: 'High-frequency single-electron transport in a quasi-one-dimensional GaAs channel induced by surface acoustic waves', *Journal of Physics: Condensed Matter* **8** (1996), L531, DOI: 10.1088/0953-8984/8/38/001 (see p. 30).

[Shi96b] J. M. Shilton, D. R. Mace, V. I. Talyanskii, Y. Galperin, C. B. Simmons, M. Pepper, and D. A. Ritchie: 'On the acoustoelectric current in a one-dimensional channel', *Journal of Physics: Condensed Matter* **8** (1996), L337, DOI: 10.1088/0953-8984/8/24/001 (see p. 30).

[Sho94] P. W. Shor: 'Algorithms for Quantum Computation: Discrete Logarithms and Factoring', *Proceedings of the 35th Annual Symposium on Foundations of Computer Science*, 1994, 124–134, DOI: 10.1109/SFCS.1994.365700 (see p. 1).

[Shu12] M. D. Shulman, O. E. Dial, S. P. Harvey, H. Bluhm, V. Umansky, and A. Yacoby: 'Demonstration of Entanglement of Electrostatically Coupled Singlet-Triplet Qubits', en, *Science* **336** (2012), 202–205, DOI: 10.1126/science.1217692 (see p. 86).

[Spr02] D. Sprinzak, Y. Ji, M. Heiblum, D. Mahalu, and H. Shtrikman: 'Charge Distribution in a Kondo-Correlated Quantum Dot', *Phys. Rev. Lett.* **88** (2002), 176805, DOI: 10.1103/PhysRevLett.88.176805 (see p. 9).

[Ste96] A. M. Steane: 'Error Correcting Codes in Quantum Theory', *Phys. Rev. Lett.* **77** (1996), 793–797, DOI: 10.1103/PhysRevLett.77.793 (see p. 2).

[Sto05] James A. H. Stotz, Rudolf Hey, Paulo V. Santos, and Klaus H. Ploog: 'Coherent spin transport through dynamic quantum dots', *Nature Materials* **4** (2005), 585 (see p. 2).

[Tak19] Shintaro Takada et al.: 'Sound-driven single-electron transfer in a circuit of coupled quantum rails', en, *Nature Communications* **10** (2019), arXiv: 1903.00684, 4557, DOI: 10.1038/s41467-019-12514-w (see p. 74).

[Tak16] Kenta Takeda, Jun Kamioka, Tomohiro Otsuka, Jun Yoneda, Takashi Nakajima, Matthieu R. Delbecq, Shinichi Amaha, Giles Allison, Tetsuo Kodera, Shunri Oda, and Seigo Tarucha: 'A fault-tolerant addressable spin qubit in a natural silicon quantum dot', en, *Science Advances* **2** (2016), e1600694, DOI: 10.1126/sciadv.1600694 (see p. 26).

[Tay07] J. M. Taylor, J. R. Petta, A. C. Johnson, A. Yacoby, C. M. Marcus, and M. D. Lukin: 'Relaxation, dephasing, and quantum control of electron spins in double quantum dots', *Phys. Rev. B* **76** (2007), 035315, DOI: 10.1103/PhysRevB.76.035315 (see pp. 21, 22).

[Tha12] Romain Thalineau, Sylvain Hermelin, Andreas D. Wieck, Christopher Bäuerle, Laurent Saminadayar, and Tristan Meunier: 'A few-electron quadruple quantum dot in a closed loop', en, *Applied Physics Letters* **101** (2012), 103102, DOI: 10.1063/1.4749811 (see p. 2).

[Tri12] L. Trifunovic, O. Dial, M. Trif, J. R. Wootton, R. Abebe, A. Yacoby, and D. Loss: 'Long-Distance Spin-Spin Coupling via Floating Gates', *Phys. Rev. X* **2** (2012), 011006, DOI: 10.1103/PhysRevX.2.011006 (see p. 2).

[Tyr12] A. M. Tyryshkin, S. Tojo, J. J. L. Morton, H. Riemann, N. V. Abrosimov, P. Becker, H.-J. Pohl, T. Schenkel, L. W. Thewalt, K. M. Itoh, and S. A. Lyon: 'Electron spin coherence exceeding seconds in high-purity silicon', *Nature Materials* **11** (2012), 143–147, DOI: 10.1038/nmat3182 (see p. 2).

[Uma09] V. Umansky, M. Heiblum, Y. Levinson, J. Smet, J. Nübler, and M. Dolev: 'MBE growth of ultra-low disorder 2DEG with mobility exceeding 35\times10 ^{6}}$ cm ^{2}}$/V s', *Journal of Crystal Growth* **311** (2009), 1658–1661, DOI: 10.1016/j.jcrysgro.2008.09.151 (see p. 6).

[Urd19] Matias Urdampilleta et al.: 'Gate-based high fidelity spin readout in a CMOS device', *Nature Nanotechnology* (2019), DOI: 10.1038/s41565-019-0443-9 (see pp. 18, 94).

[Van17] L. M. K. Vandersypen, H. Bluhm, J. S. Clarke, A. S. Dzurak, R. Ishihara, A. Morello, D. J. Reilly, L. R. Schreiber, and M. Veldhorst: 'Interfacing spin qubits in quantum dots and donors—hot, dense, and coherent', en, *npj Quantum Information* **3** (2017), DOI: 10.1038/s41534-017-0038-y (see p. 2).

[Van01] Lieven M. K. Vandersypen, Matthias Steffen, Gregory Breyta, Costantino S. Yannoni, Mark H. Sherwood, and Isaac L. Chuang: 'Experimental realization of Shor's quantum factoring algorithm using nuclear magnetic resonance', en, *Nature* **414** (2001), 883–887, DOI: 10.1038/414883a (see p. 2).

[Vel14] M. Veldhorst, J. C. C. Hwang, C. H. Yang, A. W. Leenstra, B. de Ronde, J. P. Dehollain, J. T. Muhonen, F. E. Hudson, K. M. Itoh, A. Morello, and A. S. Dzurak: 'An addressable quantum dot qubit with fault-tolerant control-fidelity', *Nature Nanotechnology* (2014), DOI: 10.1038/nnano.2014.216 (see p. 2).

[Wee88] B. J. van Wees, H. van Houten, C. W. J. Beenakker, J. G. Williamson, L. P. Kouwenhoven, D. van der Marel, and C. T. Foxon: 'Quantized conductance of point contacts in a two-dimensional electron gas', *Phys. Rev. Lett.* **60** (1988), 848–850, DOI: 10.1103/PhysRevLett.60.848 (see p. 9).

[Wei57] G. Weinreich and H. G. White: 'Observation of the Acoustoelectric Effect', *Phys. Rev.* **106** (1957), 1104–1106, DOI: 10.1103/PhysRev.106.1104 (see p. 28).

[Wei77] Claude Weisbuch and Claudine Hermann: 'Optical detection of conduction-electron spin resonance in GaAs, $\mathrmGa_1\ensuremath-x\mathrmIn_-x\mathrmAs$, and $\mathrmGa_1\ensuremath-x\mathrmAl_x\mathrmAs$', *Phys. Rev. B* **15** (1977), 816–822, DOI: 10.1103/PhysRevB.15.816 (see p. 11).

[Yan13] C. H. Yang, A. Rossi, R. Ruskov, N. S. Lai, F. A. Mohiyaddin, S. Lee, C. Tahan, G. Klimeck, A. Morello, and A. S. Dzurak: 'Spin-valley lifetimes in a silicon quantum dot with tunable valley splitting', *Nature Communications* **4** (2013), DOI: 10.1038/ncomms3069 (see p. 59).

[Yon18] Jun Yoneda, Kenta Takeda, Tomohiro Otsuka, Takashi Nakajima, Matthieu R. Delbecq, Giles Allison, Takumu Honda, Tetsuo Kodera, Shunri Oda, Yusuke Hoshi, Noritaka Usami, Kohei M. Itoh, and Seigo Tarucha: 'A quantum-dot spin qubit with coherence limited by charge noise and fidelity higher than 99.9%', en, *Nature Nanotechnology* **13** (2018), 102–106, DOI: 10.1038/s41565-017-0014-x (see pp. 2, 26).

[Zaj16] D. M. Zajac, T. M. Hazard, X. Mi, E. Nielsen, and J. R. Petta: 'Scalable Gate Architecture for a One-Dimensional Array of Semiconductor Spin Qubits', en, *Physical Review Applied* **6** (2016), DOI: 10.1103/PhysRevApplied.6.054013 (see p. 2).

[Zen32] C. Zener: 'Non-Adiabatic Crossing of Energy Levels', *Proc. R. Soc. Lond. A* **137** (1932), 696–702, DOI: 10.1098/rspa.1932.0165 (see p. 69).

[Zim03] N. M. Zimmerman and M. W. Keller: 'Electrical metrology with single electrons', *Measurement Science and Technology* **14** (2003), 1237, DOI: 10.1088/0957-0233/14/8/307 (see p. 30).

List of Figures

APPENDIX A

Spin evolution during the transport

A.1 Single-spin rotation

We consider an arbitrary single-spin rotation whose Hamiltonian is:

$$\mathrm{H} = \frac{\hbar\omega_x}{2}\sigma_x + \frac{\hbar\omega_y}{2}\sigma_y + \frac{\hbar\omega_z}{2}\sigma_z \tag{A.1}$$

Applying this Hamiltonian for a duration τ is equivalent to the unitary transformation:

$$\begin{aligned} \mathrm{U} &= \exp\left(-\frac{i\mathrm{H}\tau}{\hbar}\right) \\ &= \cos\left(\frac{\omega_{\mathrm{tot}}\tau}{2}\right)\mathrm{I}_2 - i\left[\frac{\omega_x}{\omega_{\mathrm{tot}}}\sigma_x + \frac{\omega_y}{\omega_{\mathrm{tot}}}\sigma_y + \frac{\omega_z}{\omega_{\mathrm{tot}}}\sigma_z\right]\sin\left(\frac{\omega_{\mathrm{tot}}\tau}{2}\right) \\ &\text{with } \omega_{\mathrm{tot}} = \sqrt{\omega_x^2 + \omega_y^2 + \omega_z^2} \end{aligned} \tag{A.2}$$

which is a rotation by an angle $\theta = \omega_{\mathrm{tot}}\tau$ around the axis $\vec{u} = \frac{1}{\omega_{\mathrm{tot}}}(\omega_x, \omega_y, \omega_z)$.

For the particular case $\vec{u} = \frac{1}{\sqrt{2}}(1,0,1)$ and $\theta = \pi$, we obtain an Hadamard gate:

$$\begin{aligned} \mathrm{U_{Hd}} &= \frac{-i}{\sqrt{2}}(\sigma_x + \sigma_z) \\ &= \frac{-i}{\sqrt{2}}\begin{pmatrix} 1 & 1 \\ 1 & -1 \end{pmatrix} \end{aligned} \tag{A.3}$$

In the most general case, we note this single-spin rotation in a abbreviated form to

simplify the derivation:

$$\begin{aligned} \mathrm{U} &= \begin{pmatrix} A & -iB \\ -i\bar{B} & \bar{A} \end{pmatrix} \\ \text{with } A &= \cos\left(\frac{\omega_{\mathrm{tot}}\tau}{2}\right) - i\frac{\omega_z}{\omega_{\mathrm{tot}}}\sin\left(\frac{\omega_{\mathrm{tot}}\tau}{2}\right) \\ \text{and } B &= \left(\frac{\omega_x}{\omega_{\mathrm{tot}}} - i\frac{\omega_y}{\omega_{\mathrm{tot}}}\right)\sin\left(\frac{\omega_{\mathrm{tot}}\tau}{2}\right) \end{aligned} \tag{A.4}$$

In addition, we mention that because U is unitary, $|A|^2 + |B|^2 = 1$.

A.2 Two-spin operation

We now consider that this single-spin rotation is applied sequentially on each spin of a two-qubit system with a given delay. During this delay, each spin precesses around a z external magnetic field, accumulating a phase ϕ. For the first (resp. second) spin this phase is therefore accumulated after (resp. before) the single-spin rotation previously described. The two-qubit transformation is thus:

$$\begin{aligned} \mathrm{U}_{\mathrm{tot}} &= \mathrm{Z}_\phi \times \mathrm{U} \otimes \mathrm{U} \times \mathrm{Z}_\phi \\ &= \begin{pmatrix} e^{-i\frac{\phi}{2}} & 0 \\ 0 & e^{+i\frac{\phi}{2}} \end{pmatrix} \begin{pmatrix} A & -iB \\ -i\bar{B} & \bar{A} \end{pmatrix} \otimes \begin{pmatrix} A & -iB \\ -i\bar{B} & \bar{A} \end{pmatrix} \begin{pmatrix} e^{-i\frac{\phi}{2}} & 0 \\ 0 & e^{+i\frac{\phi}{2}} \end{pmatrix} \\ &= \begin{pmatrix} Ae^{-i\frac{\phi}{2}} & -iBe^{-i\frac{\phi}{2}} \\ -i\bar{B}e^{+i\frac{\phi}{2}} & \bar{A}e^{+i\frac{\phi}{2}} \end{pmatrix} \otimes \begin{pmatrix} Ae^{-i\frac{\phi}{2}} & -iBe^{+i\frac{\phi}{2}} \\ -i\bar{B}e^{-i\frac{\phi}{2}} & \bar{A}e^{+i\frac{\phi}{2}} \end{pmatrix} \end{aligned} \tag{A.5}$$

If we initially prepare the two spins in a singlet state $|S\rangle = \frac{1}{\sqrt{2}}(|\uparrow\downarrow\rangle - |\downarrow\uparrow\rangle)$, the probability to measure a singlet spin state after this transformation is:

$$\begin{aligned} P_S &= |\langle S|\,\mathrm{U}_{\mathrm{tot}}\,|S\rangle|^2 \\ &= \left|\frac{1}{2}\langle\downarrow\uparrow|\,\mathrm{U}_{\mathrm{tot}}\,|\downarrow\uparrow\rangle + \frac{1}{2}\langle\uparrow\downarrow|\,\mathrm{U}_{\mathrm{tot}}\,|\uparrow\downarrow\rangle - \frac{1}{2}\langle\downarrow\uparrow|\,\mathrm{U}_{\mathrm{tot}}\,|\uparrow\downarrow\rangle - \frac{1}{2}\langle\uparrow\downarrow|\,\mathrm{U}_{\mathrm{tot}}\,|\downarrow\uparrow\rangle\right|^2 \\ &= \left||A|^2 + \frac{e^{+i\phi} + e^{-i\phi}}{2}|B|^2\right|^2 \\ &= \left||A|^2 + |B|^2\cos(\phi)\right|^2 \end{aligned} \tag{A.6}$$

The singlet spin state probability therefore oscillates with the accumulated phase ϕ during the delay between the two single-spin operations. This probability has always a maximum of 1 for $\phi = 0\ [2\pi]$, when constructive interferences bring the two-qubit system back to a singlet state no matter what the unitary transformation U is.

However the oscillation contrast, given by $2|B|^2$, depends on the axis and angle of the

single spin rotation. It is equal to 1 for the condition:

$$\begin{aligned} |B|^2 &= \frac{\omega_x^2 + \omega_y^2}{\omega_{\mathrm{tot}}^2} \sin^2\left(\frac{\omega_{\mathrm{tot}}\tau}{2}\right) = \frac{1}{2} \\ \Leftrightarrow \sin^2\left(\frac{\omega_{\mathrm{tot}}\tau}{2}\right) &= \frac{1}{2}\left(1 + \frac{\omega_z^2}{\omega_x^2 + \omega_y^2}\right) \end{aligned} \tag{A.7}$$

A.3 Example for spin-orbit coupling

An electron propagating with a constant momentum $\vec{p}$ endures a single-spin rotation such as the one described above. If the propagation is in the (x,y) plane, the electron spin experiments an apparent magnetic field B_{SO} in the (x,y) plane as well. Because this magnetic field is proportional to the electron speed v, it is often convenient to define the spin-orbit length as the distance needed to achieve a π pulse in the absence of any other external magnetic field:

$$l_{\mathrm{SO}} = \frac{\pi v}{\omega_{\mathrm{SO}}} = \frac{\pi \hbar v}{|g|\mu_{\mathrm{B}} B_{\mathrm{SO}}} \tag{A.8}$$

In the presence of an additional orthogonal magnetic field B_z, the rotation axis is shifted towards $\vec{z}$ and the precession becomes faster, as illustrated figure A.1. The condition for maximum contrast obtained in eq. A.7 is equivalent to:

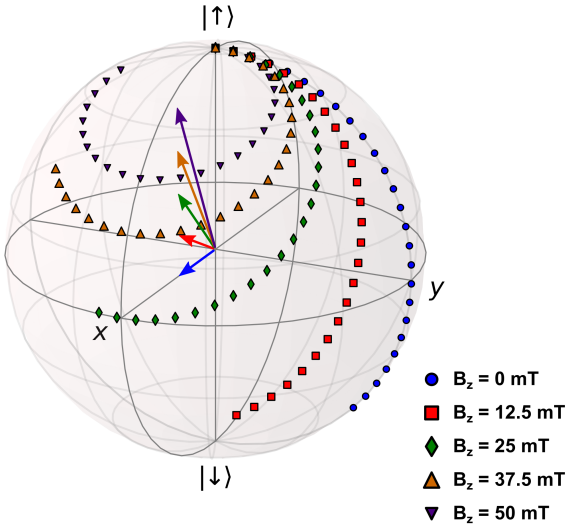

Figure A.1: Spin trajectories. Evolution of a single spin initially in a $|\uparrow\rangle$ state for different values of external magnetic field B_z. Here $B_{\mathrm{SO}} = 25\,\mathrm{mT}$, $v = 2.79\,\mu\mathrm{m/ns}$ and $l = 6\,\mu\mathrm{m}$. For $B_z = B_{\mathrm{SO}}$, the rotation maps the two poles $|\uparrow\rangle$ and $|\downarrow\rangle$ to opposite points in the equatorial plane.

$$\begin{aligned} \sin^2\left(\frac{\sqrt{\omega_{\mathrm{SO}}^2+\omega_z^2}}{2}\frac{l}{v}\right) &= \frac{1}{2}\left(1+\frac{\omega_z^2}{\omega_{\mathrm{SO}}^2}\right) \\ \Leftrightarrow \sin^2\left(\frac{\pi l}{2l_{\mathrm{SO}}}\sqrt{1+\frac{\omega_z^2}{\omega_{\mathrm{SO}}^2}}\right) &= \frac{1}{2}\left(1+\frac{\omega_z^2}{\omega_{\mathrm{SO}}^2}\right) \end{aligned} \tag{A.9}$$

For a propagation length $l \in \left[\frac{l_{\mathrm{SO}}}{2}\,;\frac{3l_{\mathrm{SO}}}{2}\right]$, this equation always has one solution $\omega_{z,0} \in [0\,;\omega_{\mathrm{SO}}]$, shown in Fig. A.2.

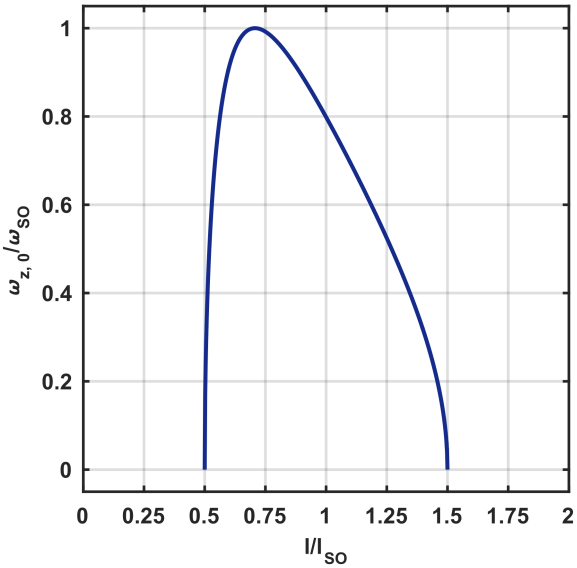

Figure A.2: Condition for maximum contrast oscillations. Necessary external magnetic field (in units of the spin-orbit equivalent magnetic field) to fulfill Eq. A.9, for different propagation length. For $l < \frac{l_{\mathrm{SO}}}{2}$ or $l \in \left]\frac{3l_{\mathrm{SO}}}{2}\,;2l_{\mathrm{SO}}\right[$, there is no solution. For $l > 2l_{\mathrm{SO}}$, there can be more than one solution.

At this particular external magnetic field $B_{z,0}$, the operation felt by each electron is analogous to an Hadamard gate, transforming the two basis state $|\downarrow\rangle$ and $|\uparrow\rangle$ into two state located opposite to each other on the Bloch sphere equator:

$$\mathrm{U}_0 = \frac{1}{\sqrt{2}}\begin{pmatrix} 1 & e^{i\phi_0} \\ 1 & -e^{i\phi_0} \end{pmatrix} \tag{A.10}$$

APPENDIX B

Tunnel-selective readout contrast

In this thesis, the spin readout relies on a first conversion towards a charge configuration, which is then read-out by the electrometer. We exploit the greater coupling towards the reservoir of the triplet spin states to discriminate them by their faster tunnel-out rate compared to a singlet spin state. Thus, we open the coupling towards the reservoir by a voltage pulse applied on RH2, raising the dot chemical potential and kicking electrons towards the reservoir. The system is then brought back to the isolated regime, allowing for a 200 µs charge readout. This use of the isolated regime allows us to decouple the spin-selective process duration and the electrometer bandwidth, as there is no more need to observe electron jumps towards the reservoir in real time. In Chap. 4, the voltage pulse used to perform spin-to charge conversion has a duration of 16 µs, the minimum duration allowed by the DAC. However, it is interesting to check whether a physical limitation prevents the realization of a tunnel-selective spin conversion on faster timescales.

Using an AWG connected to the fast RP1 gate, we can probe the spin-selectivity for shorter pulses, down to a few nanoseconds. As presented in Fig. B.1, a shorter pulse duration required a higher amplitude to observe the first electron tunnel-out, but the contrast between a mostly singlet and mixed ($50\,\%\ S - 50\,\%\ T_0$) spin state remains constant and close to $23 \pm 1\,\%$ for the right side of the structure. This indicates that the spin-to-charge conversion can be reduced to a few nanoseconds without affecting its fidelity. In terms of timing, this sets the charge readout as the main bottleneck, with the best electrometer bandwidths around a few MHz. This analysis completes the development of sub-µs spin manipulation, together with the fast adiabatic singlet initialization presented in Chap. 4.

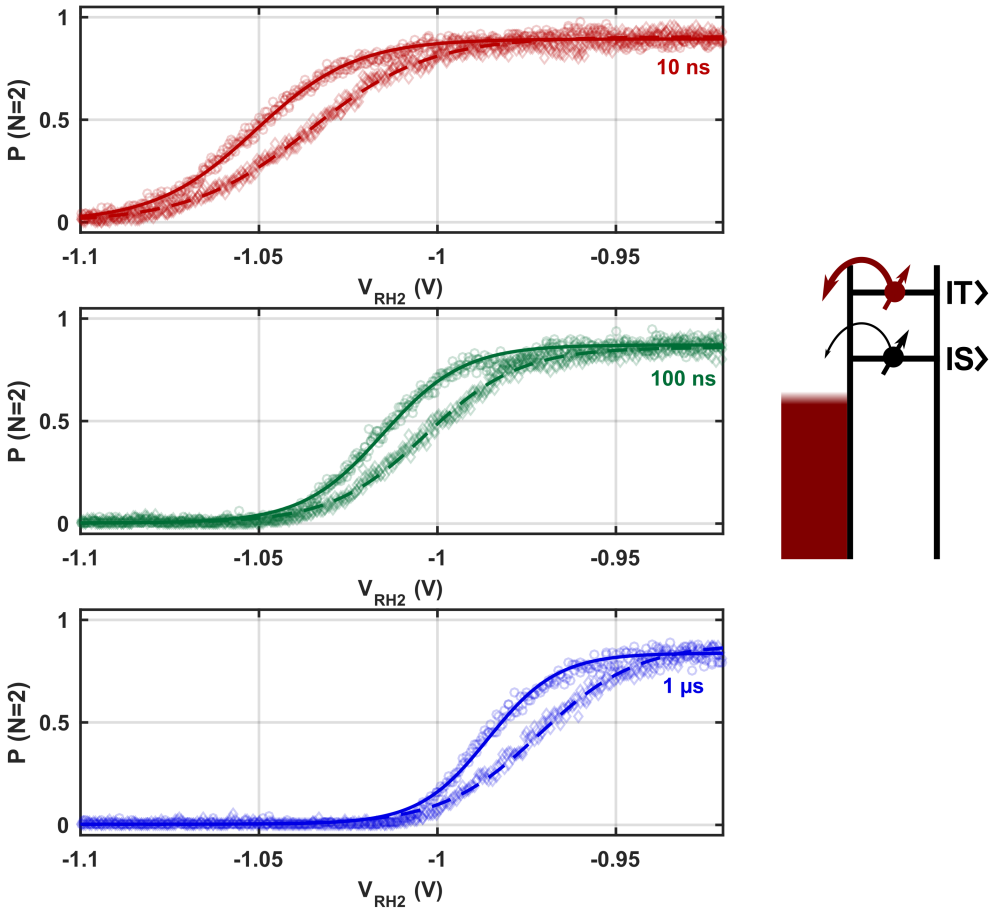

Figure B.1: Tunnel-selective readout contrast. Two electrons are prepared in a singlet (solid) or mixed (dashed) spin state. A voltage pulse of duration 10 ns, 100 ns or 1 µs is applied, temporarily bringing the quantum dot chemical potential closer to the Fermi reservoir. As this pulse becomes shorter, its amplitude needs to increase to allow the tunnel-out process. We observe a similar contrast between the two spin preparations for the different pulse duration, indicating a constant tunnel-out ratio Γ_T/Γ_S between triplet and singlet spin states.

APPENDIX C

Excited orbital states

In the *spin map* presented in Chap. 4, we identified a weak interdot coupling regime where a singlet spin state is preserved even at zero detuning, because the (1,1) charge configuration is unaccessible within the 500 ns duration of the detuning pulse. Figure C.1. presents a similar spin map, where the singlet spin probability is recorded after a 500 ns AWG pulse on gates RP1 and RP2. At the bottom-right corner, we can identify the (2,0) charge state where a singlet remains the ground spin state of the system. The detuning axis $\varepsilon = \delta V_{\mathrm{RP1}} - \delta V_{\mathrm{RP2}}$, is indicated by the black arrow. We observe parallel mixing lines, attributed to excited $|S_{(1,1)}\rangle$ states.

Since our quantum dots are weakly coupled, the detuning pulse is extremely non-adiabatic with respect to the avoided crossings, and the relaxation mechanisms from (2,0) to (1,1) occur on much longer timescales. Thus, our spin states can remain the $|S_{(2,0)}\rangle$ state, even when $|S_{(1,1)}\rangle$ are lower in energy. Mixing only occurs when the detuning pulse brings the system exactly at one avoided crossing, allowing hyperfine coupling to transform the spin state into an excited $|T_{0\ (1,1)}\rangle$ state.

To probe the dynamics of these higher orbitals and their coupling to the ground $|S_{(2,0)}\rangle$ state, we perform a Landau-Zener experiment where the detuning is ramped across the avoided crossing, and the probability to end up in the excited state is recorded. For this, we apply a 50 mV ramp on RP1 and RP2 of variable duration, followed by a non-adiabatic return towards higher detuning. In order to only probe the Nth avoided crossing, the ramp is started only after rapidly crossing N-1 mixing lines.

We observe a decay of the final singlet probability as the ramp duration increases, and extract the amplitudes of the avoided crossings from the characteristic timescales of these decays (Fig. C.1.bc.). We obtain a quadratic increase of the interdot coupling as higher orbitals are involved, from 280 ± 25 MHz to 870 ± 25 MHz. This increase is expected from the greater spatial extension of the higher (1,1) orbital states, increasing their overlap with the ground (2,0) orbital.

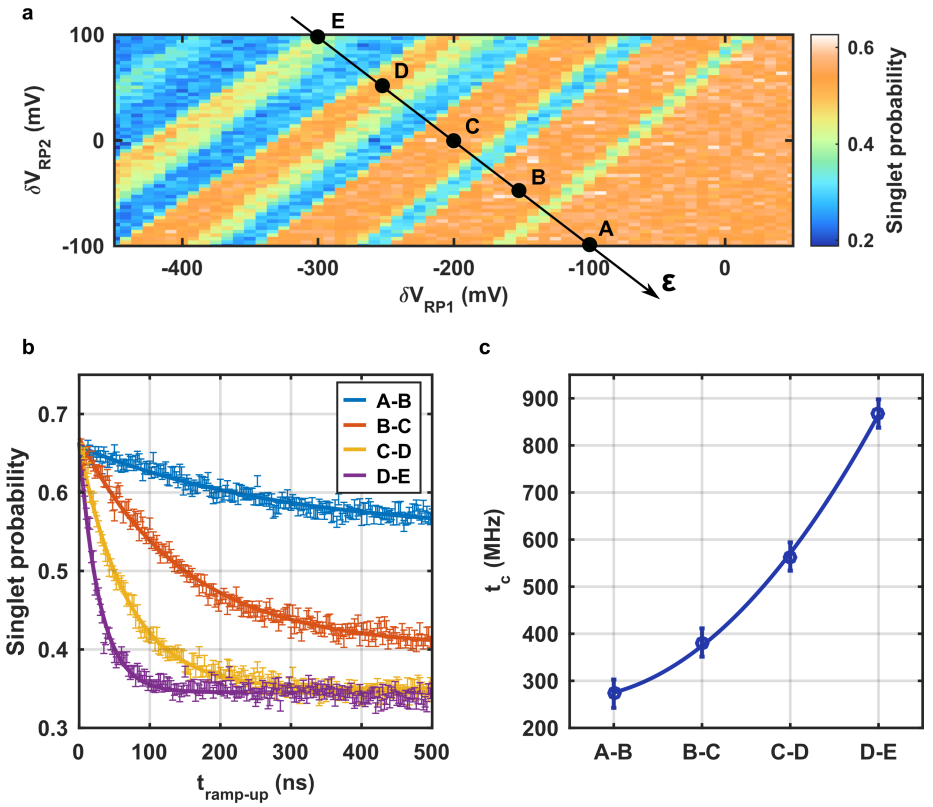

Figure C.1: Excited orbital states. a. Spin-map of the right double quantum dot in the weak interdot coupling regime. We can see parallel mixing lines, attributed to avoided crossings between $|S_{(2,0)}\rangle$ and excited $|S_{(1,1)}\rangle$ states. To probe the Nth avoided crossing, we jump over the N-1 mixing lines and perform a Landau-Zener adiabatic ramp, immediately followed by a fast return to the (2,0) configuration (A). **b.** Singlet probability as a function of the ramp-up duration, for each four avoided-crossings. **c.** Amplitudes of each avoided crossing t_c, extracted from the decays obtained in **b**. We observe a quadratic increase of the coupling as higher (1,1) orbitals are involved, in agreement with their greater spatial extension.

APPENDIX D

Decoherence source at high magnetic field

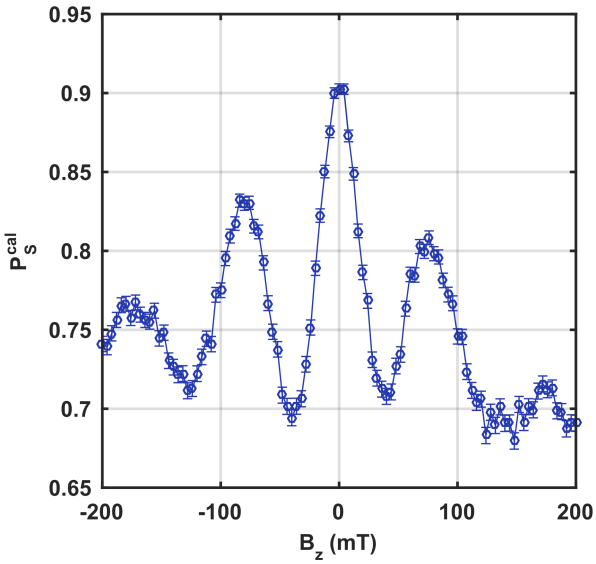

Figure D.1: Decoherence at $\Delta t = 0$. Singlet probability after recombination for $\Delta t_{\text{sending}} = 0\,\text{ns}$ as a function of the external magnetic field. The oscillations are explained by the magnitude of the single-spin rotations (see Chap. 5), and characteristic of the channel length, SAW velocity and spin-orbit length. In particular, around $|Bz| \approx 75\,\text{mT}$ the electrons endure a 2π rotation and the expected singlet probability after transfer is expected to be identical to the $B_z = 0\,\text{mT}$ case. This experimental data thus points at a decoherence mechanism proportional to B_z, affecting the electron spins during their motion.

As discussed in the main text, the contrast of the coherent oscillations obtained in the two-electron transfer experiment depends on the ratio of external magnetic field B_z to the spin-orbit equivalent magnetic field B_{SO}. Figure D.1 presents a larger cut for a minimum electron separation $\Delta t_{\text{sending}} = 0\,\text{ns}$, and allows us to probe this dependance. We observe damped oscillations in the singlet probability after recombination, the position of the local maxima being in good agreement with the expected parameters $v_{\text{SAW}} = 2700\,\text{m/s}$,

$l_{\mathrm{SO}} = 8.5\,\mu\mathrm{m}$ and $l = 6\,\mu\mathrm{m}$. However, the observed decoherence towards higher magnetic field is not expected for a simple hyperfine coupling, as the electrons are never separated more than a few nanoseconds. Instead, a mechanism involving potential inhomogeneities, leading to a decoherence proportional to B_z, needs to be considered.[Hua13] In the main text, we develop a numerical simulation to account for this phenomenon, which is in good qualitative agreement with this experimental result.

Acknowledgments

À la fin de ce projet de thèse vient le temps de remercier ceux qui m'ont aidé à le mener à bout, et qui m'ont permis de grandir scientifiquement, professionnellement et humainement. Évidemment en tout premier lieu à Tristan, qui a toujours été présent à mes côtés dans toutes les étapes. Que ce soit lors des soirées passées devant les écrans, le suivi par SMS les week-ends, ou encore tes irruptions fréquentes (et remarquées) dans le bureau du bâtiment V, tu m'as impressionné par la passion que tu voues à ton métier et ta faculté à mener un millier de projets simultanément de front. Nos débats animés sur l'interprétation des résultats expérimentaux ont, pour paraphraser un grand philosophe passé par le bâtiment M, façonné le physicien que je suis aujourd'hui. Merci à Chris pour m'avoir enseigné le goût des choses faites soigneusement et avec le bon outil, et pour m'avoir laissé utiliser ton frigo aussi longtemps. Évidemment, un grand merci aux deux meilleurs post-docs du bâtiment M : Pierre-André qui m'a tout appris depuis mes premiers pas et Matias qui m'a accompagné dans les débuts nébuleux du projet silicium. Vous avez tous les deux été à la fois d'excellents mentors et la source de nombreuses idées exploitées dans cette thèse, mais aussi un important contre-pouvoir arbitrant les débats.

Un merci tout particulier à l'équipe régionale de baby-foot et membres de groupes WhatsApp prud'homaux, qui m'a permis de relâcher la pression : Gérard, Klaus, Tipiak, Naruto, Bambi et Tourtemisque. Merci pour les restaus d'après-manif, les soirées mojitos, et les memes douteux. Plus généralement, merci aux autres thésards et post-docs du Bat M, passés ou présents : Giorgos, Hermann, Jun-Liang, Takada-sensei pour avoir partagé le fardeau du Labview, Cameron, Bernhard, David, Ben pour avoir mis la barre aussi haute, Hanno, Greg, Vivien pour m'avoir aidé à monter la manip, Candice pour tes précieux conseils en phase de rédaction, Mathias pour les pauses café et autres interludes musicaux. Discuter avec vous, autant de physique que de politique, a contribué à rendre cette thèse plus formatrice et intéressante encore.

Je tiens également à remercier les pôles de l'Institut Néel qui m'ont aidé à mener ce projet à bien avec bienveillance et compétence. Merci à l'équipe Nanofab : Thierry, Seb, Bruno, Jeff, Latifa et Gwen pour les heures passées en salle blanche à mes côtés. Merci au pôle électronique : Christophe Guttin, Daniel et en particulier à Christophe Hoarau pour m'avoir aidé à mesurer des centaines d'IDTs. Merci au pôles ingénierie expérimentale et cryogénie, en particulier Pierre Perrier, Éric, Gilles et Henri qui m'ont assisté dans mes problèmes cryogéniques. Merci également à l'équipe du liquéfacteur qui m'a permis d'avoir les milliers de litres d'hélium nécessaires à cette thèse. Enfin, merci aux équipes

administratives, Angélique, Otmane, Florence et Sabine, qui m'ont aidé pour les missions, contrats et autres commandes.

Merci à Thomas Ihn et Patrice Bertet d'avoir accepté d'être rapporteurs de ce manuscrit, et également à Alexia Auffèves et Jean-Michel Raimond de me faire l'honneur d'être membres de mon jury. Merci à vous quatre pour avoir été aussi flexibles et réactifs sur la fin de la rédaction de thèse.

Merci à mes amis, famille et belle-famille, qui m'ont permis de penser momentanément à autre chose et m'ont fait travailler mes qualités de vulgarisation scientifique. En particulier, un grand merci à mes frères et mes parents que je n'ai pas beaucoup vu ces derniers mois. Enfin, et plus que tout, merci à Anthéa pour tout ce que tu m'apportes au quotidien. Depuis tes qualités d'écoute et de conseil jusqu'à ta patience lors des urgences cryo en pleine nuit, je n'aurais jamais pu arriver au bout de ce projet sans toi.